UNIVERSITÀ DEGLI STUDI DI BARI ALDO MORO

DIPARTIMENTO INTERATENEO DI FISICA "M. MERLIN"

LAUREA MAGISTRALE IN PHYSICS

Master Thesis

Performance in a high-rate environment of triple-GEM detectors for the Phase-2 upgrade of the CMS detector

CERN-THESIS-2024-114
//2024

Relatori:
Dott. Piet Omer J. Verwilligen
Dott. Antonello Pellecchia
Controrelatrice:
Dott.ssa Alessandra Pastore

Laureando:
Felice Nenna

---

a.a. 2023/2024

Contents

Introduction 1

1 Gas Electron Multipliers 3
1.1 Interaction of particles with matter . . . 3
1.1.1 Energy loss of charged particles by ionization . . . 3
1.1.2 Interaction of photons with matter . . . 5
1.2 Working principle of gaseous detectors . . . 7
1.2.1 Primary ionization . . . 8
1.2.2 Drift and diffusion . . . 9
1.2.3 Charge multiplication . . . 11
1.2.4 Signal formation . . . 12
1.3 Examples of gaseous detectors . . . 13
1.3.1 Single-Wire Proportional Chamber . . . 13
1.3.2 Multiwire Proportional Chambers . . . 14
1.3.3 Cathode Strip Chambers . . . 14
1.3.4 Drift Chambers . . . 15
1.3.5 Resistive Plate Chambers . . . 15
1.4 MPGD . . . 16
1.4.1 Historical development and evolution . . . 16
1.5 GEM detectors . . . 18
1.5.1 GEM detectors design . . . 18
1.5.2 Basic GEM operation . . . 19
1.5.3 Multi-GEM Assemblies . . . 20
1.5.4 Rate Capability and Radiation Resistance . . . 21
1.5.5 Discharges and Breakdown . . . 22
1.5.6 Ageing . . . 22
1.6 Performance of Gaseous Detectors . . . 22
1.6.1 Impact of the gas choice . . . 22
1.6.2 Spatial resolution . . . 23
1.6.3 Time resolution . . . 24

2 The CMS experiment 27
2.1 General design and characteristics . . . 27
2.1.1 The Silicon Tracker . . . 27
2.1.2 Electromagnetic Calorimeter . . . 28
2.1.3 Hadronic Calorimeter . . . 28
2.1.4 The solenoid magnet . . . 28
2.1.5 The Muon System . . . 29
2.1.6 Trigger and DAQ . . . 30
2.2 CMS Phase-2 upgrade . . . 30
2.3 CMS Phase-2 upgrade of the Muon System . . . 31
2.3.1 Upgrade of the electronics of existing muon detectors . . . 32
Drift Tube chambers . . . 33

Cathode Strip Chambers . . . 33
Resistive Plate Chambers . . . 33
2.3.2 New detectors for the Phase 2 upgrade of the muon system . . . 34
*i*RPC detectors: RE3/1 and RE4/1 . . . 34
GEM detectors . . . 34
2.3.3 Maintaining existing trigger capabilities . . . 35
2.3.4 The ME0 station: muon identification and triggering in the very forward region . . . 37

3 The CMS GEM ME0 43
3.1 CMS triple-GEM detectors for ME0 station . . . 43
3.1.1 GEM module design . . . 43
3.1.2 Performance requirements . . . 45
3.2 Design of the ME0 readout chain . . . 46
3.3 The front-end electronics . . . 47
3.3.1 The readout chip: VFAT3 . . . 47
3.3.2 The optohybrid . . . 50
3.3.3 The GEM electronic board . . . 51
3.4 Back-end electronics . . . 51
3.5 Data Acquisition Software (DAQ) . . . 52
3.6 Power system design . . . 52
3.6.1 High Voltage system . . . 52
3.6.2 Low Voltage system . . . 54
3.7 Electronics calibration and configuration . . . 55
3.7.1 GBT phase scan . . . 55
3.7.2 DAC scan . . . 56
3.7.3 S-bit rate scan . . . 56
3.7.4 S-curve . . . 57
3.7.5 Latency scan . . . 59

4 CMS ME0 performance in high background rate environment 61
4.1 GIF++ at CERN . . . 61
4.1.1 General features . . . 61
4.1.2 Characteristics of the photon flux . . . 62
4.1.3 Dose rate at GIF++ vs ME0 . . . 63
4.2 Test beam setup . . . 64
4.3 Test Beam operations . . . 66
4.4 Reconstruction . . . 67
4.5 Analysis workflow . . . 67
4.5.1 Beam profile . . . 67
4.5.2 Background rate measurement at the GIF++ . . . 68
4.5.3 Efficiency computation . . . 71
4.6 Results and discussion . . . 74
4.6.1 HV scan . . . 74
4.6.2 Efficiency measurement . . . 75
4.6.3 Rate capability measurement . . . 76
4.7 Offline detector monitoring . . . 80
4.7.1 Integrated charge . . . 81
4.7.2 Discharges . . . 82
4.8 Conclusions . . . 83

5 CMS ME0 performance with MIPs **87**
5.1 Setup and electronics . . . 87
5.1.1 Trigger system . . . 88
5.2 Offline alignment . . . 88
5.3 Time resolution measurements . . . 89
5.3.1 Digi timing . . . 91
5.3.2 Rechit timing . . . 92
5.3.3 Segment timing . . . 92
5.4 Conclusions . . . 94

Conclusion **97**

A Model for dead time behavior **99**

B Monte Carlo toy for dead time **101**

C High Voltage compensation at GIF++ test beam **105**

Bibliography **109**

Introduction

Micro-Pattern Gaseous Detectors (MPGD) have been developed, starting from the end of the '80s [1], as an alternative to the traditional gaseous detectors based on the Multi-Wire Proportional Chambers (MWPC) technology [2]. Thanks to their good spatial and time resolution, high rate capability, long lifetime, and low cost-to-surface ratio, MPGDs have been introduced in various fields, such as high energy physics at colliders, astroparticle physics, and medical applications. Among the various types of MPGDs, GEM detectors (invented by F. Sauli in 1997 [3]) have gained a particularly good reputation thanks to their ease of manufacturing and flexible geometry. As a result, they were installed very soon in large HEP experiments as charged particle trackers, in the COMPASS experiment (started in 2002) and in the LHCb experiment (started in 2010) at CERN. These first applications proved GEM detectors' successful performance and, consequently, granted them a central role in the future of LHC.

The LHC (Large Hadron Collider) [4] is a 27 km-long circular accelerator located at CERN, 175 m beneath the surface of the Earth. Along LHC, two hadron beams (protons or heavy ions) are accelerated until they reach the required energy and are collided together, in order to produce significant particles. The collider has four crossing points where the accelerated particles collide, and, in correspondence with these points, large-area experiments are installed to detect and analyze the products of the collisions. The 4 mentioned experiments are: ATLAS, CMS, Alice, and LHCb. LHC first collision occurred in 2010, and it has been running smoothly at world-record proton-proton center-of-mass energies from 7 TeV (Run 1, in 2010) up to 13 TeV (Run 2, from 2015), with a luminosity exceeding $10^{34}\,\mathrm{cm}^{-2}\,\mathrm{s}^{-1}$. The Standard Model was tested in an unprecedented energy regime and with high precision. The Higgs boson was discovered through its two-photon and four-lepton decay modes. New 'Beyond the SM' (BSM) particles have been searched for in many channels, and stringent limits have been set, but so far no new physics was found. The increasing need to extend the sensitivity for new physics searches brought to the undertaking of a major upgrade of the LHC, the High Luminosity LHC (HL-LHC) [5], which should be operational from the beginning of 2029. This project is aimed at increasing tenfold the integrated luminosity of the accelerator ring and at raising the center-of-mass energy for proton-proton collisions from the current 13 up to 14 TeV.

In the new radiation environment characterizing HL-LHC hadron collisions, the 4 large-area experiments along the accelerator ring need to be upgraded to sustain the higher particle rate and maintain their excellent performance. In particular, the CMS detector foresees a set of innovations, namely the Phase-2 upgrade, to face the challenge introduced by the new harsh environment expected in HL-LHC. The Phase-2 upgrade includes the enhancement of both the electronics and detection apparatus. In this scenario, MPGDs, and, in particular, GEM detectors will take on a major role in the CMS muon system upgrade. Due to their high-rate capability and slow aging, 3 stations of GEM detectors are planned to be installed: GE1/1, GE2/1, and ME0 [6]. Among these three stations, ME0 will be located in the most challenging region of the apparatus. ME0 position is currently occupied by the HCAL, but it will be freed

with the installation of the new High Granularity Calorimeter (HGCal). In particular, ME0 will be the closest detector of the muon system to the interaction point, and, consequently, it will receive the highest rate of background particles. This environment requires the ME0 performance to be validated under working conditions as similar as possible to the HL-LHC background particle rate.
To meet the challenges introduced by the HL-LHC project, in 2015 a new facility has been equipped, the Gamma Irradiation Facility (GIF++) [7], providing charged particle beams the SPS, combined with a 14 TBq ^{137}Cs source.

This thesis is organized in 5 chapters, and their content is here summarized. The first chapter provides an overview of the processes of interaction of particles with the matter and of the working principles of gaseous detectors, together with a description of the traditional detector technologies and of the innovative MPGDs, with a particular focus on the GEM detectors' performance.
The second chapter briefly outlines the characteristics of the CMS experiment and the major modifications foreseen, accordingly to the Phase-2 upgrade. Particular emphasis will be given to the upgraded muon system and the role the new GEM stations will have in it.
The third chapter focuses on the specific characteristics of the triple-GEM detectors, planned to be used in the ME0 station. ME0 chambers will be described in terms of module design and readout architecture. Then, the main calibration and configuration scans for the GEM system readout electronics are presented.
The fourth chapter discusses the rate capability measurements of the ME0 prototype composed of four stacked triple-GEM chambers. The data analyzed have been collected during a test beam campaign at the GIF++ at CERN North Area.
Finally, the fifth chapter presents the integration of the final-design prototype of the six-layered ME0 stack, showing an offline alignment procedure of the six chambers in the stack and measurements of the time resolution of both the six single chambers and the overall detector. The analysis has been performed taking data both with cosmic rays and in a test beam at the CERN H4 line.

Chapter 1

Gas Electron Multipliers

The present chapter provides a description of the basic mechanisms of particle-matter interactions, laying the groundwork for the examination of gaseous detectors, with a particular emphasis on Gas Electron Multipliers (GEMs). By elucidating the mechanisms through which particles interact with various materials, this chapter aims to discern the principles guiding the operation and optimization of these pivotal instruments. The discussion is mainly based on references [8, 9, 10, 11].

1.1 Interaction of particles with matter

Particle detection is based upon sensing particles, charged or neutral, exploiting their interaction with matter. Different mechanisms of interaction can occur depending on the nature of the particle to be detected, its dynamics (e.g. its energy), and the medium it is passing through. In this section, the main mechanisms of interaction of charged particles and photons will be discussed: respectively ionization and excitation for charged particles and photon scattering and absorption. The emphasis on this particular topic stems from its fundamental relevance to the subsequent discussions and analyses presented throughout this work.

1.1.1 Energy loss of charged particles by ionization

When penetrating a medium, charged particles lose energy by ionization and excitation of the medium's atoms or molecules. This is the dominant energy loss process of charged particles up to very high particle velocities when radiation effects start to play a role. The energy loss per path length is described by the Bethe-Bloch formula [12]. The first calculations using classical methods were already published by Bohr in 1913 [13]. In the 1930s Bethe and Bloch provided a quantum mechanical treatment of the problem, the results of which are to a large extent still valid today. The Bethe-Bloch formula of the stopping power by ionization, $S.P._{ION}$, is the following:

$$S.P._{ION} = -\left\langle \frac{dE}{dx} \right\rangle = K \frac{Z}{A} \rho \frac{z^2}{\beta^2} \left[\frac{1}{2} ln \frac{2 m_e c^2 \beta^2 \gamma^2 T_{max}}{I^2} - \beta^2 - \frac{\delta(\beta\gamma)}{2} - \frac{C(\beta\gamma, I)}{Z} \right] \tag{1.1}$$

The various quantities in the formula are defined as follows:

- $K = 4\pi N_A r_e^2 m_e c^2 = 0.307\,\mathrm{MeV\,cm^2\,mol^{-1}}$, using the classical electron radius;
- z, β are charge and velocity of the projectile particle;
- Z, A are the atomic number and atomic mass (g/mol) of the medium, respectively;

- T_{max} is the maximum energy transfer to a shell electron occurring in a central collision.

- δ is the so-called *density correction*, relevant at high energies;

- C/Z is a *shell correction*, important for small values of β.

Equation 1.1 is valid for particles *heavy* with respect to their target (i.e. atomic electrons), namely all particles except electrons and positrons. The Bethe-Bloch formula describes how particles are stopped in matter. The energy loss in matter is hence also called *stopping power*. The stopping power determines the range, i.e. the distance travelled before stopping, of a particle in matter or the energy lost after penetration of a layer of material. Figure 1.1 shows the mean energy loss $\langle dE/dx \rangle$ as a function of the energy of the incoming particle for a typical example (μ^+ on Cu). At low energies, the $1/\beta^2$ term is dominant, while at high energies the $ln\gamma$ term prevails. In between those regions, there is a broad minimum around $\beta\gamma \approx$ 3-3.5, corresponding to a stopping power of approximately $1.5\,\mathrm{MeV}\cdot\mathrm{g/cm^2}$. Particles in this kinematic range are called *minimum-ionizing particles* (*mip*s). Since the increase in dE/dx for energies corresponding to $\beta\gamma >$3.5 is only moderate compared to the steep rise $\propto 1/\beta^2$ towards energies lower than the minimum, it is common practice to use the term *mip* for all charged particles with energies larger than those at the minimum.

Furthermore, at higher energies, an increase in the stopping power is determined by the radiative losses. In fact, charged particles not only lose their energy by ionization (as described by Bethe-Bloch formula), but also by radiating electromagnetic quanta. The latter is called *Bremsstrahlung* process. Computations employing relativistic quantum electrodynamics yield a proportionality to Z^2E/m^2 of the radiative power. The characteristic E/m^2 dependence implies that for energies below a few hundreds of GeV this process is only significant for electrons and positrons. Accordingly, critical energy E_C can be introduced as the point in energy at which both energy loss curves intersect:

$$S.P._{ION}(E_C) = S.P._{RAD}(E_C)\ . \tag{1.2}$$

For electrons and positrons, due to their much smaller mass compared to heavier particles, energy loss by photon radiation (Bremsstrahlung) becomes relevant already at relatively small energies. Since ionisation and bremsstrahlung of electrons or positrons can to a good approximation be treated independently, for the purposes of this work only the energy loss by ionization is treated here. The ionisation energy loss by electrons and positrons differs from that by heavy particles due to kinematics, spin and their identity or respectively their antiparticle character with respect to the electrons of the medium. For positrons, a complete loss via e^+e^- annihilation into photons must also be accounted for. Generally, two regimes of energy transfer can be distinguished:

- in the regime where the atomic energy levels cannot be neglected energy loss is treated by averaging, as done above for heavy particles;

- in the regime with large energy transfers discrete processes, that is Møller scattering ($e^-e^- \rightarrow e^-e^-$) or Bhabha scattering ($e^+e^- \rightarrow e^+e^-$), are computed.

Figure 1.2 shows the comparison of energy loss by protons and electrons in silicon. The difference near the minimum of the ionisation is about 10 %, increasing by small amounts towards smaller and larger velocities.

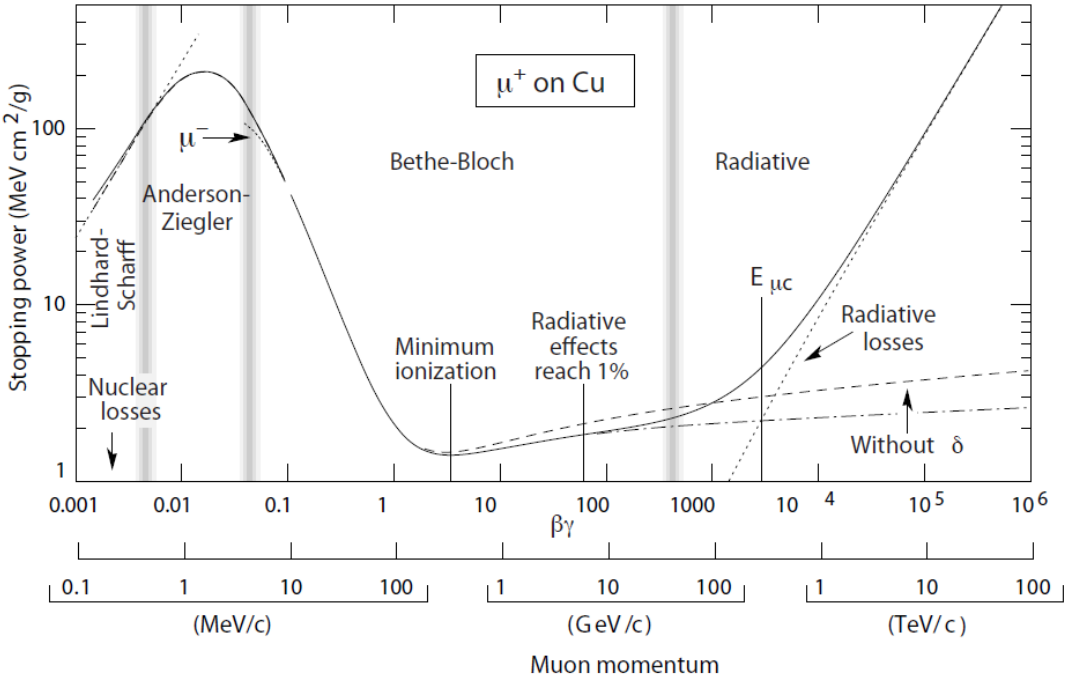

FIGURE 1.1: Energy loss for positive muons in copper (taken from [14]). The vertical bands separate regions with different theoretical descriptions. The center marks the validity region of the Bethe-Bloch formula 1.1. At high energies where Bremsstrahlung dominates the drawn curves show the total energy loss (solid), the loss by radiation (dotted) as well as by ionization without (dashed) and with (dash-dotted) the inclusion of the δ term in 1.1. The region at low energies labelled "Anderson-Ziegler" is described by an empirical fit to measured data. The region below this, labelled "Lindhard-Scharff", is based on a theoretical model which yields an energy loss dependence roughly proportional to β (dashed line). At the lowest non-ionizing energy loss caused by elastic nuclear recoil dominates. At low energies the energy loss is smaller for negative than for positve particles attributed to higher order corrections and indicated here by the curve labelled "μ^-".

1.1.2 Interaction of photons with matter

As for photon interaction with matter, particle detectors exploit mainly the photoelectric effect, the Compton effect and the pair production. These three processes, indeed, dominate at photon energies above the ionization threshold. The occurrence of one over the others depends on the energy of the impinging photon and on the interacting medium. At low energies, Thomson and Rayleigh scattering also play a role. Thomson scattering is a low-energy photon scattering off free charges. The coherent scattering off of a whole atom without shell excitation or ionization is called Rayleigh scattering.
As a result of the above interaction processes, photons are absorbed or scattered off their original direction, with a probability proportional to the path length dx in the medium. The number of photons in a beam passing towards a thin medium follows an exponential law, known as Lambert law [8]:

$$N(x) = N_0 e^{-\mu x} \,, \tag{1.3}$$

where N_0 is the number of photons entering the medium, x is the depth travelled though the medium and μ is the mean free path (or *absorption length*).

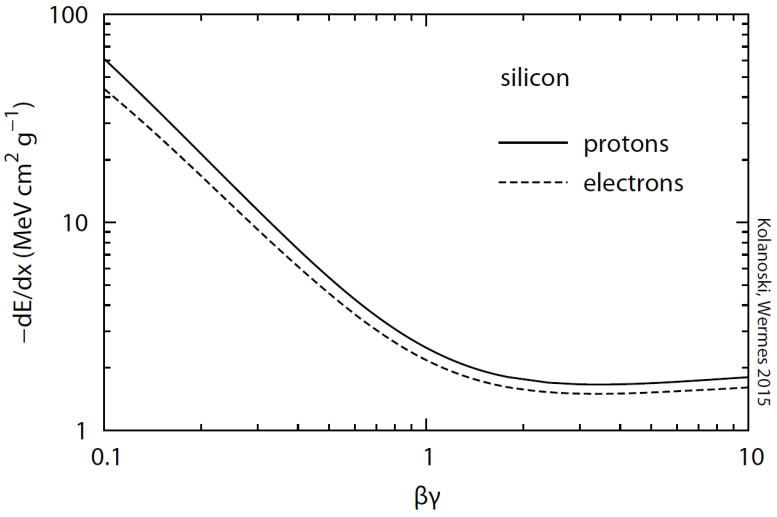

FIGURE 1.2: Comparison of the energy loss by electrons (excluding Bremsstrahlung) and by protons in silicon. The curves have been computed via the programs ESTAR and PSTAR [8].

The **photoelectric effect** is the dominant photon interaction process at energies in the lower keV range, typically above 1 keV. In the photoelectric effect the photon transfers its complete energy onto an atom which, then, releases the absorbed energy by emitting an electron into the continuum. The atom absorbs the recoil momentum and is ionized after the reaction. In order for the photoelectric effect to take place, the energy E_γ of the photon must exceed the binding energy E_B of the electron ($E_\gamma > E_B$); the energy surplus is transferred as kinetic energy to the electron: $T = E_\gamma - E_B$. The recoil energy transferred to the atom can be neglected due to the atom's large mass. The cross section for photoeffect rapidly drops with increasing photon energy (at fixed photon energy) and strongly increases with increasing Z. For a given photon energy the probability for absorption is largest for the most strongly bound inner shell electrons, for which the energy surpasses the threshold for that shell. This is why jumps in the absorption cross section, so-called absorption edges, are observed at photon energy $E_\gamma = E_B^i$, $i = K, L, ...$

The **Compton effect**, or incoherent scattering, is the scattering of a photon off a free or quasi-free electron. A shell electron is termed "quasi-free" in this context when the energy of the incoming photon is substantially larger than the electron's binding energy ($E_\gamma \gg E_B$). A scattering process is called Compton scattering if the electron is kicked out of the atom, carrying away the recoil momentum. There is also the possibility that, even at high photon energies, the electron remains in the atom-shell. In this case, the whole atom takes the recoil and the scattered photon's energy is nearly the same as the initial energy, independent of the scattering angle. The latter process is called 'coherent photon scattering' and becomes strong at lower energies. The Compton effect is dominant in an extended energy region around 1 MeV. The extent of this region is much larger at low Z of the medium than at high Z.

Pair production process refers to the conversion of a photon into an electron-positron pair in the Coulomb field of a charge. For this process to occur, the energy of the photon must be larger than twice the electron mass plus the recoil energy transmitted to the field-producing charge. Except for very light elements, pair production occurs predominantly in the Coulomb field of the nucleus. For nuclei, the recoil energy is practically always negligible such that the threshold energy for pair

production is $2m_ec^2$. The cross-section for pair production increases as Z^2 and is approximately constant at large photon energies ($\sim 1\,\text{GeV}$).
Figure 1.3A shows regions in the (E_γ, Z)-plane in which a process is dominant in each case. For a given Z value the strong decline of the photoeffect with energy leads to the fact that the Compton effect becomes dominant from a certain energy onwards. It is then taken over by pair production starting at its threshold and becoming constant at high energies. The stronger dependence on Z of the photoeffect and pair production compared to Compton scattering is responsible for the fact that the region in which the Compton effect dominates becomes smaller with increasing Z. In particular, Figure 1.3 shows the total cross section for photon interaction in a gas mixture Ar/CO_2 (70/30), as of particular interest for the successive analysis performed throughout this work. All the contributions to the total cross section are shown, but as apparent the most relevant ones are, at increasing energies, respectively Photoelectric absorption ($\lesssim 0.1\,\text{MeV}$), Compton scattering ($\lesssim 10\,\text{MeV}$) and, finally, pair production in the nuclear field.

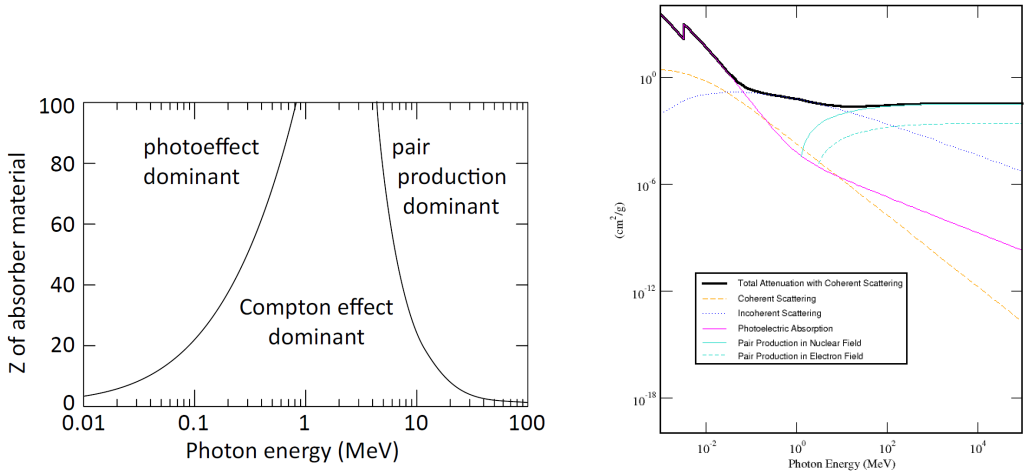

FIGURE 1.3: (A) Regions in the (E_γ, Z) plane in which the different photon absorption processes are dominant. (from [8]). (B) Cross section for photon interaction in a gas mixture Ar/CO_2 (70/30) (from NIST Xcom).

1.2 Working principle of gaseous detectors

Gaseous detectors [8], as the name immediately suggests, employ gas as an active medium, in such a way that particles traversing the detector interact with the atoms, or molecules, of the gas, thus either exciting or ionizing them. In particular, when one atom (or molecule) of the gas gets ionized, two separate charges are created: an electron and a positive ion. A gaseous detector must be composed of: an **active volume**, namely the gas, whose atoms (or molecules) get ionized, **field-defining electrodes** to generate an external electric field, and, finally, **readout electrodes**, on which the drifting charges induce the electric signal, that, once measured, gives evidence of the passage of a particle. Even if drifting and readout electrodes have different functions, they can often physically coincide in a detector.

1.2.1 Primary ionization

The processes of transfer of the energy from a traversing particle to a suitable medium are described in Section 1.1. For charged particles, in particular, the largest fraction of energy dissipated in matter is due to electromagnetic interactions between the Coulomb fields of the projectile and of the molecules in the medium, and the average energy loss per unit length is given by the Bethe-Bloch formula. In particular, the slowing down in matter is mainly due to multiple inelastic processes of excitation and ionization [9]. Then, when dealing with charged particles the actual average energy loss needed to create an electron-ion pair (W_I) is larger than the ionization potential of the atom (or molecule) (E_I), because part of the particle energy is lost via non-radiative mechanisms. The table in Figure 1.4 summarizes physical parameters useful to estimate the energy loss and ionization yields of fast charged particles in gases commonly used in proportional counters [15].

Gas	Density mg cm^{-3}	E_x eV	E_I eV	W_I eV	$dE/dx\|_{min}$ keV cm^{-1}	N_P cm^{-1}	N_T cm^{-1}
Ne	0.839	16.7	21.6	30	1.45	13	50
Ar	1.66	11.6	15.7	25	2.53	25	106
Xe	5.495	8.4	12.1	22	6.87	41	312
CH_4	0.667	8.8	12.6	30	1.61	37	54
C_2H_6	1.26	8.2	11.5	26	2.92	48	112
iC_4H_{10}	2.49	6.5	10.6	26	5.67	90	220
CO_2	1.84	7.0	13.8	34	3.35	35	100
CF_4	3.78	10.0	16.0	54	6.38	63	120

FIGURE 1.4: Table of the properties of the most common gases. (from [15])

Since all the primary ionization events are independent of each other, statistically the number of electron-ion pairs, k, generated by primary ionization follows the Poissonian distribution:

$$P(k, n_T) = \frac{n_T^k}{k!} e^{-n_T} ,$$

where n_T is the average number of electron-ion pairs generated by primary ionization.

An easy calculation can be performed to estimate the number of electrons generated on average per unit length by a MIP traversing a gas, for example, a mixture of Ar:CO_2 (70%:30%). Considering the weighted average of the values listed in the table above, the total number of electron-ion pairs generated by a traversing MIP would be:

$$n_T = \frac{\langle dE/dx \rangle}{W_I} = \frac{2.78 \times 10^3}{27.7} \text{cm}^{-1} = 100\,\text{cm}^{-1}$$

This amount of charge would result in a signal too weak ($\sim 10^{-2}$ fC cm^{-1}) to be sensed with any measurement apparatus. To allow particle detection, this signal must be amplified and, for this to happen, collisional excitation and subsequent charge multiplication can be exploited.

1.2.2 Drift and diffusion

As for the active volume, the motion of the charges inside the gas represents a crucial argument for the functioning of such detectors. In a volume of gas, once ions and electrons are released, they swiftly lose their energy in multiple collisions with the surrounding molecules until they get neutralized either by recombination in the gas or at the walls [9]. In absence of external fields and inelastic collision processes, ions and electrons released in a gas behave like neutral molecules, with properties described by the classic kinetic theory of gases. Accordingly, a localized distribution of molecules or ions diffuses symmetrically by multiple collisions following a Gaussian law, with a standard deviation for linear and volume diffusion, respectively, given by:

$$\sigma_x = \sqrt{2Dt} \text{ and } \sigma_V = \sqrt{6Dt}\,, \tag{1.4}$$

where D denotes a diffusion coefficient. The values of the diffusion coefficient D, mean free path between collisions λ, and average velocity v of atoms and molecules in their own gas depend on the gas itself and its temperature and pressure. In the table in Figure 1.5, classical values of the aforementioned properties are listed for some of the most frequently used gas types.

Gas	λ(cm)	v(cm/s)	D(cm^2/s)
H_2	1.8×10^{-5}	2×10^5	0.34
He	2.8×10^{-5}	1.4×10^5	0.26
Ar	1.0×10^{-5}	4.4×10^4	0.04
O_2	1.0×10^{-5}	5.0×10^4	0.06
H_2O	1.0×10^{-5}	7.1×10^4	0.02

FIGURE 1.5: Classic values of the mean free path between collisions, velocity and diffusion coefficient for atoms and molecules at NTP. (from [16])

At the thermal equilibrium, electrons, due to their lower mass, are characterized by a thermal velocity, that is several orders of magnitude higher than that of ions, with an average value, at room temperature, of about 10^7 cm/s. Thermal diffusion occurs with a correspondingly larger value of the diffusion coefficient.
To avoid recombination and neutralization of the charges generated by the ionizing encounters with the traversing particles, an electric field must be applied to the gas volume. Indeed, when an electric field is applied to the gas volume, a net movement of ions and electrons, respectively along the field direction and opposite to it, is observed. The average velocity of this motion is named *drift velocity* $w^{\pm}$, but its dependence on the intensity of the electric field changes whether ions or electrons are considered. For ions, drift velocity is linearly proportional to the electric field up to very high values of E. It is therefore customary to define a quantity μ, the mobility of the charge, as:

$$\mu^+ = \frac{w^+}{E}\,. \tag{1.5}$$

The value of the mobility is specific to each type of charge moving in a given gas, and depends on pressure and temperature; it is usually measured in units of 10^{-8} m^2 s^{-1} V^{-1}, except for H^+, for which it is ten times larger.
For electrons instead, except for very low fields, the mobility of electrons is not constant: because of their small mass, electrons can substantially increase their energy

between collisions with the gas molecules. In a simple formulation [17], the electrons drift velocity:

$$w^{-} = k\frac{eE}{m}\tau \,, \tag{1.6}$$

where τ is the mean time between collisions, and the value of the constant k, between 0.75 and 1, depends on assumptions about the energy distribution of electrons. The compilation in Figure 1.6 for several pure gases illustrates the wide span of values and shape of the field-dependence of the drift velocity. A classical argument allows

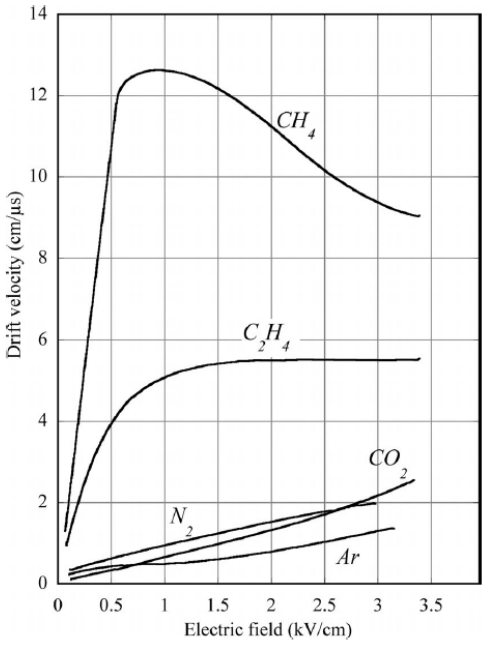

FIGURE 1.6: Electron drift velocity as a function of field in pure gases at NTP. (from [10])

one to obtain the following relationship between mobility and diffusion coefficient (Nernst-Townsend formula) for ions (and thermal electrons):

$$\frac{D}{\mu} = \frac{kT}{e} \tag{1.7}$$

where D is the diffusion coefficient and e the electron charge.
A similar relationship can be obtained for electrons considering that the extent of diffusion depends on the gas, but also on the electric field intensity, due to the increase of electron energy. Introducing a phenomenological quantity ϵ_k, named characteristic energy, the expression 1.7 is modified:

$$\frac{D}{\mu} = \frac{\epsilon_k}{e} \tag{1.8}$$

The diffusion of ions and electrons strongly affects the detector performance in terms of spatial resolution, as the larger the diffusion the less precise is the localization of the particle.

1.2.3 Charge multiplication

When the intensity of the external electric field inside the gas volume exceeds a few kV cm^{-1}, the primary electrons, produced via primary ionization, can acquire enough energy between two collisions to ionize, in their turn, the atoms (or molecules) of the gas, creating electron-ion pairs, while the primary electron continues its motion in the gas. When the mean free path for ionizing collisions is small compared to the gas layer thickness, the secondary electrons soon acquire sufficient energy from the field to ionize further. This leads to a rapid growth of an electron-ion avalanche, and constitutes the basic mechanism of signal amplification in gas proportional counters. The ionization cross-section increases rapidly above the threshold and for most gases has a maximum at an energy 100 eV.
The mean free path for ionization λ is defined as the average distance an electron has to travel before having an ionizing collision; its inverse, $\alpha = \lambda^{-1}$, is the first Townsend coefficient, and represents the average number of electron-ion pairs produced per unit length of drift; it relates to the ionization cross section through the expression $\alpha = N\sigma_{ion}$, where N is the number of molecules per unit volume. As for other quantities in gaseous electronics, the Townsend coefficient is proportional to the gas density and therefore to the pressure.
Consider an electron released in a region of the electric field **E**=**E**(x). After a mean free path $1/\alpha(x)$, one electron-ion pair will be produced, and the two electrons continue their drift generating, after another mean free path, two more ion pairs, and so on. If n is the number of electrons in a given position, the increase in their number after a path dx is $dn = n\alpha(x)dx$; integrating:

$$M = \frac{n}{n_0} = e^{\int_{x_1}^{x_2} \alpha(x)dx} , \tag{1.9}$$

where M represents the charge multiplication factor, x_1 and x_2 are the initial and final coordinates of the multiplication path.
Due to the very large difference in mobility and diffusion of electrons and ions the process of charge multiplication results in a characteristic drop-like charge distribution, or avalanche, with all electrons at the front and a slow ions trail. One of the possible parametrization for the Townsend coefficient consists of assuming it to be proportional to the average electron energy ϵ:

$$\alpha = kN\epsilon . \tag{1.10}$$

The multiplication factor cannot be increased at will. Secondary ionization processes in the gas and on the walls produced by photons emitted in the primary avalanche spread the charge over the gas volume; the space charge-induced distortions of the electric field, strongly increasing in front of and behind the multiplying charge, enhance the formation of secondary avalanches and may cause transition of the proportional avalanche to a streamer and eventually, if not damped by the detector geometry or by a reduction of the field, the streamer can propagate through the whole gas gap, leading to a spark breakdown. A qualitative description of the main processes leading to the avalanche-streamer transition is shown in Figure 1.7. A phenomenological limit to the proportional avalanche multiplication before the transition is given by the empirical condition (Raether's limit):

$$\alpha x < 20 . \tag{1.11}$$

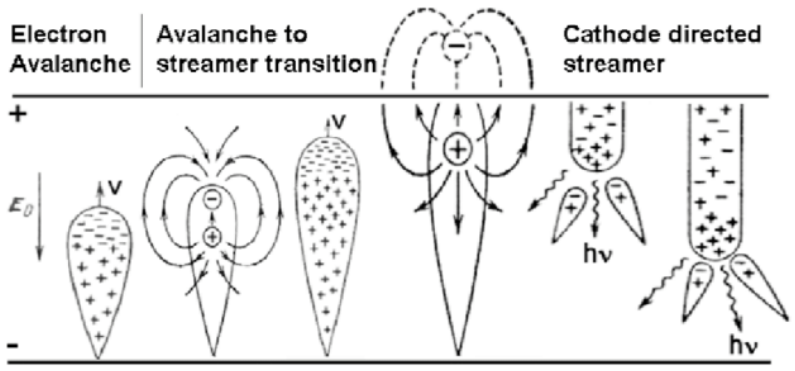

FIGURE 1.7: Evolution of electron avalanche in discharge gap, showing avalanche development, avalanche-to-streamer transition, and streamer propagation. (from [18])

Practically, once the total voltage supplied by the drifting electrodes is fixed, the electric field depends on their geometry. The two traditional geometries employed for gaseous detectors are the cylindrical geometry and the parallel plate geometry: the first being characterized by an electric field that increases approaching the central wire, and the second by a uniform electric field. As a consequence, in the cylindrical geometry the avalanche starts developing when the charges get close enough to the central wire, while in the parallel plate geometry, the avalanche can occur in any point inside the active volume. This main difference implies that the first is preferred for precise tracking, while the second for precise timing. As an emblematic case of cylindrical geometry, in Section 1.3, the detecting mechanism of the single wire proportional chamber will be discussed. Then, a brief description of the two main detector technologies most widely spread in HEP experiments nowadays is provided: respectively Multi-Wire Proportional Counters for the cylindrical geometry and Resistive Plate Chambers for the parallel plate geometry.

1.2.4 Signal formation

In ionisation detectors the formation of signals that can be electronically processed starts with the energy deposit of the particle in the detector volume. Consequently, charged pairs are created and separated by an electric field generated by the drifting electrodes. Afterwards, the moving charges induce an accumulation of charges on the electrode surfaces, which is recorded either as a charge, current or voltage signal [8].
In a detector made only of conductive materials, the signal induced on a readout electrode by a moving charge is determined by the weighting field $\mathbf{E_w}$. The weighting field is calculated in a geometry in which the voltage of the readout electrode is set to an arbitrary value V_0. All the other electrodes are grounded and the moving charge is removed; once $\mathbf{E_w}$ is known, the signal induced by a single point charge q is determined by the Ramo-Shockley theorem [19, 20]:

$$i(t) = \frac{q}{V_0}\mathbf{E_w} \cdot \mathbf{v}(t) \, ,$$

where $\mathbf{v}$ is the velocity vector of the charge. The current signal induced by an avalanche is the sum of the currents of the single charges in the avalanche; the signal ends when all the charge is either neutralized or collected.

1.3 Examples of gaseous detectors

1.3.1 Single-Wire Proportional Chamber

In Figure 1.8A, a typical single-wire proportional chamber (or tube counter) is depicted. The anode is a thin wire of radius a on the cylinder axis and the cathode is the metallic wall of the cylinder, whose radius is b. In most of the cylindrical gas volume, the electric field is not enough to trigger avalanche processes, so electrons drift toward the anode and ions toward the cathode. Since the electric field inside the gas varies with $1/r$, when electrons get close to the wire (usually at a few wire radii), the electric field becomes intense enough to trigger multiplication processes. Figure 1.8 shows a typical dependence of detected charge on anode voltage, for two sources of radiation differing in primary ionization density passing through a tube counter.

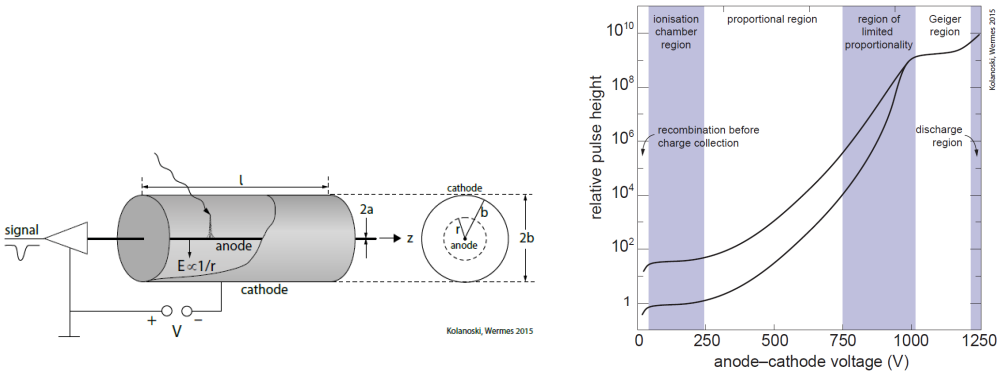

(A) (B)

FIGURE 1.8: (A) Principle of a counting tube. The plot delineates the relevant geometrical parameters and the cylinder coordinates r and z which are used for the calculation of the field and the detector capacitance (the azimuth is not shown since it is not relevant for the calculations). (B) Schematic representation of the dependence of the output signal of a counting tube on the anode–cathode voltage. The characteristics are shown for two particles with different values of energy released by primary ionization. The lower curve is normalised such that the gas amplification can be read off the vertical axis. The numerical values for amplification and voltage are used as examples; in concrete cases they depend strongly on the electrode arrangement and the used gas. The different amplification regions are discussed in the text. (from [8])

At very low voltages, charges start being collected, but recombination is still the dominant process; at higher fields, full charge collection begins, and the counter is said to operate in the ionization chamber mode. Increasing the voltage further, and above a threshold value V_T, the electric field close to the surface of the anode gets large enough to initiate a process of charge multiplication; gains in excess of 10^5-10^6 can be obtained, with the detected charge proportional, through the multiplication factor, to the original deposited charge. At even higher voltages, however, this proportionality is gradually lost, as a consequence of the electric field distortions due to the large charge density building up around the anode; the region of limited proportionality ends in a region of saturated gain, where the detected signal is independent of the original ionization density. When the voltage is further increased, various secondary processes set in, resulting in breakdown or, under special conditions (low pressure, poorly quenched gases) in a photon-mediated propagation of the multiplication over the full length of the anode, the so-called Geiger-Muller operation.

1.3.2 Multiwire Proportional Chambers

The MWPC, developed by George Charpak at CERN in the late 1960s [2], consists of a set of parallel, regularly spaced thin anode wires between two cathode planes. On application of a symmetric difference of potential between anodes and cathodes, electric field lines and equipotentials develop as shown in Figure 1.9A. Charges released by ionization in the gas volume drift towards the electrodes, electrons to the anodes and ions to the cathodes. On approaching the thin wires, the electrons accelerated by the increasing field, undergo inelastic collisions with the gas molecules, starting an avalanche. The process continues until the amplified electron charge reaches the anodes. The multiplication process initiates typically at a distance of few wire radii, ensuring a proportional response to the ionization released in most of the gas volume. With a proper choice of geometry and gases proportional gains up and above 10^6 can be achieved, permitting the detection of small amounts of primary charges. Efficiently operating at radiation fluxes up to $10^4\,\mathrm{mm}^{-2}\,\mathrm{s}^{-1}$, MWPCs were quickly adopted to instrument the new generations of detectors in particle physics experiments. Limited originally in localization properties by the wire spacing due to electrostatic stability (1 to 2 mm), the development of the induced cathode signals readout method permitted to reach position accuracies well below a millimeter. MWPC time resolution typically lies in the range of 100-10 ns, depending on the gas mixture [21].
This detector type and variants of it, like the drift chamber and time projection chambers, have been crucial for progress in particle physics until today. Nowadays, they are still used for tracking in the muon systems of large-area experiments, like LHCb and CMS (DTs and CSCs), and for particle identification, as in ALICE (TPC).

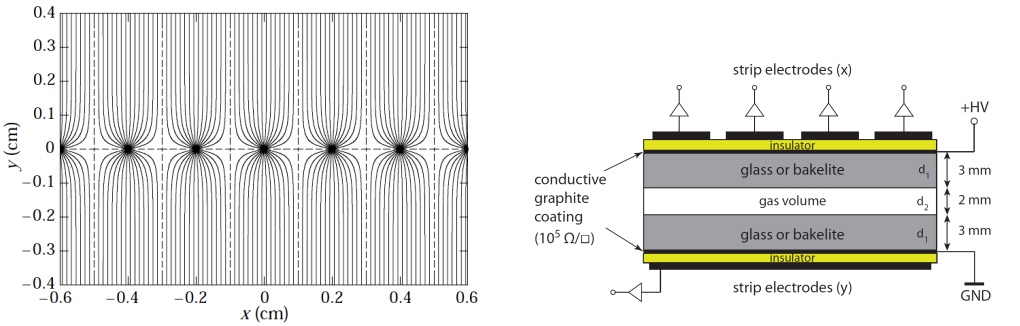

(A) (B)

FIGURE 1.9: (A) Field lines in a MWPC detector, calculated by Garfield Program [22] (B) Layout of an RPC. The high voltage is applied between the two high-resistive electrodes (glass or bakelite) via conductive graphite layers. The signals are induced onto readout strips with different orientation on top and bottom. The strips are insulated from the voltage electrodes. Typical dimensions are given for illustration (from [8]).

1.3.3 Cathode Strip Chambers

Cathode Strip Chambers are MWPCs with a cathode segmented in strips and the signal induced by the charge avalanche on a strip is recorded. The cathode strip readout provides a further coordinate in addition to the one provided by the anode readout. In particular, if the detector response contains information about the

amount of detected charge, as given for analog readout, a charge center of gravity can be determined; its position is a better estimate for the hit coordinate than the center of the strip. The position of the center of gravity is reconstructed according to:

$$x_{c.o.g.} = \frac{\sum S_i x_i}{\sum S_i}$$

where the x_i is the coordinate of the center of the i-th strip and S_i the corresponding signal height measured on it. The signals on the strips are assumed to follow a certain distribution, for example, a Gaussian. The signals are then integrals of this distribution over the strip width. The achievable resolution depends on the signal distribution function, in particular on its width relative to the strip width. This method allows to reduce the spatial resolution of CSC down to $\sim$100 µm, as measured, for example, in CMS CSCs (strip pitch $\sim$ 8.4 - 16 mm) [23].

1.3.4 Drift Chambers

Drift chambers are a further development of MWPCs. In a drift chamber, the position where a particle traversed the detector is determined by the drift time of the electrons measured from the generation of ionisation at the time t_{start} to the arrival at the anode at the time t_{stop}. The basic formula is an integral over the drift velocity v_D:

$$x = \int_{t_{\text{start}}}^{t_{\text{start}}} v_D(t)dt \ .$$

The drift velocity is expressed as a function of the time, because it may vary with the local field along the trajectory of the moving charges. Unlike MWPCs (and CSCs), for a drift chamber, the position resolution is no longer directly dependent on the spacing of the signal electrodes but rather on the precision of the time measurement of the electron drift until the arrival at the anode. Since drift distances can be much larger than the wire distances in MWPCs, in general the number of readout channels and the material per area that a particle has to traverse are reduced. At the same time, the position resolution improves as compared to MWPCs. The best resolutions reached with drift chambers lie at about 20 µm, however for large volume detectors the typical values lie more in the range 100-200 µm, like in CMS Drift Tubes [24].

1.3.5 Resistive Plate Chambers

Resistive Plate Chambers (RPC) [25, 26] are gaseous detectors based on the parallel plate geometry, whose basic structure is depicted in Figure 1.9B. The key point of operation is a sufficiently high electric field such that instant avalanche multiplication sets in at any point of the gas volume with negligible drift before, thus fulfilling the conditions for good time resolutions and fast trigger decisions. The plates are made of a highly resistive material with a resistivity of 10^8-$10^{12}\,\Omega \cdot$ cm (e.g. glass or bakelite) and have a typical distance of about 2 mm.
A high voltage of about 10 kV is applied between the plates. On the sides facing away from the gas volume, the plates are coated with low-conductivity graphite with a surface resistivity of $R_{foil} \approx 10^5\,\Omega$. Because of the high resistivity of the (bakelite or glass) electrodes, the charge drain is delayed and therefore a counter-field builds up, limiting the discharge in time and strength. The duration of the discharge is typically 10 ns. The time for the restoration of the electric field in the region of discharge, however, last typically around 10 ms, that is, the time for the charge created near the glass or bakelite electrode to "decay away", $\tau_{recharge} = RC$.

RPCs can be operated in streamer mode or, with somewhat reduced voltage, in avalanche mode with different performance properties. Historically, RPCs were first operated only in streamer mode. In streamer mode the electric field inside the gas gap is so intense ($\sim$10 kV mm^{-1}) that traversing charged particles generate limited discharges. This allows for a detection efficiency 95% and time resolution of $\sim$1 ns but does not allow for rate capability exceeding 200 Hz cm^{-2} since the charges of the streamers are large. No signal amplification via electronics is needed in this mode because signals are large enough to be read out directly. However, the rate is low due to the long recovery time, caused by the large charge deposited on the resistive plates. This feature makes streamer mode RPCs useful for low-rate measurements, such as cosmic rays or neutrino experiments, but unpractical for high-rate regimes, leading to the development of an alternative mode of operation for use at LHC detectors: the avalanche mode.
When operated in avalanche mode [27, 28], lower electric fields ($\sim$5 kV mm^{-1}) can be used to reduce the size and charge of the avalanches, leading to an improved rate capability of about 1 kHz cm^{-2} [29]. In the avalanche mode the electric signals induced on the strips are $\sim$1 mV, so dedicated electronic amplifiers are necessary to compensate for the loss of gas amplification to process the signal. The readout planes on the outside are separated from the conducting graphite coating by insulating layers. The readout plane picks up the induction signals of the avalanche in the gas volume. It is usually subdivided into parallel conducting strips, which can be oriented on both sides in different directions in order to obtain a position measurement.
The choice of the gas mixture for an RPC is, in general, a difficult task; RPCs require for efficient operation the use of gas mixtures with a somewhat demanding combination of characteristics:

- high density of primary ion-electron clusters, to assure high efficiency;
- relevant "quenching" properties, to reduce the photon feedback phenomena;
- being electronegative, to reduce the transversal side of the discharge and improve its localization.

These requirements must be fulfilled by eco-friendy mixtures not dangerous for human health and that ensures slow ageing. These conditions are currently met using mixtures of tetrafluoroethane ($C_2H_2F_4$) in combination with sulfur hexafluoride (SF_6), a strongly electronegative gas, and, sometimes, butane (C_4H_{10}). The main component is always $C_2H_2F_4$ ($\gtrsim$90%) with a few percentages in volume of the other components. Enrichment of the mixture with an amount of water vapor is needed to keep conductivity of the plates stable in time.
Because of their exceptional timing performances, RPCs are spreadly used for trigger purposes in the muon systems of HEP experiments, like CMS and ATLAS.

1.4 MPGD

1.4.1 Historical development and evolution

Despite the performance improvements offered by wire systems, the progress with particle physics accelerators and the new quest for rare events, requiring the operation of the detectors at very high particle flux, eventually exceeded the MWPC rate capability, limited by the long collection time of positive ions created in the

avalanche process. A new family of innovative devices, collectively named micro-pattern gaseous detectors (MPGDs), introduced in the late nineties, permitted to overcome some of the weaknesses of wire systems, in particular in their rate limitations [11].

Despite their good performances and large impact on particle physics experimentation, the gaseous detectors making use of thin anode wires as amplifying elements suffer from a number of limitations, such as the maximum length of unsupported wires set by the instabilities due to electrostatic forces, or the mechanical fragility of detectors with thousand of thin wires. An even more fundamental limitation results from the slow retrograde motion of positive ions generated at the anode by the avalanching process, and the long time required to neutralize them at the cathodes. At high radiation fluxes, this accumulation in the gap of positive space charge induces a decrease of the electric field around the wires, with a consequent reduction of gain. For common wire chamber geometry, the gain drop begins at a particle flux around $10^4\,\mathrm{mm}^{-2}\,\mathrm{s}^{-1}$, easily exceeded in experiments [30].
An innovative detector, developed in 1988 by Anton Oed, permitted to overcome some of the above-mentioned limitations [1]. Appropriately named micro-strip gas counter (MSGC), the device, depicted in Figure 1.10A, consists of a set of thin parallel metallic strips engraved on an insulating substrate and alternatively connected as thin anodes and wider cathodes. On application of a difference of potentials between adjacent strips, and with an overlaying gas volume delimited by a drift electrode, the electric field lines converge to the thin anodes creating a field structure evocative of that of MWPCs: electrons released by ionization in the gas volume drift towards the anode and multiply in an avalanche process. As shown in Figure 1.10B, there is a well-defined separation between a drift region, where the primary ionization occurs, and a thinner multiplication region. Using high-resolution, industrially available photolithographic technologies, the distance between strips, or pitch, can be reduced to fractions of a millimeter, thus ensuring a good space resolution of the order of 100 µm [31].

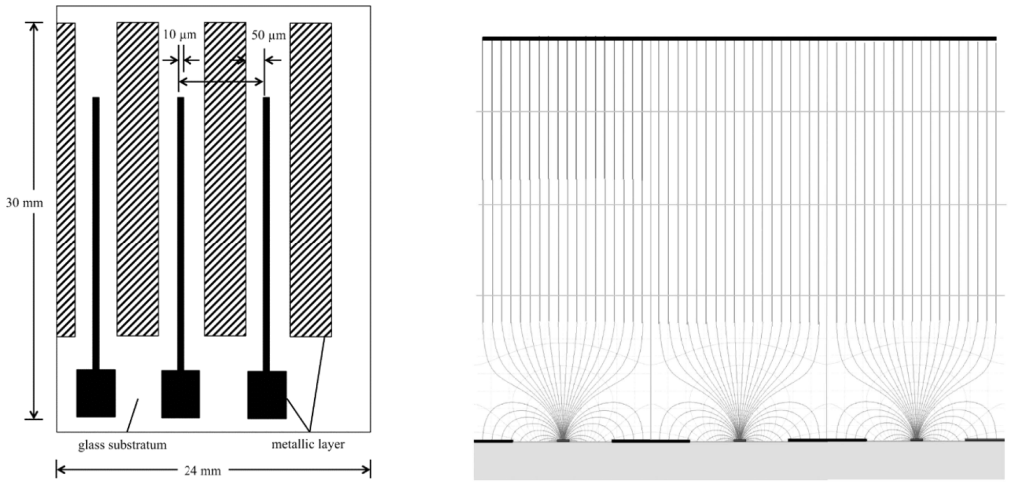

(A) (B)

FIGURE 1.10: (A) MSGC schematics, with thin anodic strips alternating with wider cathodes (from [1]). (B) Electric field lines and equipotentials in the MSGC.

Owing to the short distance between strips, the majority of the positive ions released

in the avalanches are quickly collected and neutralized at the cathodes, minimizing the space-charge-induced field distortions encountered in wire detectors at high radiation fluxes. Adding to the narrow pitch, the fast clearance of the charge results in an increase by almost two orders of magnitude in the rate capability as compared to wire chambers, up to few MHz mm^{-2} [32]. The disadvantage of such a structure is that stable operations are achievable only with low gains, of the order of 10^4, because of the fragile and narrow electrodes employed.

Fostered by the development of micro-strip counters and aiming to improve performances and mitigate long-term reliability problems, numerous innovative detector geometries have been conceived and manufactured with photolithographic or silicon foundry technologies both on rigid and plastic supports. Some of these mitigation techniques are:

- geometries with flat equipotential surfaces in the amplification region, to lower the charge density (MicroMegas);
- cascading multiple amplification stages (GEM);
- embedding resistive materials (MicroMegas, μ-RWELL, resistive GEM).

Due to their effectiveness in facing the new HL-LHC challenges in terms of ultra-high rates, radiation harsh environment, longevity, and large area detectors, MPGD technologies have already started to be integrated into LHC experiments. Triple-GEM detectors have already been installed in TOTEM, LHCb, and CMS; two additional GEM stations will be added to the CMS muon system for the Phase-II upgrade.

1.5 GEM detectors

1.5.1 GEM detectors design

The Gas Electron Multiplier (GEM), introduced by Fabio Sauli in 1997 [11], is a thin polymer foil, metal coated on both sides and pierced with high density of holes, typically 50-100 mm^{-2}, as shown in Figure 1.11A. The GEM foil is the basic component of the single-foil GEM detector, built by inserting the foil between a cathode and a charge collection anode, in such a way that with the application of appropriate potentials, the GEM electrode develops the field lines shown in Figure 1.11B. As evident, the typical three regions of MPGD-based detectors can be distinguished:

- The **drift** region, where the primary electron-ion pairs are generated but no further multiplication occurs because of the low intensity of the electric field;
- The **multiplication** region within the GEM foil holes, where the large difference of potential applied between the two faces of the foil creates a high field in the holes, such that ionizing collisions, with the molecules of the gas filling the structure, can occur. A sizeable fraction of the electrons produced in the avalanche leaves the multiplication region and transfers into the lower gap structure, while ions are recollected by the amplification and drift cathodes, minimizing space charge problems;
- The **induction** region, finally, where the overall charge moves towards the readout anode without further multiplication inducing the readout signal until charge collection occurs.

After the first GEM foil, electrons can also be injected into other multiplying sections before reaching the induction region. This gives great flexibility of use to the detector, exploited to achieve higher gains and better performances. The thin polymer foils can be shaped to match the experimental requirements.

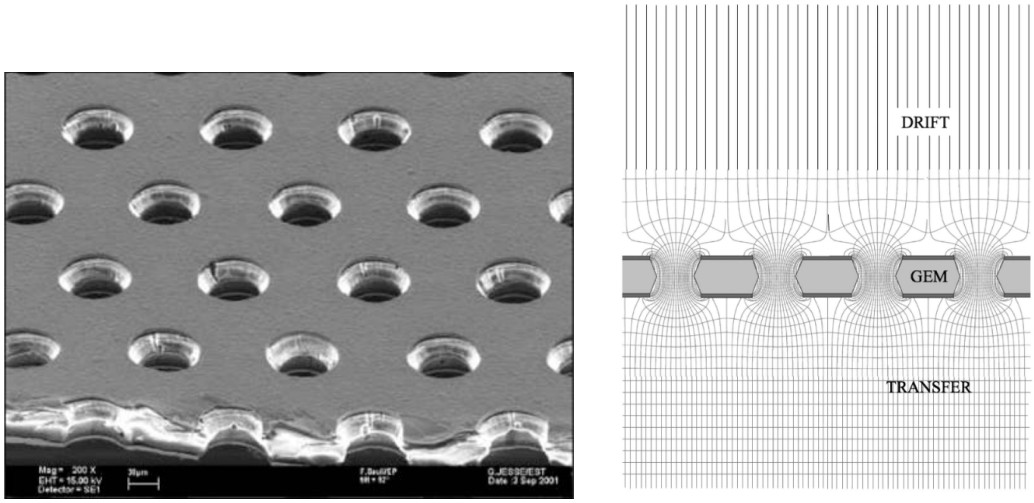

(A) (B)

FIGURE 1.11: (A) Electron microscopic image of a section of a GEM electrode, 50 µm thick. The holes' pitch and diameter are 140, 70 µm (external diameter) and 50 µm (external diameter), respectively; (B) Electric field near a GEM electrode.

1.5.2 Basic GEM operation

Unlike other gaseous counters, the (negative) signal on the GEM anode is induced only by the collection of electrons, without a contribution from the slow positive ions, making the device potentially very fast. Moreover, the moderate field between multiplying and sensing electrodes reduces the probability of the propagation of a discharge to the fragile front-end readout electronics. To perform localization, the anode can be patterned with strips or pads.
The diameter and shape of the holes have a direct influence on the performance and long-term operation stability of a detector. It was found already in early studies [33] that to ensure high gains, the optimum diameter of the holes should be comparable to the foil thickness. Indeed, while narrower holes result in larger fields for a given voltage difference, losses on the walls and charging up compensate for the increased gain. Since a field-dependent fraction of the multiplying electrons is collected on the lower face of the GEM electrode, the effective gain, defined as a ratio of detected to primary charge, is lower than the real gain of the multiplier.
The typical values of the electric-field intensity in a GEM for typical operating conditions are: $\sim$2 kV cm^{-1} in the drift region, $\sim$6 kV cm^{-1} in the induction region and $\sim$50 kV cm^{-1} in between the GEM holes, where avalanche multiplication occurs [34]. Above approximately 8 kV cm^{-1}, avalanche multiplication begins in the induction gap; even if it would be exploitable to attain higher gains, this is not a desirable feature since it might help in propagating a discharge through the structure. An important parameter for a GEM detector is the *transparency*, namely the fraction of ionization electrons transferred through the GEM foil; it depends on the drift field, decreasing at high values due to losses to the top GEM electrode, as seen in Figure 1.12A for a "standard" geometry (70 µm holes at 140 µm pitch) at increasing values of

the GEM voltage; the initial loss at low fields is due to electron capture and diffusion. Transparency losses are important in determining the energy resolution, and directly affect the detection efficiency. The maximum proportional amplification that can be attained before discharge depends on the GEM manufacturing quality since a single local defect can affect the whole electrode. While for small sizes with a thorough selection of the electrodes, an effective gain above 10^3 can be obtained, for larger areas, instead, these conditions are seldom realized and it is preferable to adopt a multi-GEM structure to safely reach larger amplification.

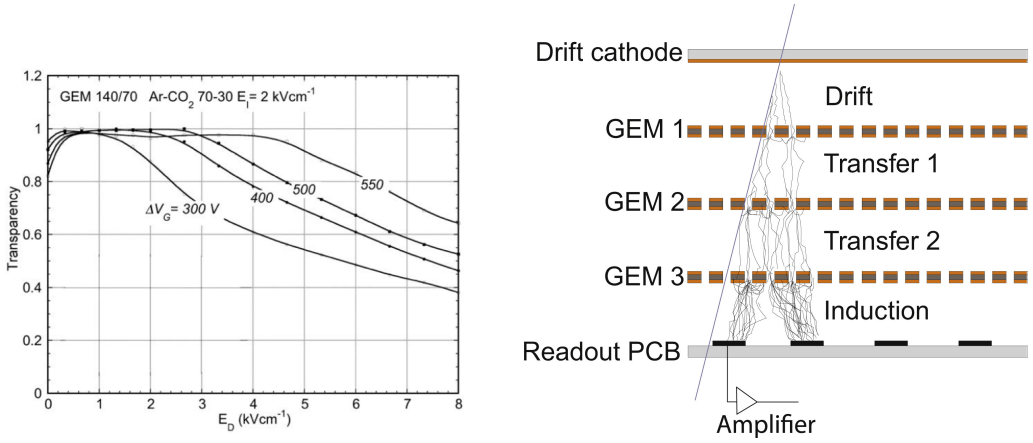

(A) (B)

FIGURE 1.12: (A) Electron transparency of a standard GEM electrode as a function of drift field for fixed induction field and several values of GEM voltage. (B) Schematics of a triple-GEM detector, including an electron avalanche.

1.5.3 Multi-GEM Assemblies

Single-GEM electrodes can reach gains above 10^3 when tested in favourable laboratory conditions. However, when exposed to high rates or harsh beam environment, they tend to discharge at lower values of gain. GEM electrodes can be assembled in cascade, achieving large amplifications at moderate operating voltages for each element; this results in a substantial reduction of the discharge rates for equal gains. While double and triple GEM devices are the most widely used, cascades up to five electrodes have been tested [35, 36]. Figure 1.12B shows schematically a triple-GEM assembly, with three identically mounted GEM foils at short distances, typically 2-3 mm; The resistive high-voltage distribution is the simplest and most widely used, although individual cascaded power supply systems have been developed allowing more flexibility in the choice of the voltage sharing. The dependence of effective gain on voltage is shown in Figure 1.13A for single-, double- and triple-GEM assemblies. For convenience of operation, the voltage applied to each foil is usually identical, but a small unbalance between the foils, with the first GEM operated at higher gain, favors the reduction of the discharge rate. The dashed lines in the figure denote the measured discharge probability on exposure to an external alpha particles source; for a triple-GEM, the onset of the discharge occurs at a gain above 10^4, thus, when working at higher gain, like in CMS GEM (G$\sim 2 \times 10^4$), several strategies are adopted to mitigate the damage caused by discharges, like the introduction of protection resistors [37]. In multiple structures, while the GEM voltages determine the gain of the device, the electric fields in the transfer and induction gaps control the flow, spread and collection of the electron and ions charges. Increasing the field below a

GEM electrode increases the electron current extracted from the foil, but decreases the current injected into the following foil; at each transfer, part of the charge is lost to the electrodes. A thorough optimization of the various field intensities permits to achieve the optimum operating performances in terms of gain, ion backflow reduction and discharge.
In a multi-GEM structure, the various electrodes collect the amplified charges (electrons and ions) resulting from the multiplication and drift processes in field-dependent relative proportions. The anode, final electrode in the structure, only gathers the electrons leaving the last GEM in a cascade; the induced negative signal is therefore very fast, as its width corresponds to the drift of the high-mobility electrons over a few millimeters. For multi-GEM structures, the width of the collected charge increases due to diffusion between the foils, permitting the use of coarser readout strips while ensuring charge sharing.

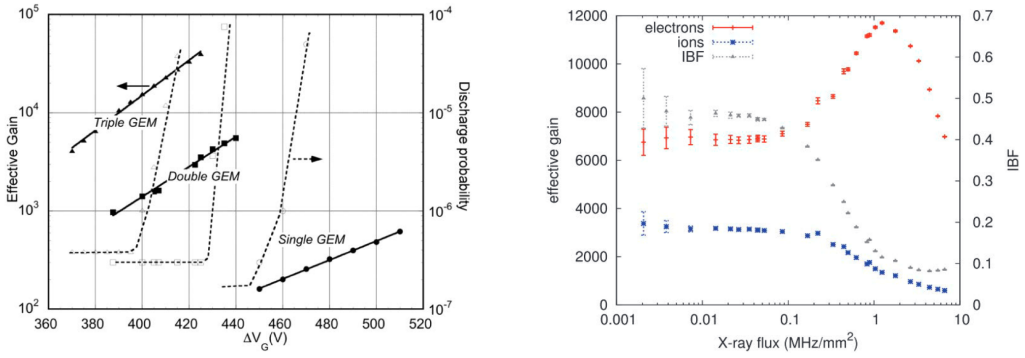

(A) (B)

FIGURE 1.13: (A) Effective gain of a single-, double- and triple-GEM detector measured on soft X-rays. The dashed lines are discharge probabilities on exposure to an internal alpha particle source. (from [38]) (B) Effective electron and ion gains and ions' backflow fraction as a function of X-ray flux measured with a TGEM. (from [39])

1.5.4 Rate Capability and Radiation Resistance

In gaseous counters, the positive ions generated in the avalanche process slowly recede to the negative electrodes until neutralized or collected; the accumulated space charge modifies the electric fields, resulting in a reduction of gain and distortions above a certain value of radiation flux. In multiwire proportional chambers, this limit is attained at around 10^4 particles per second per mm^2. In GEM detectors, the rate capability is improved by several orders of magnitude owing to the fast collection of most ions by the electrodes and to the screening effect from external influence due to the confinement of the avalanches in the holes. The proportional gain, measured on a single GEM exposed to a soft X-ray generator, remains constant up to a flux above 10^6 Hz/mm^2. A systematic study of rate dependence of gain in multi-GEM devices in a range of operating conditions and geometry has shown a tendency of the gain to increase at very high rates, due to space-charge field distortion induced by the positive ions. Simulation studies [40] have succeded in explaining this peculiar behavior as due to the high density of positive ions accumulating near the bottom of the holes. As seen in Figure 1.13B, at very high rates, while the gain increases, the ion current measured on the cathode and the corresponding ion backflow fraction decrease, a behavior well reproduced by simulations.

1.5.5 Discharges and Breakdown

As most gaseous detectors, GEM devices tend to discharge when the voltage is increased over a threshold value, thus limiting the useful range of operation. Depending on the available energy and external resistive protections, the discharge can be bland or evolve in a more disruptive spark breakdown. While discharges are generally observed in the electrode with the highest amount of charge (the last in a cascade), the discharge can propagate to other electrodes, and in particular to the anode for high value of the induction field. Disregarding spontaneous breakdowns due to local defects, two major sources of discharges have been identified: high radiation fluxes and large, albeit rare, energy losses by heavily ionizing particles. In either case, a transition from a proportional avalanche regime to a streamer and then to a spark is observed when the released charge exceeds around 10^7 ions and electrons, i.e. the Raether limit. The discharge can be initiated by any GEM foil in a cascade, and propagate through the structure. For high values of the induction fields, it can continue to the anode. The process of this so-called secondary discharge propagation is crucial due to the danger of exposing the sensitive read-out electronics to irreversible damage.

1.5.6 Ageing

Under sustained irradiation, gaseous detectors can be subjected to the so-called ageing, a permanent damage of the electrodes, resulting in a progressive deterioration of performances. The main cause of ageing is the growth on the electrodes of thin insulating layers resulting from the polymerization in the avalanche process of organic gas molecules or pollutants released by the manufacturing materials. The former typically occurs in gas with H-content, otherwise the latter is dominant, e.g. in Ar:CO_2 mixtures.
GEM structures, not depending on the field strength close to thin electrodes for amplification, are expected to have a reduced sensitivity to the presence of deposits; this has been verified experimentally with long-term irradiation studies. Motivated by the requirement to improve the time resolution, the addition to the gas mixture of carbon tetrafluoride, owing to its well-known etching properties, extends the detector lifetime up to and above a collected charge of $20\,\mathrm{C\,cm^{-2}}$ [41]. The use of CF_4 requires, however, special precautions, due to its reactivity of the fluorine liberated in the avalanches with water to form HF one of the most aggressive acids for many materials [42]. In the development of the forward muon tracker for CMS exposures to various fields of radiation has confirmed the long-term survivability of large GEM prototypes [43].

1.6 Performance of Gaseous Detectors

The performance of a gaseous detector depends on a multitude of factors, from the geometry, as previously mentioned, to the readout electronics. In particular, in this section, the impact of the gas choice will be discussed, together with general features related to spatial resolution and timing resolution.

1.6.1 Impact of the gas choice

The choice of the gas is crucial in determining the performance of the detector, indeed several criteria must be taken into account. In the present section, the impact

of gas choice in proportional counters is discussed. RPC gas choice has been already outlined in Section 1.3.5. As mentioned before, the energy loss by a traversing particle in a gas does not contribute only to the ionization of the medium, because of the non-radiative interactions. To increase the energy loss in the former process, gases with high ionization density are preferred. This feature belongs, in particular, to noble gases argon, krypton and xenon. Also, charge losses must be avoided, thus electronegative gases cannot be considered as main components of a chamber gas. There may be specific cases where exceptions arise, such as in negative ion drift chambers [44].
In order to minimise sparking and leakage currents, which occur in particular near the mounts of the electrodes, the potential differences between electrodes should be as low as possible. A high amplification at a relatively low voltage is provided by the noble gases helium, neon, argon, krypton and xenon, whose thresholds for gas amplification lie at a field strength of about $50\,\mathrm{kV\,cm^{-1}}$. In general, argon gas is the preferred gas for detectors with gas amplification in the proportional regime, because it is the best compromise between costs and ionization density. However, very strong diffusion and an unstable behavior of the gas amplification make it necessary to use argon in admixtures with quenchers.
Unstable behaviors in gas amplification stem from the inability of photons generated during the amplification process to be absorbed, enhancing the avalanche-to-streamer transition. The solution of the problem consists of adding to the noble gas, mostly argon, a quencher. Usually one uses hydrocarbons and CO_2. These molecules have a broad spectrum of rotational and vibrational states which can be excited by the absorption of photons but which release excitation energy preferentially in non-radiative processes. Although hydrocarbons have better properties as quenchers, they can cause polymers to deposit on electrodes, thus altering the detectors' characteristics and reducing their lifetime.

1.6.2 Spatial resolution

The spatial resolution of a detector depends on the segmentation of the readout electrodes: the anode wires in MWPCs and strips along the anode plane in RPCs. In particular, defining the x-axis as the direction perpendicular to the wires (strips), if upon the passage of a particle exactly one wire (strip) with the coordinate x_a fires, then the point of passage must lie within $x_a \pm p/2$, meaning within an interval $\Delta x = p$, the wire spacing (strip pitch). If all passage points near a wire occur with equal frequency (uniform distribution) then the standard deviation, corresponding to the resolution of the measurement device, is given by:

$$\sigma = \frac{\Delta x}{\sqrt{12}}\,. \tag{1.12}$$

Often several wires (strips) respond, in particular, if a track does not pass perpendicular to the detector plane. In order to assign an x coordinate of the crossing point of the track with the anode plane, the center of gravity of the x coordinates of the hit wires (strips) is calculated. Depending on the type of readout (either analog or

digital [1]), its computation and the related uncertainty change. If the readout is digital, the center of gravity coincides with the geometric center of the wires' (strips') cluster, while if the readout is analog, the center of gravity is weighted on the charge induced on the wires (strips) of the cluster.

1.6.3 Time resolution

Time resolution is correlated to two key parameters [45]: the signal-to-noise ratio (S/N) and the slew rate (dV/dt), i.e. how fast the signal rises. Figure 1.14 reports a schematic view of the basic elements used to perform time measurements.

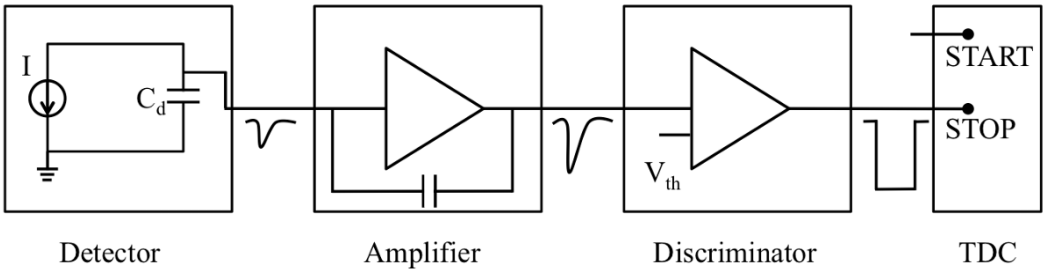

FIGURE 1.14: Schematic view of the basic elements of a time measurement chain.

The detector when traversed by an avalanche-generating particle can be, in general, represented as a current generator (I) in parallel to a capacitance (C_d). The measurement chain typically foresees an amplifier, used as signal shaper, a discriminator, used to compare the signal to a reference level (V_{th}) and to convert it to a logic signal, and a Time to Digital Converter (TDC) to measure time intervals. Taking into account these basic elements the time resolution of the system can be expressed as:

$$\sigma_t^2 = \sigma_{intrinsic}^2 + \sigma_{time\,slewing}^2 + \sigma_{jitter}^2 + \sigma_{TDC}^2 \,, \tag{1.13}$$

where:

- $\sigma_{intrinsic}^2$ is the uncertainty linked to the physics processes characterizing the specific detector.
- $\sigma_{time\,slewing}^2$ is the term related to the time slewing effect caused by the comparison of the signal with a fixed threshold voltage. Even if two signals, with different amplitudes, arrive at the same time, different shapes of the rising edge can cause the two signals to be detected at two different times. The time slewing effect can be reduced both by increasing the slew rate and reducing the threshold, if the noise allows to do so.
- σ_{jitter}^2 stems for the fluctuation of the time of crossing threshold caused by the intrinsic noise.
- σ_{TDC}^2 corresponds to the uncertainty introduced by the time digitization performed by the TDC. Assuming, in the simplest of cases, that such a device is a counter of internal clock cycles of period Δt, the time delay between a start

[1] In the analog readout the induced signal is read as it is, so its shape can be used to infer more precisely the position of the traversing particle; in the digital readout a logic 1 is returned if the signal exceeds a certain threshold.

event and a stop event is given by an integer n representing the number of clock cycles between the two events. The time resolution associated with TDC is $\sigma_t = \Delta t/\sqrt{12}$, and its contribution is typically small, indeed for a $\Delta t = 25$ ps it is of 7 ps.

Let us briefly outline the typical values of the intrinsic time resolution for the most employed gaseous detectors.
For MWPCs, the intrinsic time resolution is mainly determined by readout signal formation. In fact, because of the varying distances of the tracks from the anode wire and because of the statistical distribution of the electron drift times, the signal times lie typically in an interval of 100 ns after the particle has passed the layer. The time stamp estimated above could be shortened forming a logical OR of signals from neighboring layers and using as a time stamp the time of the earliest hit, thus reaching resolutions around 10 ns [8].
In RPCs, the amplitude of a signal depends on the distance of the ionization from the anode, as the electric field is homogeneous. Hence, intrinsic time resolution is dominated by the fluctuations in time occurring when a signal crosses the threshold value. For trigger RPC a typical time resolution of ∼1 ns is reached. In order to further improve the time resolution of RPCs, so-called multi-gap RPCs have been proposed with multiple avalanches inducing signals on the same readout strip [46]. The time resolution improves with the number of gaps decreasing under 100 ps
Regarding GEMs, the time performance of a GEM-based detector for a MIP is correlated with the statistics of the position of formation of the primary clusters in the drift gap [47, 48]. The general expression for the space-distribution of the cluster j created at a distance x from the first GEM foil, is [10]:

$$A_j^{\bar{n}}(x) = \frac{x^{j-1}}{(j-1)!}\bar{n}^j e^{-\bar{n}x} \tag{1.14}$$

where $\bar{n}$ is the average number of clusters created per unit length. For a given drift velocity in the drift gap, v_d, since the statistics of ionization follows a poissonian distribution, the probability-distribution of the arrival times on the first GEM for the cluster j gives:

$$P_j(t_d) = A_j^{\bar{n}}(v_d t_d)\ . \tag{1.15}$$

Specifically for the cluster produced closest to the first GEM, that is the one created closest to it, ($j = 1$):

$$P_1(t_d) = \bar{n}\cdot e^{-\bar{n}v_d t_d} \ \Rightarrow\ \sigma_1(t_d) = \frac{1}{\bar{n}\cdot v_d}\ . \tag{1.16}$$

The latter gives the intrinsic value of the time resolution of the detector if the first cluster is detected and returns a time stamp (i.e. exceeds the discriminator threshold). A high primary ionization ($\bar{n}$) and a fast (v_d) gas mixture should be chosen in order to improve the time performance of a GEM detector. For an Ar:CO_2(70:30) gas mixture ($\bar{n} = 100\,\mathrm{cm}^{-1}$) in a 3 kV cm^{-1} electric field (v_d = 1-2 cm µs^{-1}), and, the intrinsic time resolution is approximately $\sigma_{\mathrm{GEM}} \sim$ 5-10 ns.

Chapter 2

The CMS experiment

GEM detectors play a central role in the upgrades foreseen for the CMS experiment in the new high-luminosity environment characterizing the upcoming HL-LHC project. Due to their outstanding rate capability and long lifetime, three stations of GEM detectors (GE1/1, GE2/1, and ME0) will be added to the CMS muon system, in order to maintain its current trigger performances and increase its pseudorapidity coverage. ME0 station will be installed in a currently instrumented region closest to the interaction point; The high rate of background particles foreseen in such a region - unprecedented in the CMS muon system - makes it a particularly challenging station and in need of a specific R&D process.
The present chapter firstly outlines the current design and characteristics of the CMS experiment, and the main modifications it will undergo according to the Phase-2 upgrade plan. Then, a more detailed description of the muon system upgrades is provided, highlighting the motivations under the choice of introducing the three new GEM stations.

2.1 General design and characteristics

The CMS detector [49] is schematically depicted in Figure 2.1. It has a cylindrical shape with total dimensions of 21.6 m in length and 15 m in diameter. Its weight amounts to about 12500 tons. Due to the high symmetry of the collision topology, this particular shape grants to cover the largest variety of trajectory directions of the generated particles.
The entire structure is divided into three main blocks: the central barrel and two endcaps. Each part of CMS is composed of several layers of detectors with specific roles in measuring the particle properties. The inner part of the solenoid contains the silicon tracker system for measuring the trajectories of charged particles (starting point, direction and momentum) and for identifying vertices. At a larger radius, still inside the solenoid, the electromagnetic calorimeter identifies and measures the energy of electrons and photons, while hadrons and jet properties are measured in the hadronic calorimeter. The muons, finally, are identified and their track is sampled with gaseous detectors placed outside the solenoid and sandwiched in the magnetic flux return yoke.

2.1.1 The Silicon Tracker

The silicon tracker has a total length of 5.8 m and a diameter of 2.5 m, covering the pseudorapidity range of $|\eta| < 2.5$. A high granularity is required to reduce occupancy and improve spatial resolution to cope with high particle fluxes during collisions. In the barrel, four layers of pixel detectors are employed close to the beam pipe, followed by silicon strips arranged in four inner and six outer layers. In the

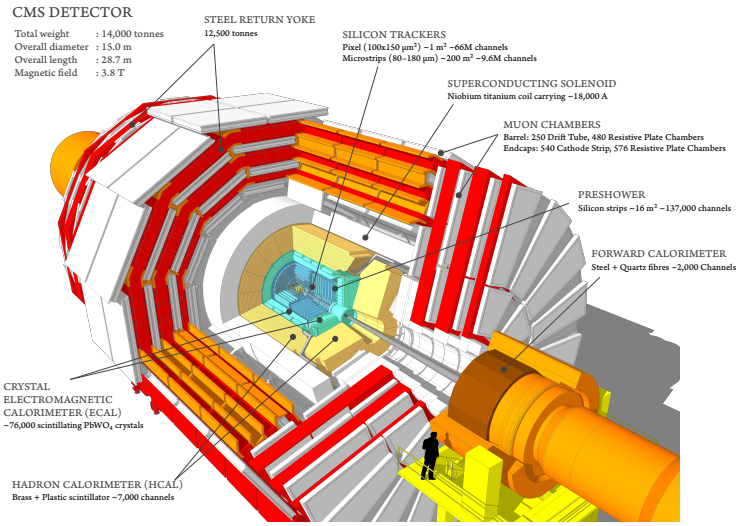

FIGURE 2.1: Schematics of the CMS detectors.[50]

endcaps, two layers of pixels and three inner and nine outer layers of strips are used to track the decay vertices and the paths of the particles generated in the interactions. Overall, the system comprises 65 million channels for the pixels and 10 million channels for the strips. For low energy or low transverse momentum hadrons ($1\,\text{GeV} < p_T < 10\,\text{GeV}$) the reconctruction efficiency is around 85%. For higher energies ($p_T > 10\,\text{GeV}$), it becomes 95%. For electrons the efficiency is estimated to be around 90%, and 98% for muons. In the region $|\eta| < 1.6$, the precision on the muon transverse momentum measurement is $\sigma(\delta p_T / p_T) < 2\%$ up to $p_T = 100\,\text{GeV}$.

2.1.2 Electromagnetic Calorimeter

The electromagnetic calorimeter (ECAL) is designed to perform energy measurements for electrons and photons with precision up to 1% and, working in a team with the hadronic calorimeter, also for hadronic jets. It utilizes inorganic crystals made of $PbWO_4$. This material has been selected because of its small Molière radius, its short radiation length, its radiation hardness and the very short scintillation-decay time. To collect and read the scintillation light produced, avalanche photodiodes are used for the barrel crystals, while vacuum photo-triodes are employed in the endcaps.

2.1.3 Hadronic Calorimeter

The hadron calorimeter (HCAL) is used to determine the energy of the hadronic jets and to estimate the missing transverse energy in the events. A sampling calorimeter, composed of alternating layers of brass absorber and active plastic scintillator, has been chosen. The hadron calorimeter covers the pseudorapidity region $|\eta| < 3.2$; in addition, the forward hadron calorimeter extends the angular acceptance up to $|\eta| < 5.2$.

2.1.4 The solenoid magnet

The CMS superconducting magnet has a length of 12.9 m, an inner diameter of 5.9 m, and a magnetic field of up to 4 T in the inner part and residual 2 T in the returning iron yoke. In normal operations, the magnetic field is about 3.8 T. This provides

the bending of particle trajectories in the transverse plane, obtaining less than 5% of charge misidentification for muons with $p_T < 200\,\text{GeV}$, $\sigma(\delta p_T/p_T) \approx 1\%$ for $p_T = 100\,\text{GeV}$ and less than 10% for $p_T < 1\,\text{TeV}$ for combined inner tracker and muon system measurements.

2.1.5 The Muon System

The particles that can traverse the entire ECAL and HCAL without being stopped, such as muons with $p_T > 3\,\text{GeV}$, are measured in the outermost group of subdetectors of the CMS experiment: the *muon system*. It is constituted by four stations in the barrel and four disks in both endcaps, covering the range $|\eta| < 2.4$. In Figure 2.2, the muon system is shown.

The CMS muon system is a robust and redundant muon spectrometer that can

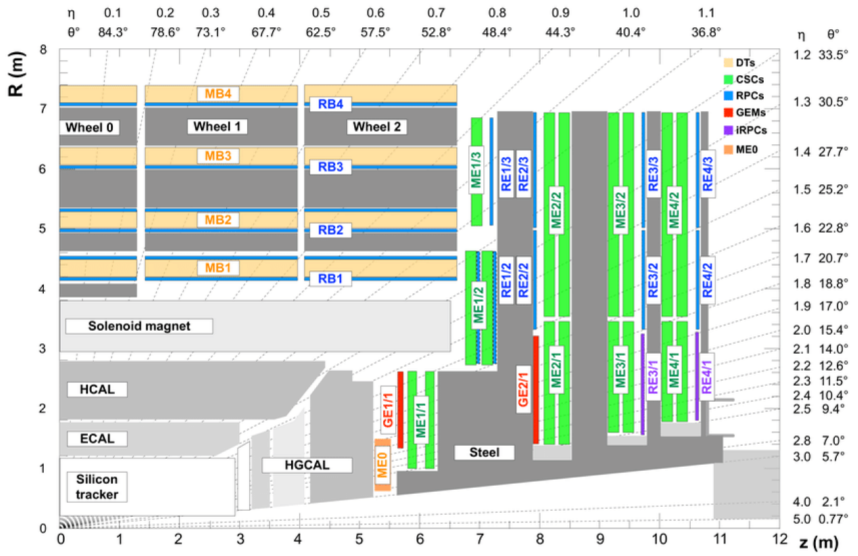

FIGURE 2.2: Transverse section of one quadrant of the CMS detector showing the present muon system and the proposed locations for the triple GEM detectors. (Source: [51])

provide precise identification and high-resolution p_T measurements thanks to four different types of gaseous detectors. Drift Tube Chambers (DTs) are employed in the barrel region ($|\eta| < 1.2$) where the occupancy is low and there is a very low residual magnetic field in between the yoke iron. Cathode Strip Chambers (CSCs), faster and more radiation resistant, have been chosen for the two endcaps ($0.8 < |\eta| < 2.4$) to cope with higher particle fluxes and non-uniformities in the magnetic field. Both DTs and CSCs have a spatial resolution of around 100 µm. Resistive Plate Chambers (RPCs) complement DTs and CSCs in both regions up to $|\eta| < 2.1$, in particular, thanks to their excellent time resolution (their spatial resolution is of a few cm), they identify muons from collision events with a precision of a few ns. In the range $1.5 < |\eta| < 2.8$, Gas Electron Multiplier (GEM) detectors are planned to be installed to complement CSCs and RPCs in triggering and tracking, for redundancy purposes.
The inner tracker precision is the most relevant for muons with $p_T < 200\,\text{GeV}$. This is due to the multiple scattering that muons experience when traversing the calorimeters, the coil, and the iron yoke. For muons with higher transverse momenta, the full system resolution takes advantage of the inclusion of the system, improving tracker resolution.

2.1.6 Trigger and DAQ

The CMS Trigger and Data Acquisition System (TriDAS) [52] plays an essential role because both the collision and the overall data rates are much higher than the rate at which one can write data to mass storage. At LHC, the proton beams will cross each other at a frequency of 40 MHz. At the Run-1 design luminosity of $10^{34}\,\mathrm{cm}^{-2}\,\mathrm{s}^{-1}$ each crossing results in an average of $\sim$ 20 inelastic pp events producing approximately 1 MB of zero-suppressed data. CMS TriDAS is split into two steps, Level-1 Trigger and High Level Trigger, to reduce the data rate by a factor 10^9 to a maximum of 100 Hz and 100 MB s^{-1}.
The required time for any primary decision to discard data from a particular beam crossing is of 3.2 µs (128×25 ns), set by the constraints imposed by the physical size of the CMS detector and underground caverns and by the electronic technology employed. During this 3.2 µs period, the Level-1 Trigger system (or "L1T") performs a primary selection of data. It is hardware-based and collects data with coarse granularity from the front-end, then it develops and propagates decisions made via custom electronics to the readout electronics front-end buffers; This first step is designed to reduce the rate of events accepted for further processing to less than 100 kHz. The High-Level Trigger (or "HLT") works at a software level and is designed to reduce this maximum Level-1 accept rate of 100 kHz to a final output rate of 100 Hz.

2.2 CMS Phase-2 upgrade

The HL-LHC - scheduled to start in 2029 - will allow precision studies of electroweak symmetry breaking and new physics via quantum loops. Higgs boson couplings will be measured to a few percent precision; rare Higgs decays (such as $\mathrm{H} \rightarrow \mathrm{c\bar{c}}$), di-Higgs production and longitudinal vector boson scattering will become more accessible. For this to happen with 14 TeV collision energy, a 10-fold increase of integrated luminosity to 3000 fb^{-1} until the early 2040s is required [53]. It translates into a luminosity of 300-400 fb^{-1} per year. HL-LHC will, then, deliver an instantaneous luminosity of 5-7.5 $\times\, 10^{34}\,\mathrm{cm}^{-2}\,\mathrm{s}^{-1}$. These conditions correspond to a number of simultaneous collisions (pileup) per bunch crossing (BX) of 140-200. This increase in pileup collisions per BX makes data collection in HL-LHC physics program a challenging task. Therefore CMS will undergo a massive upgrade, namely the Phase-2 upgrade, that foresees a redesign of both the trigger architecture and the detection apparatus.

Firstly, the hardware-implemented Level-1 Trigger [54] will go through three major innovations:

- **Track Trigger path**: track primitives are produced in the tracker back-end from the information of the outer tracker only; these are, then, used by the Global Track Trigger (GTT) to reconstruct vertex and track-only objects and associate muon and calorimeter deposit matching. This path is crucial in identifying PU contribution and reducing the L1T.
- **Particle Flow Trigger path** (or Correlator Trigger): it receives information from Calorimeter, Track and Muon Trigger paths and exploits it to implement a PF-like processing.
- **Scouting system**: it guarantees the ability to perform trigger-less analysis of L1T data profitting from spare optical links.

This new L1T architecture comes with an increased latency of 12.5 µs, corresponding to roughly three times the Phase-1 latency. The increase is due to the Track Trigger path hardware reconstruction and matching time. The output bandwidth is of 750 kHz, being 7.5 times larger than the Phase-1 output rate.
Concerning the detector systems, several changes are scheduled in the Phase-2 upgrade project, due to the limitations of existing detectors in the increased luminosity environment.

In the tracking system, both the strip trackers and the pixel detectors (already substituted once in Phase-1) will have to be replaced due to the significant damage and performance degradation they would suffer from during operation at the HL-LHC, and to cope with more demanding operational conditions. The requirements are extensively outlined in reference [55]. Closest to the beam pipe, the Inner Tracker (IT) will be made of 2 billion hybrid micropixels of 25 µm $\times$ 100 µm. The newly designed Outer Tracker (OT) consists of 43 million microstrips and 170 million macropixels. The OT will provide input at 40 MHz to the L1T.

In the calorimeter system, the major upgrade is in the endcaps, where the High Granularity Calorimeter (HGCal) [56] will be installed, replacing the existing calorimeter system. It will be the first imaging calorimeter at a high-PU hadron calorimeter, designed to provide precision particle flow reconstruction improving the sensitivity for vector boson fusion and scattering and allowing more precise reconstruction of jet substructures, as well as, through its timing capability, to extend the reach for long-lived particle searches. The system employs a mixed technology: 6 million Si sensor channels in the region closer to the interaction point, and 250 000 scintillator tiles read out by SiPMs in the lower fluence hadronic region. Absorbers of Pb, Cu, and Cu-W are used in the EM section, while in the hadronic section steel is used. With the installation of this new calorimeter, space will be freed behind it for additional instrumentation, introducing the possibility to add a new - closest to the interaction point - muon station, ME0.
Finally, in the next section, the CMS Phase-2 upgrade of the Muon System will be presented.

2.3 CMS Phase-2 upgrade of the Muon System

The muon detectors play a central role in CMS, thanks to the muon's low cross-section of interaction with the matter. In fact, muons can be identified and measured individually and accurately, as they stand out from the large hadronic background typical of hadron colliders, mostly stopped by the calorimeters. In addition, the most sensitive signatures of the production of new particles often include one or more muons.
Among the different parts of the CMS muon system, the forward region is particularly challenging for muon detection: on one hand, relatively light particles to be studied or searched for are produced predominantly with high pseudorapidities; on the other hand, backgrounds are the highest. HL-LHC project makes such region even more challenging. Therefore, to maintain the present excellent performance of the CMS muon system within large geometrical acceptance, several measures must be undertaken.
Under the foreseen luminosities at the HL-LHC, the event pileup (PU) will rise substantially to become a major challenge for the experiments. At the nominal

luminosity of the HL-LHC, the average number of interactions in a single crossing is approximately 140 [5], compared to the average Run-3 LHC pile-up of 50 (@ $2 \times 10^{34}\,\mathrm{cm}^{-2}\,\mathrm{s}^{-1}$) [57]. This higher pile-up yields an increase of the rate of secondary particles. Such a high rate is a major challenge for particle detectors. As it was not foreseen in the planning phase of the LHC in the 1990s, now detectors and electronics must be upgraded to handle this rate, using the latest technology. In addition, new requirements on the Level-1 trigger and the data acquisition in terms of latency can only be met with new electronics with deeper buffering and faster processing.
Moreover, even if the aging of high-tech components over the long lifetime of the CMS detector of about 30 years (2008-2038) was already taken care of in the LHC planning phase, the longevity is further compromised by the increased particle flux. A higher rate of interacting particles enhances radiation damage to detectors as well as electronics, shortening life expectancy even more. Since all present gaseous detectors and a large fraction of their electronics are expected to stay also for HL-LHC, their longevity must be validated. Aging electronics parts need to be replaced by new components, if possible exploiting technology advancements.
As a consequence of the increased luminosity, in Phase-2 the background induced by neutrons and low energy gammas, and the large number of particles crossing the CMS detector quasi simultaneously, will be very high. This makes the association of individual hits to tracks - and thus the event reconstruction - a major challenge, both for the muon trigger and the offline analysis. It can be met only if the number of hits recorded for a single particle is sufficiently large, and if both the spatial and the time resolution are very good.
Regarding the trigger, the standalone muon trigger capabilities are important for reconstructing long-lived BSM particles decaying into muons outside the inner tracker. In these scenarios, neither a vertex constraint nor the trigger information from the tracker can be exploited. Standalone muon triggering requires good measurement of the track bending to determine the momentum, which is possible only with several independent direction measurements, for which the additional muon chambers in the endcap regions are essential.
Moreover, the extended coverage of the Phase-2 inner tracker in the very forward region reach-es $|\eta| = 4$, well beyond the current muon detector acceptance of $|\eta| < 2.4$. The enlarged η range of the new tracker needs to be matched by a muon detector, since the silicon tracker alone cannot identify muons. The increase in acceptance is particularly rewarding for multi-lepton final states, for example, Higgs boson decay to four muons.
Finally, another challenge to be addressed in the muon upgrade is the set of new environmental restrictions on the use of fluorine-based gases. In order to comply with these constraints, the release of greenhouse gases into the atmosphere should be substantially reduced. Ideally, the gas mixtures of some CMS muon detectors are supposed to be adapted, but this is still not required for the very next runs, because a difference in the gas mixtures implies a difference in the HV working point, and such power supplies have not been developed yet.

2.3.1 Upgrade of the electronics of existing muon detectors

The existing DT, CSC, and RPC detectors are all essential for identifying and measuring muons at the required precision and accuracy needed to fulfill the CMS physics program. Therefore, their electronics need to be upgraded to fit with the new latency and it must be guaranteed that their performance will be sustained at high luminosity.

Drift Tube chambers

According to HL-LHC predictions, the maximum hit rates in the DT chambers will be about 50 Hz cm^{-1} [6], and measurements performed in test beams, with spare detectors, show that the DT chambers can handle the hit rate expected. Only in the MB1 stations in the outer wheels and in the MB4 detectors, a significant drop of the hit efficiency is predicted, due to the decrease of the gas gain caused by deposits, forming on the anode wires. The large number of hits measured for each muon track ensures that even a 50% per-layer loss in DT efficiency translates into a small reduction in track reconstruction efficiency. Moreover, the DT front-end electronics and high voltage boards are sufficiently radiation-hard and do not need to be replaced. Nevertheless, upgrades are needed for the Minicrate electronics (MiC), which are attached to each chamber and host readout and trigger electronics. The current version (MiC1) needs to be replaced for HL-LHC operation by improved Minicrates, because of the limited maximum Level-1 trigger rate, below the Phase-2 CMS requirements, and the insufficient radiation hardness of some electronics components. Accordingly, the Phase-2 upgrade foresees a reduction of the Minicrate functionality, with the displacement of the trigger and event-building logic to the back-end electronics, in the CMS underground control room. As a consequence, the new Minicrate (MiC2) will be able to cope with the Phase-2 conditions in terms of latency, readout rate, and trigger rules.

Cathode Strip Chambers

The Cathode Strip Chambers (CSCs) cover the CMS endcap regions corresponding to $0.9 < |\eta| < 2.4$, and, as a result, the radiation dose they are subjected to is significantly larger than for the muon chambers located in the barrel, with a predicted maximum hit rate of 4.5 kHz cm^{-1}. Longevity tests have shown no significant deterioration of key chamber parameters such as gain, detection efficiency and spurious signal rates. Nevertheless, EU regulations of greenhouse gases will severely restrict, or even ban, the use of CF_4, which has a critical role in the longevity of CSCs. Accordingly, tests with ecologically-friendly substitutes are ongoing. While the CSC modules are expected to provide satisfactory performance throughout the HL-LHC program, some CSC read-out electronic boards will need to be replaced in order to handle the new longer latency. The new electronics will consume more power which will require the redesign of the LV system with higher maximum currents and appropriate voltage levels. Higher background rates and the need for a more accurate monitoring of CSC currents will also imply an incremental upgrade for the present HV system.

Resistive Plate Chambers

For the RPC system, two upgrades are foreseen: a new link system for the current RPC chambers and two new RPC stations (RE3/1 and RE4/1) to be added. Regarding the current RPC system, the RPC chambers can operate until the end of Phase-2, but the link system, which connects the front-end board to the trigger processors, must be exchanged. The maximum estimated background rate for the ultimate HL-LHC luminosity is approximately 200 Hz cm^{-2} for the present RPC chambers [6]. In such an environment, it has been proved, via dedicated test beam measurement, that RPC performance remains good and the chambers do not need to be replaced. RPC electronics board including front-end electronics are evaluated to be radiation hard and can stay for the Phase-2 running. The data from the RPC front-end boards

are sent to trigger and readout via a link system. The current link system is made of electronic boards using obsolete IC components, most of them not available anymore in the market. These boards have also weak electronics components that can be disturbed by electromagnetic noise and that are not certified for the full HL-LHC lifecycle. The upgrade of the link system will make the RPC system robust against such effects. In addition, the upgraded system will exploit fully the intrinsic time resolution of the RPC chambers, which is of the order of 1.5 ns. The present link system records the hit time in steps of 25 ns, synchronized with the LHC bunch crossings. This limitation can only be removed by exchanging the existing link system by an upgraded one. An improvement of the RPC time resolution by more than one order of magnitude allows to enhance background hit rejection, to trigger on slow heavy stable charged particles, and to facilitate the RPC system synchronization.

2.3.2 New detectors for the Phase 2 upgrade of the muon system

A major challenge at the HL-LHC is the reliable triggering on muons in the very forward regions, which suffer from high muon and background rates and reduced magnetic bending. The number of hits measured per track must be increased to enhance the redundancy of the muon system and to obtain a robust track reconstruction, including rejection of wrongly reconstructed tracks, already at the Level-1 trigger. The existing muon stations ME1/1 and ME2/1, where the bending angles are largest and thus momentum determination is most effective, will be equipped with GEM detectors denoted GE1/1 and GE2/1. In the third and fourth muon stations, improved RPC (iRPC) detectors, RE3/1 and RE4/1, will provide the needed redundancy at relatively modest cost. The ME0 chambers, also using GEM technology, will extend the acceptance of the muon system further to $|\eta| = 2.8$, by providing hits for triggering and for offline muon reconstruction.

*i*RPC detectors: RE3/1 and RE4/1

The muon RPC upgrade extends the geometrical acceptance of the RPCs from $|\eta|$=1.9 to 2.4 with two additional stations RE3/1 and RE4/1, that will complement the CSC stations ME3/1 and ME4/1 enhancing the local muon measurements providing more track hits and a larger lever arm. Such an improvement, together with a better time resolution, increases the accuracy of the p_T assignment when RPC and CSC data are combined. Hence, the Level-1 muon trigger rate is able to suppress low-p_T tracks, whose mismeasurement could cause a saturation of the trigger rate. The expected maximum rate is 700 Hz cm^{-2} and it needs an upgrade of the current RPCs employed, i.e. the so-called *improved* RPCs (*i*RPC). The *i*RPCs are designed to reach a higher rate capability and are characterized by slower aging.

GEM detectors

The increasing luminosity causes an increasing rate of incident particles in the most forward region of the CMS endcaps. These rates approach the capabilities of the traditional gaseous detector, like CSC and RPC detectors, so novel technologies should be employed to instrument this challenging region of the apparatus. The introduction of micro-pattern gaseous detectors (MPGD) has provided new opportunities for developing cost-effective muon detectors capable of efficiently detect muons in high-rate environments. The CMS plan for the Phase 2 upgrade of the muon system includes the installation of three new stations instrumented with GEM detectors.

These three stations are GE1/1, GE2/1 respectively in the first and second sector of the endcap, and ME0, in a region of the first endcap sector that is currently instrumented with the HCAL but that will be freed with the installation of the new HGCal. Figure 2.2 shows the exact location of the mentioned GEM stations; GE1/1 and GE2/1 systems will cover the forward pseudorapidity range $1.6 < |\eta| < 2.4$ and are aimed at improving forward muon triggering capabilities. The ME0 detector is not only the closest muon station to the interaction point, but also the first one to cover the pseudorapidity range $2.4 < |\eta| < 2.8$. Hence, ME0 aims to take advantage of the extension of the CMS inner tracking capabilities in order to extend efficient muon identification (and triggering) capabilities up to $|\eta| \sim 2.8$.

2.3.3 Maintaining existing trigger capabilities

HL-LHC luminosities will degrade the trigger capabilities of the muon system as it is, so the Phase-2 upgrades come with the challenge of maintaining an efficient and reliable triggering. With no upgrades, the muon trigger rates would increase significantly, particularly in the region $|\eta| > 1.6$. The Level-1 muon trigger bases its selection upon the observed bending of muon trajectories in the magnetic field. In the forward part of the detector, at high $|\eta|$ the magnetic field decreases increasing the distance from the interaction point, resulting in a decreased bending of muon trajectories throughout the endcaps and, consequently, a decreased p_T resolution. Additionally, many more soft particles will scatter off elastically in the muon system, and, in particular, in the iron yokes. Multiple scattering causes the straightening of the tracks, making low p_T muons misinterpreted as high p_T muons by the CSC track finder [58].
Therefore, the consequent degradation of transverse momentum resolution in the forward region leads to a high trigger rate, due to the increased probability of low transverse momentum particles being reconstructed as high transverse momentum muons. This effect is enhanced by the HL-LHC increasing rate.
Novel strategies to maintain the existing trigger capabilities have been found. It has been proved that an efficient low-rate muon trigger can be designed by combining Level 1 tracking trigger (L1Trk) with Level 1 standalone muon trigger (L1Mu). In particular, the strategy consists of three steps [59]:

1. find standalone muons, built from stubs in the muon detectors. This step ensures strong discrimination against non-muon background;

2. match L1 tracks to standalone muons, using the more precise momentum measurement of the tracker. Being the major innovation of the Level-1 Trigger system, the good transverse momentum measurement of the tracking trigger eliminates mismeasurements that drive the high trigger rate;

3. isolate muons using L1 tracks.

However, this cannot be the only trigger path, because many new-physics scenarios involve muons that are significantly displaced from the beamline, produced in the decay of long-lived particles and, in those cases, tracks from the track trigger cannot be reconstructed for muon having an impact parameter, $|d_{xy}|$, beyond 1 cm. Standalone muons however can be reconstructed up to a transverse displacement with respect to the beampipe, L_{xy}, of $\sim$350 cm and up to an impact parameter of $\sim$100 cm. The strategy consists of requiring precision measurements of the muon direction in at least two stations to measure momentum, using the DT stubs direction

measurements in the barrel and the measurement of the bending angle from GE1/1-ME1/1 (or ME0-ME1/1) and GE2/1-ME2/1. Additionally, a veto of the tracks from the track-trigger extrapolated to the second muon station is employed to reduce the trigger rate.
The standalone L1Mu trigger also provides an important complementarity as it can reconstruct muons with transverse momenta below the L1Trk cut-off threshold of $\sim$ 2 GeV [59], which is especially important for the scenarios of new physics involving forward production where momentum is much higher than the transverse momentum, e.g. $\tau \rightarrow 3\mu$. It is therefore planned that the Phase-2 muon trigger design will utilize both L1Trk and L1Mu capabilities in designing specific trigger paths to maximize the CMS physics reach.
Among the additional three aforementioned GEM stations, GE1/1 and GE2/1 are aimed at improving the direction measurement when combined with, respectively, the classical ME1/1 and ME2/1 stations, thanks to their good position resolution and to the increased lever arm formed by the two couples of detectors. The measurement of the candidates' direction in station 1 using the new GE1/1 and existing CSC ME1/1 chambers provide an accurate measurement of the muon bending angle that is almost not affected by multiple scattering, as illustrated in Figure 2.3A, resulting in a clear separation between soft muons ($\sim$5 GeV) and hard muons ($\lesssim$20 GeV) outlined in Figure 2.3B. This discriminates lower p_T muons and reduces the soft muon rate at the level-1 trigger, as it is illustrated in Figure 2.4A.

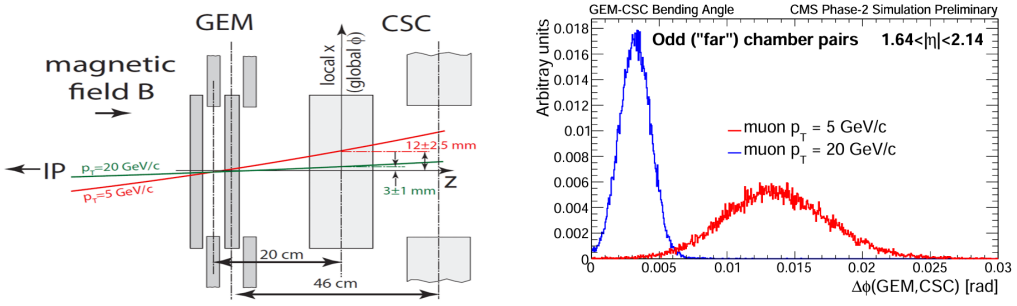

(A) (B)

FIGURE 2.3: (A) GEM and CSC systems in each station enlarge the lever arm for a bending angle measurement unaffected by multiple scattering. (Source [60]) (B) GEM-CSC bending angles for soft (5 GeV/c) and hard (20 GeV/c) muons for odd-numbered GEM chambers. (Source [58])

Figure 2.4B shows the measurements that can be performed in the Phase-2 upgrade CMS muon system. In particular, the new GEM station provides direction measurements within stations, improving Level-1 trigger p_T measurements. In particular, the second overall station (GE2/1+ME2/1) serves redundancy purposes. The availability of a second measurement of the muon direction further improves the efficiency and increases the resilience and stability of the trigger in practical operations, enhancing its robustness.

The third station, ME0, among its multiple functions (discussed in Section 2.3.4), is also designed to make the muon trigger match the track trigger coverage, $|\eta| < 2.4$. Indeed, as the new GE1/1 detector can only extend to $\eta \sim 2.15$, the region $2.1 < |\eta| < 2.4$ of the current detector coverage is left out. The new ME0 detector, positioned behind the new endcap calorimeter consists of six layers of triple-GEM

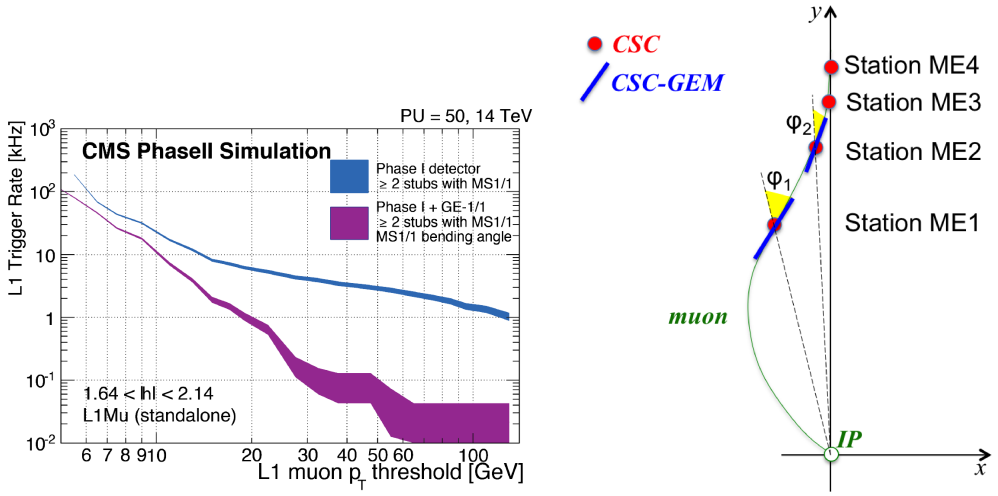

(A) (B)

FIGURE 2.4: (A) Trigger rate reduction with the deployment of muon direction measurement using GEM GE1/1 and CSC ME1/1 chambers. (Source [51]) (B) Schematic of the muon system measurements provided by the Phase-2 upgrade CMS muon system. In particular, the new GEM stations introduce the direction measurements within stations. (Source [6])

modules capable of high-precision direction measurement and effectively serves as the fifth station in this challenging region.

The availability of direction measurements in two stations allows the development of new algorithms for trigger reconstruction and momentum measurements of muon candidate directions, with the compatibility checking between the two directions reconstructed. The two direction measurements are provided by ME1/1-GE1/1 and ME2/1-GE2/1 pairs in the region $1.6 < |\eta| < 2.1$ and by ME0-ME1/1 and ME2/1-GE2/1 pairs in the region $2.1 < |\eta| < 2.4$. The requirement that displaced muon candidates are to be incompatible with any of the L1 tracking trigger candidates allows a further large reduction in the trigger rate. Figure 2.5 shows the efficiency and the trigger rate for a displaced muon trigger. The rate reduction due to the track trigger veto ranges from a factor 3 to 8 depending on the working point and the muon candidate $|\eta|$.

2.3.4 The ME0 station: muon identification and triggering in the very forward region

The baseline design of the ME0 detector station comprises 36 module stacks (18 per endcap), each composed of six layers of triple-GEM chambers covering $\Delta\phi = 20°$, divided into 384 radial strips, and $\Delta\eta = 0.8$, divided into eight partitions. Figure 2.6 illustrates the insertion of the ME0 stacks into the endcap. The modules in each stack are oriented upside-down with respect to the modules in the two adjacent stacks to allow for overlap of modules and maximum coverage.
Its deployment will reinforce muon trigger in $2.0 < |\eta| < 2.4$ (as discussed in Section 2.3.3) and extend current muon coverage into the region $2.4 < |\eta| < 2.8$, thereby reducing the non-instrumented area behind HGCAL. The primary challenge of designing ME0 is efficiently identifying muons with a transverse momentum much lower than their momentum while maintaining a low rate of background

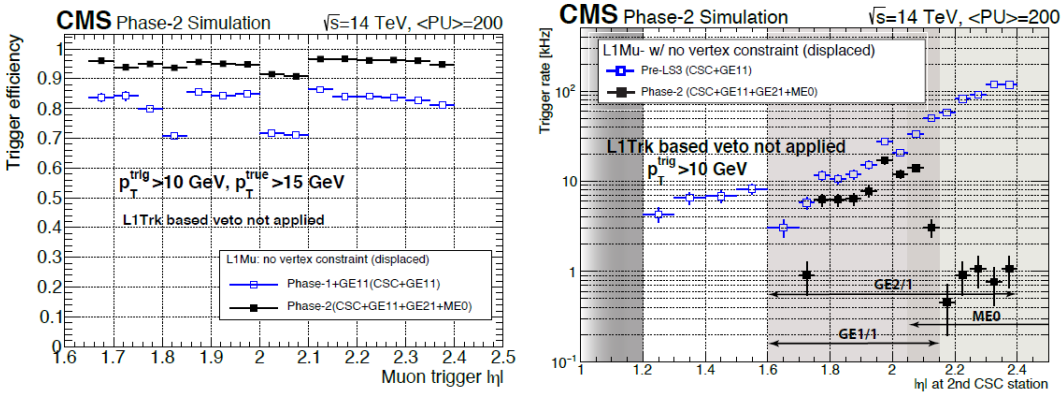

FIGURE 2.5: Efficiency (left) and trigger rate (right) for the displaced muon candidates. The rates do not include the effect of the L1Trk veto, which, depending on the working point, provides a factor of 3-8 reduction in the trigger rate at the cost of a 3-10% loss in efficiency. (source [6])

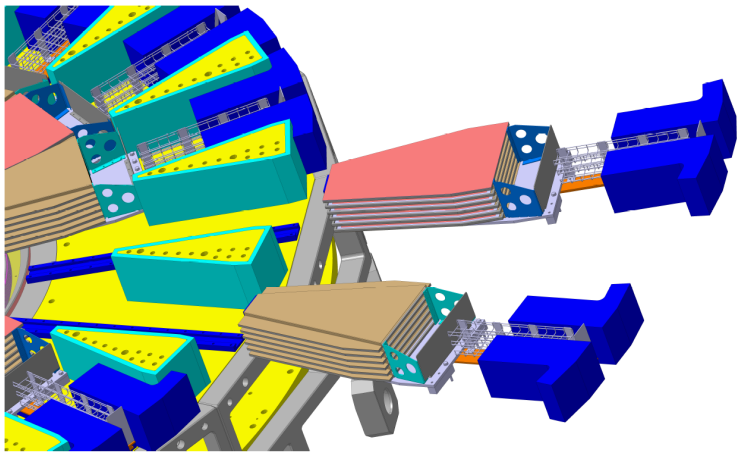

FIGURE 2.6: 3D drawing of the insertion of two adjacent stacks of six ME0 modules (pink/brown) into the endcap nose. The rails for sliding the stacks into the endcap are visible both on the nose (blue) and on the stack (orange). Note the alternating orientation of modules in the stacks. (source [6])

mis-identified as muons in the harsh HL-LHC conditions. A key feature of the ME0 design is multi-layer detection of charged particle trajectories with excellent ϕ resolution. This allows for the combination of a high precision ϕ trajectory measurement with a less precise η position measurement into a coarse estimate of particle transverse momentum. The quantity $\Delta\phi$ - defined as the fitted ϕ position of a ME0 segment at the first detector layer subtracted from its fitted ϕ position at the last layer - is a powerful variable for identifying segments as likely originating from high transverse momentum particles. The current benchmark for optimizing ME0 reconstruction is identifying muons with transverse momentum greater than 3 GeV ($p \gtrsim 15$ GeV) at an efficiency of 95%. As the detector is effective in measuring momentum, it is capable of reconstructing segments with lower transverse momentum, which is important for certain physics signatures, such as the lepton flavor violation decay $\tau \to 3\mu$.
In this environment there are two distinct sources of background misidentified as muons:

1. **charged particles produced in PU interactions**

Baseline ME0 performance is evaluated at 200 PU interactions per BX, resulting in $\sim$ 1000 pixel tracks ($p_T > 0.5\,\text{GeV}$) per BX in ME0 acceptance. This large pixel track density can potentially lead to the reconstruction of misidentified muon candidates arising from the high combinatorics of background pixel tracks and ME0 segments. The granularity of the ME0 design allows for the association of pixel tracks to the correct ME0 segment by matching in η position, ϕ position, particle transverse momentum, and particle charge.
The matching of $\Delta\phi$ is limited by multiple scattering for muons with transverse momentum lower than 20 GeV while the precision in the segment η position is similar to that of the pixel measurement for low transverse momentum muons. Even if ME0 is shielded and placed behind HGCAL, the PU particle density is so large that approximately $\sim$ 12 real muons (dominated by decay-in-flight muons from pile-up interactions) and $\sim$ 50 electrons or hadrons (which either escape HGCAL or are produced through interactions in front of ME0) produce hits in the ME0 detector (including both endcaps) every BX. These low transverse momentum particles are a potentially large source of background segments.
The left plot in Figure 2.7 shows that the segments produced by these particles can be reduced by 30% by requiring that segments contain hits in at least four layers. The right plot shows that they can be further reduced by a factor of $\sim$ 10 by requiring that they have a $\Delta\phi$ consistent with $p_T > 3\,\text{GeV}$ particles ($|\Delta\phi| < 0.013$).

2. **long-lived neutrons and their byproducts**
These particles are estimated to induce $\sim$ 1000 ME0 hits per BX, which due to the large combinatorics can be a potentially large source of background ME0 segments. At the nominal luminosity of $7.5 \times 10^{34}\,\text{cm}^{-2}\,\text{s}^{-1}$, this background is reduced to a negligible level by requiring that segments contain hits in at least four layers.
Because ME0 is designed to consist of six layers, requiring four layers results in a sub-percent loss of muon segment reconstruction efficiency. However, neutron-induced background estimation has many sources of uncertainty and is sensitive to small changes in beampipe and calorimeter design. Therefore if the neutron-induced hit rate is higher than expected, this layer requirement can be increased to five layers for a percent level efficiency loss in order to maintain a negligible neutron induced segment level.

Figure 2.8 shows the simulated background at the ME0 station, outlining that a rate up to $200\,\text{kHz}\,\text{cm}^{-2}$ is expected to be reached. The inclusion of ME0 will also extend the range of muon triggering to the $2.4 < |\eta| < 2.8$ region. The average number of background segments per event (for all ME0) is shown in the left plot of Figure 2.9. This background multiplicity is too high for using ME0 to increase the single muon trigger coverage. However, the segment position and transverse momentum measurements can be used in conjuction with other L1-trigger objects in multi-object triggers. For example, triggers targeting multi-muon signatures, such as $\tau \to 3\mu$, can include the additional requirement of a ME0 segment in a ϕ slice of one endcap for a factor of $\sim$ 10 rate reduction. The second category of identification is offline reconstruction, in which pixel tracks are matched to ME0 segments, also in the HLT. The matching of track position, charge and transverse momentum to ME0 segments allows for a background reduction by an order of magnitude. This is shown in the

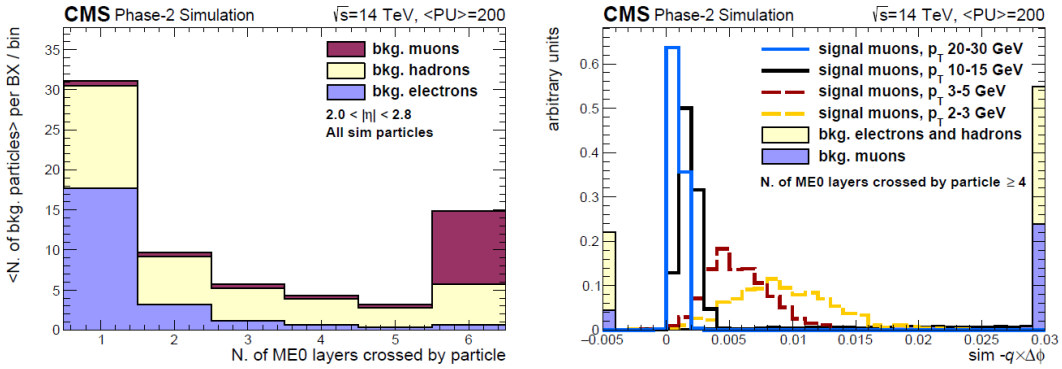

FIGURE 2.7: Properties of both generated muon and PU particle trajectories in ME0. They are obtained from the simulated hits on the ME0 detector layers and include the effect of multiple scattering. Left: The distribution of the number of ME0 layers crossed by each PU particle, normalized by the total number of generated events. The colors of the stacked histograms denote the type of particle. The category labeled "muons" is primarily comprised of particles originating from light hadron decay. The other categories include particles that escape HGCAL and those that are produced through interactions in front of ME0. Right: The $\Delta\phi$ distribution for generated muons and PU particles for those particles that cross at least four ME0 layers. The distributions for the PU particles are shown in the stacked histograms, in which the colors denote the particle type. The distributions for generated muons are shown in the non-stacked histograms, for which different colors refer to different muon p_T. (Source [6])

right plot of Figure 2.9, in which the number of pixel tracks matched to ME0 segments is displayed as a function of pixel track $|\eta|$.

ME0 capabilities allow building an effective trigger path extending from Level-1 into the HLT, in which Level-1 selections are followed by the early stages of HLT, where ME0 candidates are first reconstructed at full granularity (L1 uses twice lower granularity), which are used to seed fast local tracking reconstruction in the forward pixel detector, muon-pixel track matching and near-offline selections already at the early stages of the HLT. The high resolution of the upgraded endcap calorimeter system is expected to allow an additional improvement of the offline muon identification and rejection of non-muon backgrounds based on the amount of energy associated with a candidate using the high granularity calorimetry information.

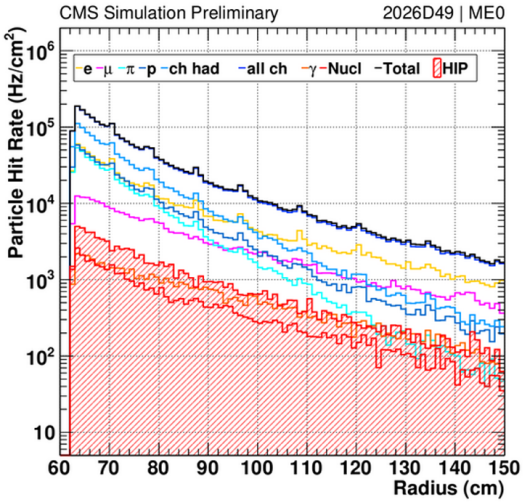

FIGURE 2.8: Expected background flux in the ME0 environment as a function of the distance from the LHC beam line. (Source [61])

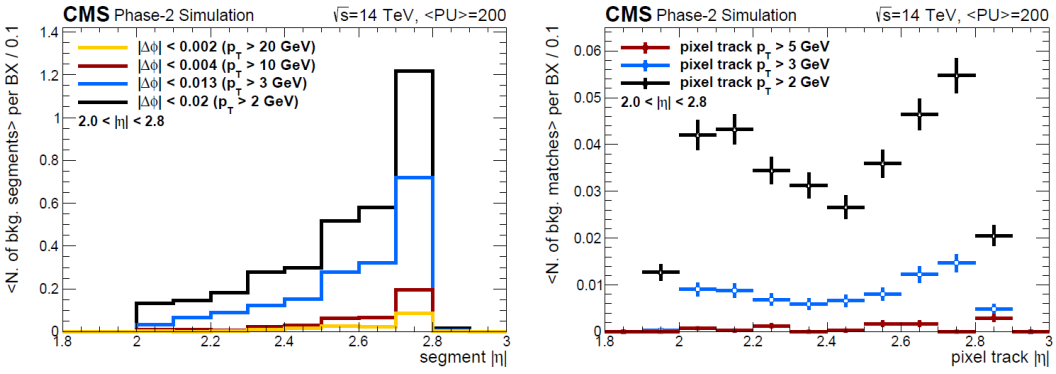

FIGURE 2.9: Average number of reconstructed ME0 objects per event as a function of $|\eta|$ in events with neutron background simulation and 200 PU interactions per BX. The averages are of all objects reconstructed in both endcaps. Left: The average number of reconstructed ME0 segments per event. The colors indicate the multiplicity after different Df selections. Right: The average number of pixel tracks matched to ME0 segments per event. The colors indicate the multiplicity for different pixel track transverse momentum ranges.

Chapter 3

The CMS GEM ME0

The present chapter focuses on describing the design of the triple-GEM modules designed for the ME0 detector, together with the requirements that need to be fulfilled in order to comply with its functionality inside the CMS muon system. Then, an overview of the ME0 readout chain will be provided, describing the front-end electronics, the back-end electronics, and the data acquisition system. Finally, the main calibration and configuration scans for the above-mentioned systems will be outlined.

3.1 CMS triple-GEM detectors for ME0 station

3.1.1 GEM module design

Each detector in the ME0 system is a large trapezoidal triple-GEM detector [62]. The detector itself consists of a trapezoidal gas volume containing a stack of three identical large area trapezoidal shaped GEM-foils embedded between a drift electrode and a readout board. The dimensions of the different regions in the CMS triple-GEM detectors are: drift region of 3 mm between drift cathode and the first GEM, spaces of 1 mm and 2 mm in the electron transfer gaps between GEM foils, and a 1 mm space in the signal induction region. The baseline gas mixture for operating the CMS triple-GEM detector is Ar:CO_2 (70:30).
Figure 3.1 shows the exploded view of the mechanical design of a CMS ME0 triple-GEM detector prototype.

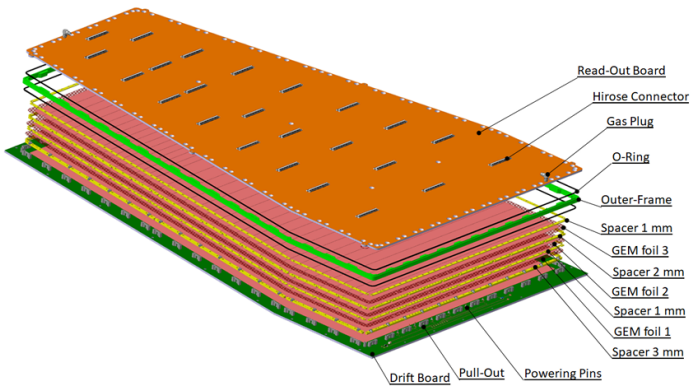

FIGURE 3.1: Exploded view of the mechanical design of a CMS ME0 triple-GEM detector prototype showing the schematic flow of the assembly procedure. (Source [62])

The trapezoidal GEM foil surfaces oriented towards the readout board are a single contiguous conductor whereas the GEM foil surfaces oriented towards the drift board are segmented into numerous HV sectors. The HV segmentation has undergone modifications during ME0 prototype studies.
In particular, the first design was characterized by a transverse segmentation, i.e. sectors were meant to run across the width of the trapezoid as shown in Figure 3.3A. The width of the sectors was designed to be gradually narrower when going from the short end of the trapezoid to the wide in such a way to make each segment cover the same area of about 100 cm^2. As required, this segmentation design restricts the amount of charge that can flow from one foil during a discharge to about 2 µC and, consequently, limits the total energy of a discharge to less than 0.5 mJ[6]. Additionally, protection resistors of 2 MΩ (for GEM top foils), 100 kΩ (for GEM bottom foils) and 10 MΩ (for the drift electrode) separate each HV segment from the HV supply cable, as shown in Figure 3.2.

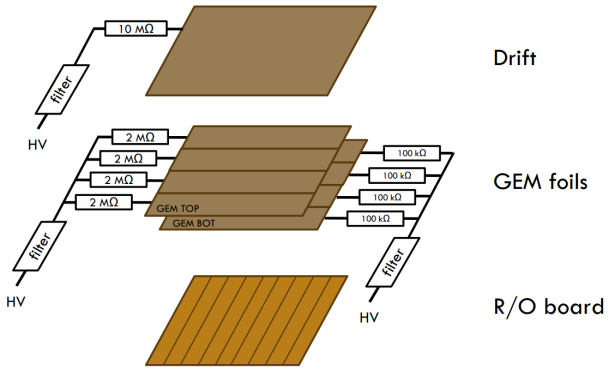

FIGURE 3.2: Schematic of the resistive circuit in the ME0 design, focusing on the single-segmented GEM foil facing the readout plane. (from [63])

This protects the GEM foil against destruction due to discharges, which are inevitable even if they occur at low rates under standard operating conditions. In the worst case, if a destructive discharge were to occur in an HV sector (creating a short circuit between top and bottom electrodes of a GEM foil), it would disable only that one HV sector permanently instead of rendering the entire chamber unusable. Nevertheless, studies of the irradiation of large-area tiple-GEM detectors [64] show that transversal segmentation is not the best design solution, since it causes a drop as high as 40% of the nominal gas detector gain, which would result in severe loss of tracking efficiency.
Indeed, when the detector is irradiated, the charges produced in the avalanche and moving in the gas induce currents on the electrodes that flow through the protection circuits, resulting in a voltage drop on the electrode itself. The voltage drop is a global effect over the entire foil, i.e. it increases for wider irradiated areas. A voltage drop implies a gain drop, and to recover the original nominal gain ($\sim 2 \times 10^4$) voltage compensation is needed. The voltage is increased in order to compensate for the drop caused by the high rate of particles passing through the detector. The procedure for the compensation is described in Appendix C. Nevertheless, with a transversal segmentation, the highest η region would require a nominal gain of approximately 6×10^4 after compensation, thus increasing damage risk in case of sudden beam loss during LHC operation. Moreover, each GEM foil sector would have

to be powered at a different voltage point to account for the highly uneven background rate at increasing pseudorapidity.
The solution for these two issues is represented by the azimuthal HV segmentation, depicted in Figure 3.3B.

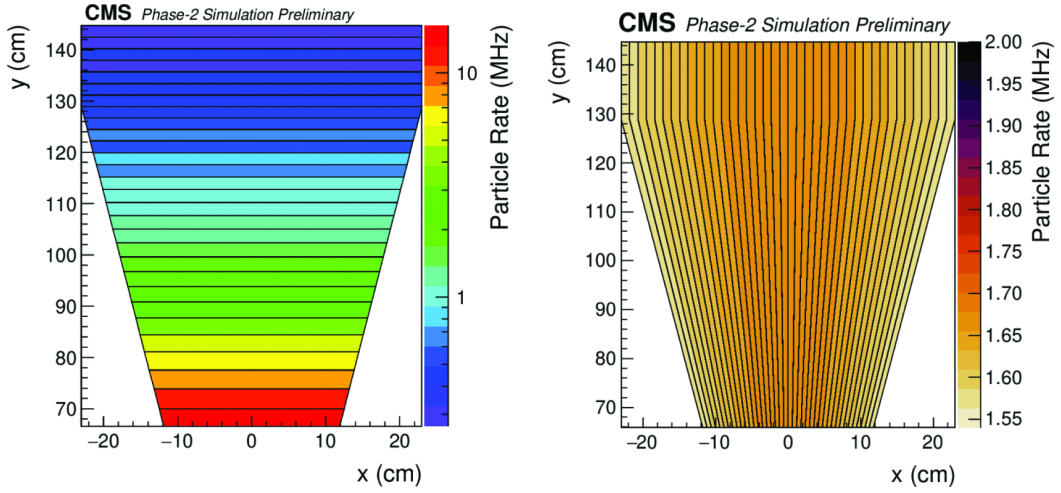

(A) (B)

FIGURE 3.3: (A) Scheme of a ME0 detector with transverse GEM foil segmentation with respect to the LHC beam line, showing the expected background particle rate per sector. (Source [61]) (B) Design of the adopted azimuthal segmentation for the ME0 detectors, showing the expected background particle rate per sector in the CMS environment. (Source [61])

This design choice manages both to equalize the gain drop across different GEM foil sectors and to minimize the average gain drop. In a segmentation with 40 sectors, the average rate per HV sector in the CMS background can be contained to 1.5 MHz, while the effective gain drop can be minimized to about 10% of the expected value of 2×10^4. A drawback of this alternative design involves the dead area introduced by the polyimide separation lines between two adjacent foil sectors. Considering that each separation line has an average thickness of 100 µm, the total dead area of a ME0 module with 40-sector azimuthal segmentation is approximately 4% of the detector surface, compared with about 0.1% for a 29-sector longitudinally segmented detector.

3.1.2 Performance requirements

The desired tracking and physics performances of the ME0 detector, outlined in Sections 2.3.3 and 2.3.4, impose the following basic requirements, listed in reference [6], on the detection performances of the CMS triple-GEM detectors:

- Maximum geometric acceptance;
- Single-chamber efficiency of 97% or better for detecting minimum ionizing particles;
- Rate capability of at least 150 kHz cm^{-2} for a ME0 module.
- Angular resolution of 500 µrad or better;
- Timing resolution of 8 −10 ns for a single chamber;

- Gain uniformity of 15% or better across a module and between modules;
- No gain loss due to aging effects after 7.9 C cm^{-2} for a ME0 module;
- A discharge rate that does not impede performance or operation.

A brief review of the rationale for these requirements is provided. Maximum acceptance will yield maximum physics yield. With 97% individual module efficiency, a ME0 stack with six modules will have a 98.8% efficiency for providing at least five hits for stub reconstruction based on combinatorics. The maximum expected hit rate within the ME0 acceptance is about 150 kHz cm^{-2} for HL-LHC [65]. A hit precision of 500 µrad will give sufficiently precise stub directions for stub matching to tracker tracks and CSC stubs. As the GEM detectors will provide primitives to the trigger, a time resolution of 8 −10 ns is required for a single chamber when running with 25 ns bunch crossing time at the HL-LHC in order to match the correct bunch crossing. A uniform module response will ensure that there are no geometrical reconstruction biases. The gain of a single GEM foil typically varies across the foil surface by 5-8% due to intrinsic variations in hole diameters that stem from the production process. The corresponding typical gain variation in triple-GEM detector is $\sqrt{3}$ times larger, i.e. about 10-15% [66]. The modules should not incur significant additional response non-uniformities due to any other factors. The charge expected to be integrated in the ME0 sector at the highest η over 10 years of operation at the HL-LHC is about 7.9 C cm^{-2} [67].
In addition, several specific technical constraints and requirements need to be taken into account in the module design. As a baseline, it must be possible to operate the modules using only counting gases that have low global warming impact while fulfilling the above performance requirements. Sufficiently small readout segmentation in η, i.e. along the readout strips, is needed so that the rate of multiple hits on the same strip that can lead to ghost stubs is well controlled. Finally, the modules must be designed so that chambers and stacks will easily fit into their designated locations in the muon endcap.

3.2 Design of the ME0 readout chain

A GEM detector in CMS (GE1/1, GE2/1, ME0) is typically divided into three parts:

- The **Detector** itself: it converts the particle energy deposit into a small analog electric signal;
- The **Readout electronics**: it amplifies and digitizes GEM signals and sends them to trigger and data acquistion;
- The **Services**: they enable detector and electronics powering and communication (HV, LV, fibers, etc.)

Furthermore, the GEM readout architecture can be divided into:

- The **Front-end** electronics: it is on-detector and reads analog GEM signals and sends digital output to trigger and data acquisition. The building blocks of the front-end electronics are: the readout chip, namely the VFAT3, discussed in Section 3.3.1, the optohybrid board described in Section 3.3.2, and the GEM electronic board explained in Section 3.3.3;

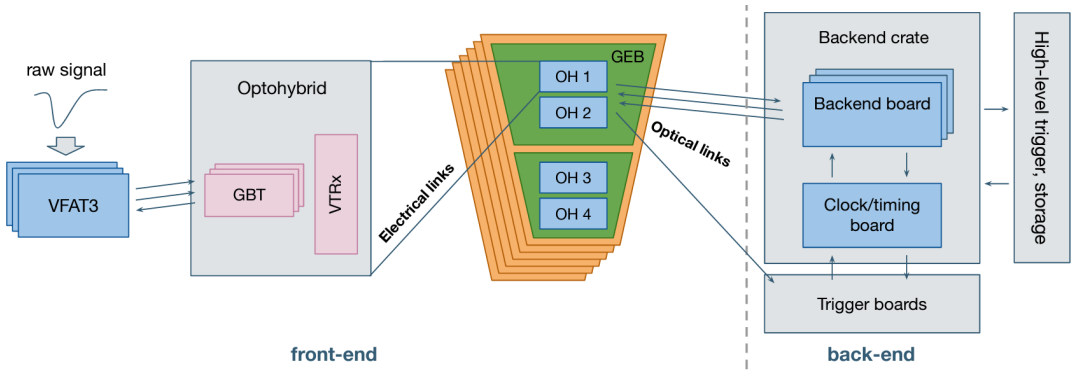

FIGURE 3.4: Overall block scheme of the ME0 readout architecture. Front-end and back-end sub-systems are distinguished. Courtesy of A. Pellecchia

- The **Back-end** electronics: it is off-detector, in the counting room, and receives front-end data and sends them for trigger or storage.

Figure 3.4 shows the overall block scheme of the ME0 readout architecture.
A constant exchange of information occurs between GEM electronics (front-end + back-end) and the CMS DAQ system. Here, the steps of the communication procedure for ME0 are briefly discussed.
First, digital information obtained from the OR of two neighboring strips (half granularity data) is sent from the front-end electronics to the backend, where stubs, namely ME0 trigger primitives, are reconstructed. ME0 stubs are, then, sent every BX to the Level-1 Trigger system[1]. L1 trigger selects the most interesting BXs to be recorded and sends back a Level-1-Accept (L1A). GEM back-end sends the L1A to the front-end, which returns the full granularity data for the selected BXs. The GEM back-end sends the data to the central CMS DAQ. Then, events are reconstructed and further filtered at the High-Level Trigger (HLT), and, finally, the remaining data are stored.

3.3 The front-end electronics

3.3.1 The readout chip: VFAT3

The VFAT3 is a front-end ASIC [2] to read out, discriminate, and, eventually, send data to trigger and data acquisition system [68]. Each VFAT3 chip provides 128 channels, each containing an analog part, a discriminator, and a block that handles digital information and communicates with the back-end electronics. The overall block scheme is depicted is Figure 3.5. Therefore, one of these chips can read out up to 128 detector strips.

The analog part is optimized for the readout of gaseous detectors and each channel contains internal input protection to protect from discharge spikes.
Figure 3.6 shows a block diagram of the analog front-end system of one of the 128 VFAT3 channels.

[1] In GE1/1 and GE2/1 the trigger primitives are the half granularity data.
[2] Application Specific Integrated Circuit (ASIC) is an integrated circuit customized for a particular use.

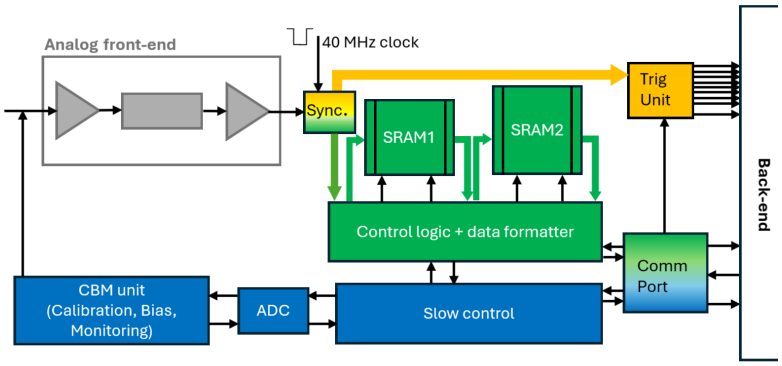

FIGURE 3.5: VFAT3 block diagram. The yellow path represents the fixed latency path, and the green one is the variable latency path. The blue blocks represent units dedicated to control, calibration, bias and monitoring.

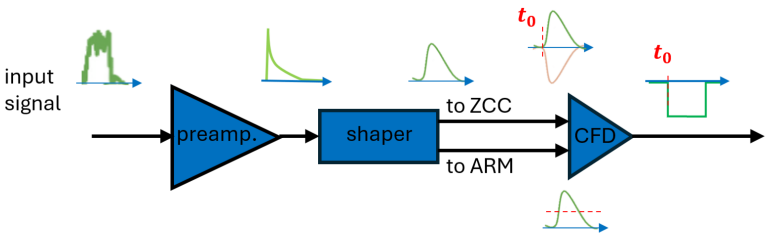

FIGURE 3.6: VFAT3 analog front-end block diagram.

The parameters of the analog channel front-end are optimized for the expected shape of a triple-GEM signal (as simulated in Figure 3.7).Each channel is provided with:

- a charge-sensitive preamplifier (CSP), that integrates the current signal over a time window and generates a voltage signal that is proportional to the incoming input charge, by means of a feedback capacitor. A feedback resistor is connected in parallel to the capacitor in order to have a well-shaped tail pulse. The VFAT3 CSP sensitivity can be varied between 8 and 60 mV fC^{-1}, by adjusting the feedback resistor and capacitance;
- a shaper, whose load capacitance is adjustable to allow front-end peaking times programmable between 25 and 100 ns.

Signal charge from GEM detectors can last approximately 60 ns, or so, depending on the gas mixture and the drift gap. The shaping time of the front-end can be adjusted to fully integrate this charge and hence maximize signal-to-noise ratio.

In between the analog front-end and the digital block, each channel is provided with a constant fraction discriminator (CFD). The constant fraction discrimination is a technique that provides information about the arrival time of an event, in a way that is amplitude-independent and, consequently, more accurate than a traditional leading-edge discriminator [3]. Figure 3.8A shows the two methods applied to two signals with a different amplitude, highlighting that the CFD optimizes timing by compensating for the time walk due to the fluctuations in the signal amplitude.

[3]The digital signal is returned when the analog signal exceeds the threshold set.

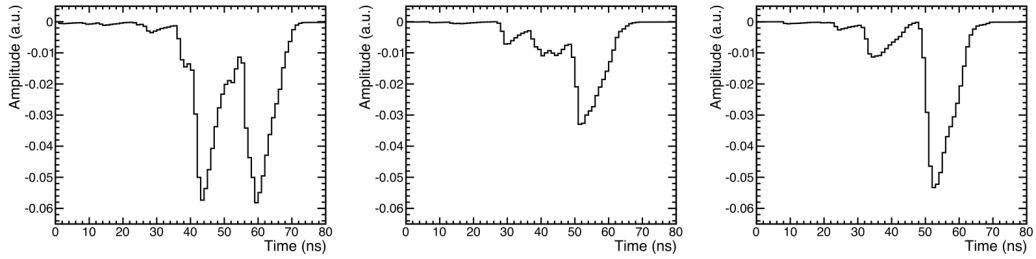

FIGURE 3.7: Examples of simulated signals from a triple-GEM detector. (from [69])

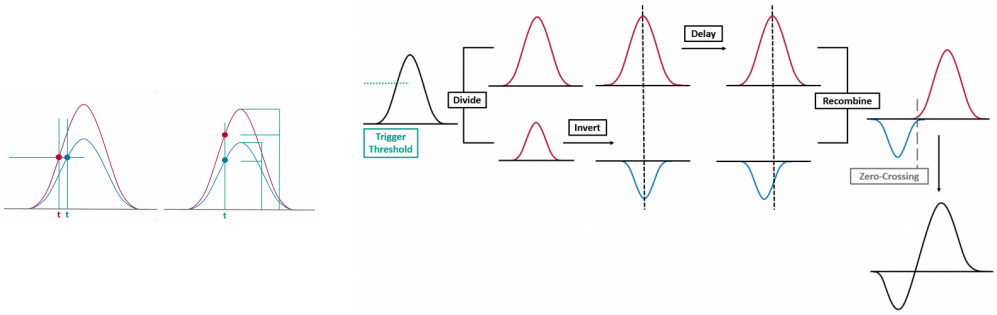

(A) (B)

FIGURE 3.8: (A) Leading edge discrimination (left) where timing jitter is equal to the difference between the two readings of time, t. Constant fraction discrimination (right) where the time is taken at the same proportional height of the two incoming pulses. (from [70])(B) Process of constant fraction discrimination where the incoming pulse is divided into 2/3 and 1/3, the lower portion inverted, the higher portion delayed, and the signals recombined. The zero-crossing point where the two portions of the signal combine is now independent of signal amplitude. (from [70])

This technique is articulated in the following steps:

1. the analog signal is shaped by a passive network of RC filters to a bipolar signal. The latter is obtained by subtracting a fraction of the input unipolar signal from its delayed copy, as schematically shown in Figure 3.8B;

2. a small voltage offset, namely the ZCC threshold, is added to the bipolar signal to avoid firing the zero-crossing comparator on noise. ZCC threshold is set via an 8-bit DAC, with a nominal sensitivity of 0.5 mV bit^{-1};

3. when the bipolar signal first crosses the programmable ZCC threshold, the offset is removed;

4. when the bipolar signal crosses the zero level, the output of the CFD is enabled.

The arrival time of the ZCC output signal is independent of the input signal amplitude.
The input signals are sent in parallel to an arming circuitry, in order to enable CFD output only when the input signal is larger than the programmed threshold provided by a global 8 bit digital-to-analog-converter (DAC). The nominal sensitivity of ARM DAC is of 2 mV bit^{-1}. Since both the ZCC and ARM threshold are set globally

for the entire chip, each channel is provided with its own DAC to compensate for mismatches among single channels, and make the response of the chip as uniform as possible. The DAC is composed of 6-bit DAC for the amplitude, corresponding to 0.5 mV bit^{-1}, plus one bit for the polarity.

Following the discriminator there is a synchronization unit that synchronizes the comparator result with the LHC clock, i.e. a 40 MHz clock. The data then splits into two paths:

- A **Fixed latency** path, or synchronous bit (s-bit): the digital information from two neighbouring strips and combined in OR is called synchronous bit (s-bit), and it is sent sent to back-end, functioning as a trigger. The purpose is to provide fast "hit" information that is synchronous with the LHC 40 MHz clock.
- A **Variable latency** path: full granularity data, i.e. signals from every single strip, are sent to the back-end when a level-1 accept (L1A) arrives from the back-end with a fixed delay. The synchronized digital signal is first extended in time by a programmable number (from 1 to 8) of clock cycles (the *pulse stretch*), and then stored at the beginning of a circular buffer (SRAM1) of 1024 bit depth; at each clock cycle, the signal advances by one bit in the buffer. When the chip receives an external L1A trigger signal, the bit stored at a specified depth in the SRAM1 is copied to a second buffer (SRAM2); the latter is a FIFO where the data are identified by their bunch counter (BC) and event counter (EC), before being transmitted to the backend. The depth of the bit in the SRAM1 at the arrival of an L1A is called latency and represents the delay between the time of formation and arrival of the external trigger and the signal formation and processing in the detector and front-end.

The chip is also provided with a calibration, bias and monitoring unit, that allows for taking scans and applying various configurations to the chip. In particular, the calibration system provides internal charge pulses to the input of the front-end amplifier, with magnitude, phase, and polarity programmable by the user. This feature helps significantly in the tests and characterization stage.

3.3.2 The optohybrid

The optohybrid is a concentrator board, shown in Figure 3.9A, providing an interface for the VFAT3 readout with backend and trigger. It converts optical data into electrical data. The communication is bidirectional:

- **VFAT3 to backend**: the Optohibrid receives data from the VFAT3 and transmits them to the back-end after compression;
- **backend to VFAT3**: the Optohybrid sends slow-control[4] commands from the back-end to the on-detector electronics.

It is made of two main components:

- **Gigabit transceiver (GBT)**: it receives and transmits data from the VFATs and communicates with the back-end through the VTRx. In particular, ME0 employs lpGBT (Low Power GBT), a radiation-tolerant device designed for HL-LHC detectors [71], which supports data transmission up to 10.24 Gbps;

[4]Slow Control Systems are used for setup and monitoring of hardware that is not time-critical, and can be run at a low priority

- **Versatile transceiver (VTRx)**: it allows the communication between back-end and on-detector electronics; it converts optical data to electrical data (electro-optical transceiver). The GE2/1 OptoHybrid uses the VTRX chip, replaced by the upgraded VTRX+ in ME0; the former ensures a data transmission rate of 4.8 Gbps, while the latter can reach up to 5.12 Gbps in reception and 10.24 Gbps in transmission.

In GE1/1 and GE2/1, the OH is also provided with an FPGA to cluster VFAT s-bit data and compress them to send to the trigger board. Nevertheless, the latter cannot be employed in ME0 due to the radiation hardness requirement, so its functionality is provided by the back-end.

3.3.3 The GEM electronic board

The VFAT3 and OptoHybrid are mounted on the detector through the GEM electronic board (GEB), a PCB attached to the detector readout board that routes the data and power lines, and works as a mechanical support for the front-end electronics. The low-voltage power provided to the GEB is distributed to DC-DC converters (bPOLs) and from those to the other components. The design of the ME0 GEB is shown in Figure 3.9B: it is made of two separate PCBs along the η direction, called *wide* and *narrow* GEB; each GEB powers 2 OptoHybrids and 12 VFATs.

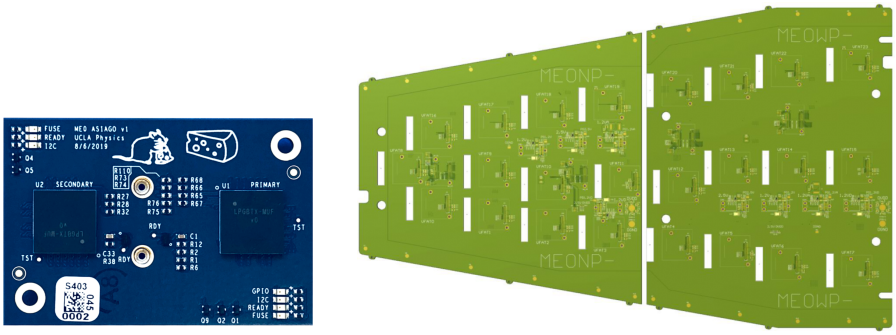

(A) (B)

FIGURE 3.9: (A) Picture of an ME0 optohybrid. (B) Design of the ME0 wide and narrow GEBs.

3.4 Back-end electronics

The back-end electronics stands between the front-end electronics and the CMS Trigger and Data Acquisition system. It is located off-detector and is subject to much less stringent requirements on radiation hardness. The ME0 back-end electronics is planned to be based on the common CMS Phase-2 technology choice, namely the ATCA standard [72], which employs advanced mezzanine cards (AMCs). The back-end electronics performs several operations:

- Programs OHs and FPGAs;
- Provides the clock and TCDS[5] commands to the front-end;

[5]The CMS Timing and Control Distribution System (TCDS) is the upgraded version of the Trigger, Timing and Control (TTC) system, which is responsible for the synchronization of the different detectors to each other and to the passage of particles. It distributes the clock and the commands to all the detectors.

- Receives trigger data from the front-end and sends it to L1 trigger system;
- Sends trigger signal (L1A) to the VFATs, and receives event data back;
- Packages data from multiple chambers (and multiple VFATs per chamber) corresponding to the same BX and sends it to the CMS DAQ system;
- Slow control: configure front-end electronics and monitor front-end data.

These functionalities are similar to those provided by the CTP7 μTCA (earlier format of the ATCA) boards that have been adapted for the GE1/1 DAQ system.
Each backend crate also hosts a standard CMS "communications" board responsible for common clock and control, as well as communications with the central CMS DAQ and Trigger systems (AMC13 board for the μTCA crate, DTH board for the ATCA crate).

At the moment both CTP7 μTCA and X2O ATCA boards are used. The former is used in the GE1/1 and GE2/1 detectors currently installed at CMS and in the ME0 test stands, while the latter is currently used for GE2/1 quality-control tests and will be installed for all GEM systems in Phase-2. A summary of the crate and back-end usage is outlined in Table 3.1.

Crate	Back-end board	Used in	Can read...
µTCA	CTP7	GE1/1 in P5 GE2/1 in P5 ME0 test stands	1 ME0 stack
ATCA	X2O	GE2/1 QC8 All GEM systems in Phase-2	2 ME0 stacks

TABLE 3.1: Crate and Back-end board usage

3.5 Data Acquisition Software (DAQ)

The GEM online software [63] is based on the libraries of the CMS DAQ framework, xDAQ. The core part of the data acquisition software is a set of tools that allow the interfacing of the xDAQ applications with the slow control of the back-end board: for each firmware block in the FPGA, a remote procedure call (RPC) server implements high-level DAQ functions (such as the launching of a calibration routine or the configuration of a front-end component) and processes requests from the AMC-Manager applications. The lower-level access to the FPGA registers from the RPC servers and other stand-alone tools is mediated and synchronized by a memory-access layer (memhub). The GEMSupervisor xDAQ application implements a finite state machine that handles the operations necessary for the data taking (e.g. configuration of the front-end or beginning of a run); a single xDAQ client instance allows the operation of the software through a web interface.

3.6 Power system design

3.6.1 High Voltage system

To power a triple-GEM, a total of seven different high-voltage potentials have to be applied to its electrodes. During the R&D phase, these voltages were achieved with

a single HV channel using an on-chamber resistive divider circuit. Figure 3.10 shows a triple-GEM chamber powered via a resistive divider circuit. This technique does

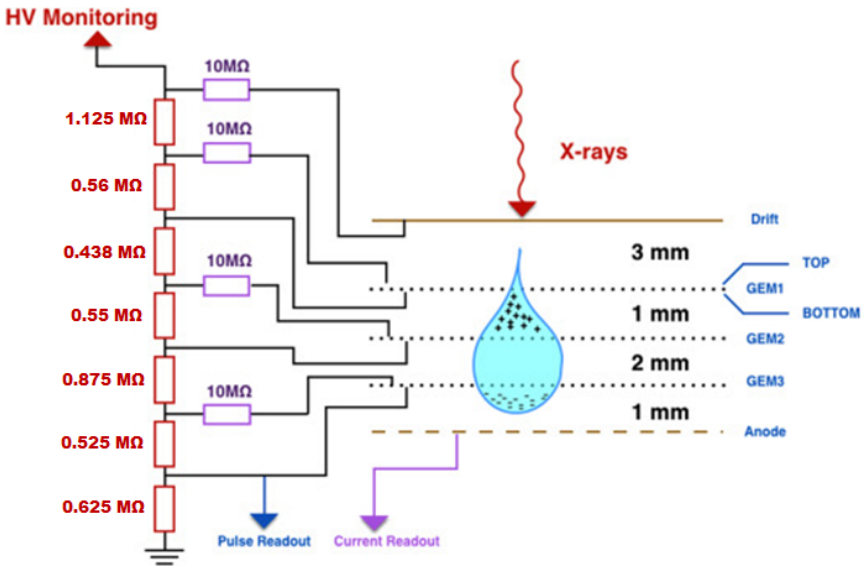

FIGURE 3.10: Schematic of a triple-GEM chamber powered using the resistive divider circuit employed for CMS GEM detectors. Protection resistors are also shown, with their typical value.

not allow for per-channel current measurements or working point optimization, and if an HV segment is in short, the divider current also starts flowing through the protection resistor, in parallel with the divider resistance. This causes the value of the divider current to change, introducing a bias in the operating voltages. An easy computation can be performed considering, for example, a short between GEM3 top and GEM3 bottom, the divider current that initially is $R_{tot} = \sum_i R_{div,i} = 4.698\,\mathrm{M\Omega}$ becomes:

$$R'_{tot} = \sum_{i \neq GEM3} R_{div,i} + \frac{R_{div,GEM3} R_{prot}}{R_{div,GEM3} + R_{prot}} = 4.673\,\mathrm{M\Omega}\ .$$

Assuming a HV working point of 3000 V:

$$I = \frac{HV}{R_{tot}} = 638.5\,\mu\mathrm{A} \rightarrow I' = \frac{HV}{R'_{tot}} = 642\,\mu\mathrm{A}\ ,$$

which can cause an increase in voltage up to 4 V (for the drift gap).
Moreover, the divider constitutes a significant local heat load inside the closed volume of the chamber.
To overcome these issues, the seven channels will be powered individually using the CAEN A1515TG multi-channel HV power supply [73], specifically designed for triple-GEM detectors. One A1515TG board provides 14 floating HV channels, grouped in two complex channels. The seven channels within a complex channel can be configured individually and the diagram of the currents per electrode is shown in Figure 3.11. The floating design assures that the failure of one channel does not introduce an increased potential on the neighboring layer.

Other important protections implemented in the on-board firmware include overheating detection, an external hardware interlock, and a maximum voltage setting to protect the detector against human errors. The A1515TG module allows for 1 kV

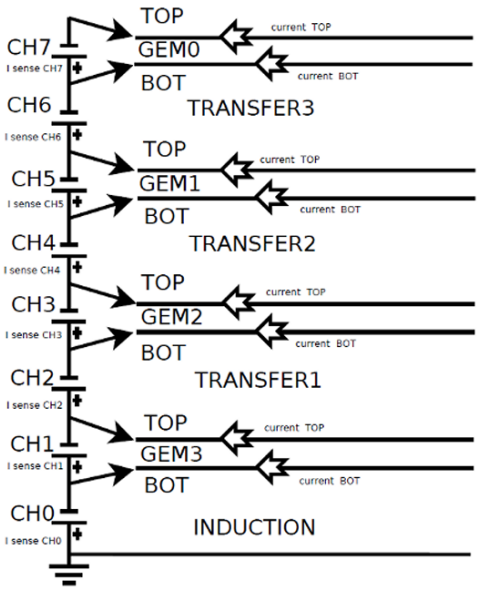

FIGURE 3.11: GEM current distribution in the CAEN A1515TG multi-channel HV supply.

and 1 mA per channel, with a limit of 0.7 W per channel.
Since the multi-channel HV supply requires special connectors and cables, it is customary in laboratories to operate triple-GEM detectors using a voltage divider. Therefore, when using a multi-channel HV power supply the equivalent divider current is used to define the HV point at which the triple-GEM detector is working. The equivalent divider current is the current that would flow through the divider if a voltage equal to the total voltage applied to the detector via a multi-channel HV system is supplied. Table 3.2 contains the set of values of the resistance defining the divider, and for each HV point, expressed in equivalent divider current, the corresponding voltages applied to each foil are listed.
The voltage for each channel can be set and read with a 20 mV resolution, and an accuracy of 0.2%$\pm$0.2 V$\pm$50 ppm/°C, and current limits are set with a 20 nA resolution. Below 100 µA, the current can be monitored with a resolution of 100 pA, and in the range of 100 µA to 1 mA, the resolution becomes 1 nA with accuracy of 0.5%$\pm$5 nA$\pm$50 ppm/°C. The ramping speed can be adjusted from 1 V s^{-1} to 100 V s^{-1} in steps of 1 V, and the maximum time an overcurrent is allowed to last, i.e. the trip time, can be set from 0 s to 100 s in steps of 0.1 s. As a consequence, spikes lasting less than 0.1 s are not monitored.

3.6.2 Low Voltage system

The main power source for the on-detector electronics is located in the experimental cavern close to the chambers. The reason for this location is that cable length must be minimized to reduce as much as possible the voltage drop due to the resistance of the cables[6]. That sets additional requirements in terms of radiation hardness and operation in the presence of magnetic fields. The baseline LV system for ME0 (and GE2/1) relies on the EASY3000 family of boards manufactured by CAEN [74].

[6]For the high voltage supply, the voltage drop caused by the resistance of the cables is negligible.

$R_{EQUIV}(M\Omega)$	I divider (μA)	620	650	670	680	700	710
1.125	**Drift (V)**	697.5	731.3	753.8	765	787.5	798.75
0.56	**GEM1 (V)**	347.2	364	375.2	380.8	392	397.6
0.438	**Trans1 (V)**	271.6	284.7	293.5	297.8	306.6	310.98
0.55	**GEM2 (V)**	341	357.5	368.5	374	385	390.5
0.875	**Trans2 (V)**	542.5	568.7	586.2	595	612.5	621.25
0.525	**GEM3 (V)**	325.5	341.3	351.8	357	367.5	372.75
0.625	**Induct (V)**	387.5	406.3	418.8	425	437.5	443.75
4.698	**Vmon (V)**	2913	3054	3148	3195	3288.6	3335.58

TABLE 3.2: Set of the values of the resistors defining the equivalent voltage divider, and for each HV point, expressed in equivalent divider current, the corresponding voltages applied to each foil are listed. V_{MON} is the total voltage supplied.

3.7 Electronics calibration and configuration

To properly operate the CMS GEM system, both the VFAT3, there is a certain amount of scans to be carried out. Indeed, the operation of the detector requires establishing communication with the front-end electronics, calibrating the internal DACs of the VFATs to determine the correct front-end bias, determining the discriminator threshold for an allowed noise rate and setting the optimal latency. In the following sections, an outline of the main scans for the operation of the CMS GEM system is provided.

3.7.1 GBT phase scan

The GBTs allow the communication of the VFAT3s with the back-end. The eLink between the GBT and the VFAT3 transmits in separate lines both data and the clock received from the LHC. However, delays in the transmission lines and in the front-end circuits do not ensure that the transmitted signals are always in phase with the clock. For this reason, the GBT allows shifting the phase of the eLinks with respect to the clock in a full clock cycle by multiple of 50 ps. A phase alignment routine, the GBT phase scan, in performed to choose the optimal eLink phase for each VFAT3 to ensure that the data received by both ends are always sampled correctly. Indeed, when the GBTs receive data back from the component, they have to sample them in the middle of the signal, and not in correspondence of its edges.
However, the received signal and the internal GBT clock have random phases, different for each component on the GEB. In order to solve this lack of correspondence, a scan of the GBT phase needs to be performed over all the components. Such scan consists of:

1. sweeping all the possible GBT phases;
2. for each phase, sending signals to the component and check if they respond correctly;
3. setting the *optimal* phase as the one which gives least errors.

Without the correct phases, communication with VFATs is not possible.

3.7.2 DAC scan

The VFAT3 analog part has several front-end circuits (the preamplifier, the shaper, and the CFD), that need to be precisely biased for compliance with the nominal performance of the chip. Table 3.3 lists the bias point of different parts of the analog front-end and their nominal value; the current values are set by the voltage sources with a 10 kΩ input resistor.

DAC	**Bias current (μA)**	**Bias voltage (mV)**
Preamplifier bias input transistor	150	1500
Preamp bias leakage compensation	25e-3	0.25
Preamp bias source follower	26	260
Shaper bias folded cascade	26	260
Shaper bias input pair	16	160
Single-differential bias input pair	28	280
Single-differential bias folded cascade	27	270
Single-differential bias source follower	30	300
CFD bias 1	20	200
CFD bias 2	20	200
Preamplifier Vref	/	430

TABLE 3.3: DAC Bias Parameters.

The bias currents (or voltage) can be tuned by an 8-bit or 6-bit digital-to-analog converters (DACs). The set value, in volts or microamperes, can be monitored via the analog-to-digital convers (ADC) integrated within the chip. The procedure followed to determine the required bias point in terms of DAC units is the following:

1. each DAC range is swept between its minimum and maximum value (0 to 63 for the 6-bit registers, 0 to 255 for the 8-bit ones);
2. the corresponding currents are read through ADC;
3. the *optimal* DAC value is chosen by interpolation as the one corresponding to the nominal bias currents (voltage).

3.7.3 S-bit rate scan

Each VFAT3 has a register corresponding to an arming comparator threshold, that is the same for the entire chip. The s-bit rate scan is the procedure typically followed to determine for a given VFAT the optimal threshold value for the arming comparator. The s-bit rate is computed counting the number of trigger hits given by the logical OR among the 64 bits, each of them being the OR of two channels (VFAT half granularity datapath).
To decide the best value for the threshold, the following procedure is followed:

1. the detector HV system is turned off, in order to neglect particles interacting with the medium while doing the scan, which would eventually affect the s-bit rate measurement;
2. Since the arming comparator threshold is set via a 8-bit DAC, all its possible values are set one by one, from 0 to 255 DAC units;

3. for each value of the threshold, the s-bit rate is read;

4. the optimal threshold is the DAC value corresponding to the desired noise rate (e.g. 100 Hz).

In Figure 3.12A a typical example of s-bit scan plot is shown. The threshold in DAC units can be converted to charge by using the s-curve result (See Section 3.7.4).
In addition to the optimal threshold, the s-bit scan can help to identify broken s-bit lines, indeed such scenario is characterized by a measured s-bit rate being constant and equal to its maximum value, namely the 40 MHz of the LHC clock. An example of s-bit scan for a broken s-bit line is shown in Figure 3.12B. Also detector gain problems can be identified, if there is no plateau with the HV system on.

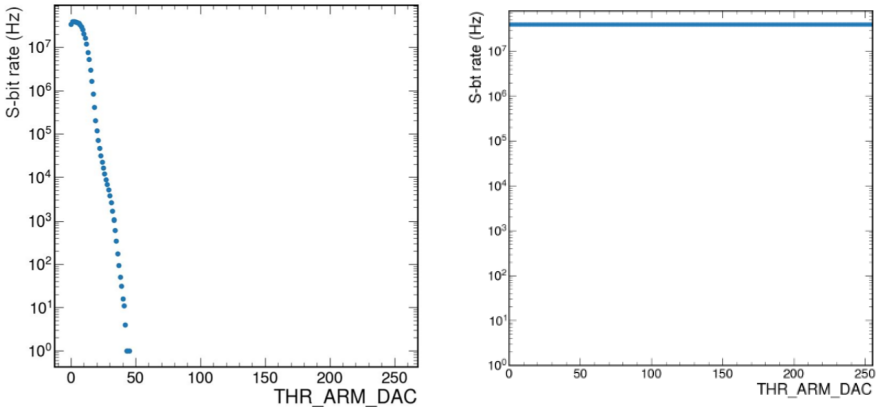

(A) (B)

FIGURE 3.12: (A) Example of a s-bit scan for a well-functioning VFAT3 chip. Here the threshold corresponding to a 100 Hz s-bit rate is ∼45 DAC units. (B) Example of a s-bit scan for a broken s-bit line.

3.7.4 S-curve

Since the VFAT3 has a digital readout, the noise of the setup cannot be evaluated by taking a pedestal run[7]. Nevertheless, as previously mentioned, the chip allows to inject pulses on each channel with an internal circuit and counts how many signals are read back. This functionality allows for a measurement of the noise. The procedure to follow for each VFAT3 channel is the following:

1. An arbitrary VFAT3 threshold is set;

2. the charge of the internal pulse is set via an 8-bit DAC, at each step changing it within all the possible charge values (from 0 to 255 DAC units);

3. for a fixed threshold, 100 pulses are sent to the VFAT3;

4. The number of recorded signals as a function of the amount of charge returns an s-shaped curve;

[7] A type of run that consists of taking data with a random trigger, in such a way that the amplitude spectrum gives the distribution of the noise "hit" amplitudes. This spectrum represents the "pedestal" in physics run.

The typical "S" shape is due to the presence of electronic noise in the analog readout chain of the chip. Conversely, in a noiseless environment, a step shape would be expected for this kind of measurement, with 0 counts when the injected signal is under threshold, and 100 counts when the signal is over threshold. The presence of the noise running above the injected signal determines the sigmoidal shape of the curve. Performing the fit with a sigmoidal function, the mean μ of the fitting function represents the threshold of the single channel, while the parameter σ represents the width of the temporal noise of the channel. Figure 3.13A shows a typical example of S-curve taken for a prototype of ME0 triple-GEM and Figure 3.13B is the summary for an entire VFAT3 chip.

Moreover, such a scan is also helpful to find either dead or detached channels.

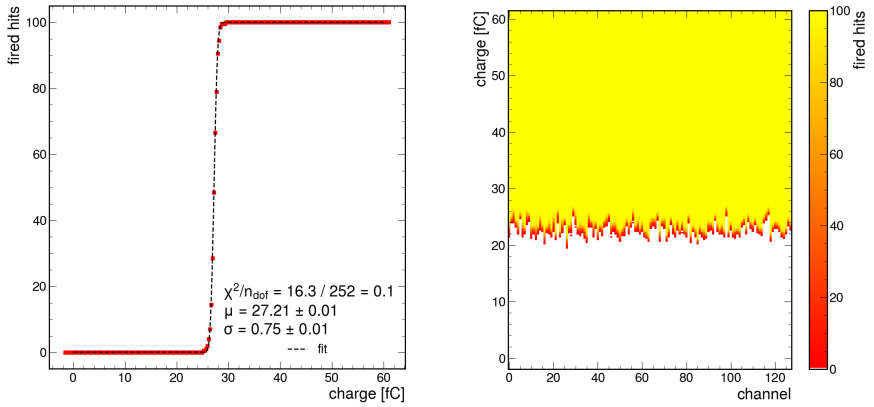

(A) (B)

FIGURE 3.13: (A) S-curve obtained for one VFAT3 channel. The dashed black line represents the fitting error function and the parameters μ and σ are shown in the plot. (B) 2-dimensional s-curve for one VFAT3.

Additionally, the s-curve scan can be used as a tool to improve the alignment of the local thresholds of the single channels of a VFAT chip. The need for such an alignment stems from the fact that, although the threshold is set for the entire chip, the arming comparator, due to production details, can apply slightly different local thresholds to signals. These fluctuations of the local threshold can cause a decrease in efficiency of the chip, because lower local thresholds make it necessary to increase the global threshold (to remain at an s-bit rate of 100 Hz per VFAT3), resulting in a possible decrease in efficiency for those channel with a higher local threshold if the threshold set exceeds the amplitude of the physics signal.
Such alignment procedure is called *trimming* and there are two main techniques to perform it: either align the μ of the sigmoid fitting the s-curves or align their rising point. Given μ and σ the fitting parameters, the rising point, X, can be defined as:

$$X = \mu - \mathrm{n} \times \sigma \, ,$$

where n is an integer, whose value is set to 4, according to the stability observed in previous tests [75]. Tests performed over a GE1/1 stack [75] have shown that the alignment of the rising point is more effective in enhancing efficiency, while the alignment of the μ is driven by the noisier channel and leads to higher global thresholds. The alignment of the rising point X to its average value implies that the noisier channels are set to have a larger individual threshold and all other thresholds become aligned to a common lower value. Figure 3.14A shows the s-curves for all

the 128 VFAT3 channels before and after the trimming procedure. As a result, the alignment of the local threshold is meant to decrease the necessary global threshold to be set. This effect is evident from the plot in Figure 3.14B where the distribution of the global thresholds obtained from the s-bit scan before and after trimming are compared. On average, the threshold decreases and, in addition, the distribution appears to be slightly narrower, implying that the thresholds of different VFAT3 become closer with each other resulting in a more uniform signal response of the chamber.

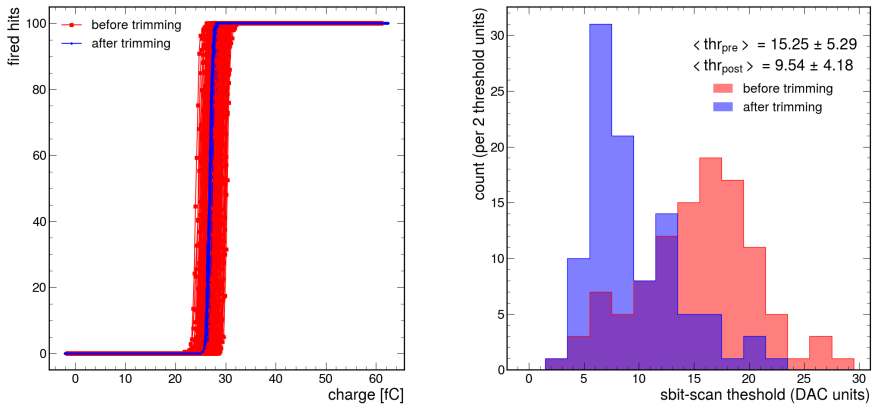

(A) (B)

FIGURE 3.14: (A) S-curves for the 128 channel of a VFAT before (in red) and after (in blue) applying the trimming procedure.(B) Distributions of the reasonable thresholds (@100 Hz) measured with the s-bit scan before and after applying the trimming procedure.

3.7.5 Latency scan

The content of the VFAT3 SRAM2 (data path) is read out to back-end whenever a trigger signal (L1A) is received. However, the L1A is not routed to the GEM electronics exactly when the GEM signal arrives to the VFAT3. Delays are generated by the backend board and the trigger system, as schematically depicted in Figure 3.15A. The VFAT3 needs to look back in time for when the correct signal arrived: this delay is called *latency*. The latency of the setup is set via a latency scan that is articulated in the following steps:

1. the detector HV system is turned on;
2. the possible range of latencies is swept, from 0 to 1023 in DAC units (corresponding to the range 1 BX - 1024 BX);
3. the number of hits recorded from the detector at each latency is counted;
4. the "optimal" latency is the one corresponding to the largest number of hits.

Figure 3.15B shows an example of a latency scan, in which the optimal latency is 20 BX (500 ns).

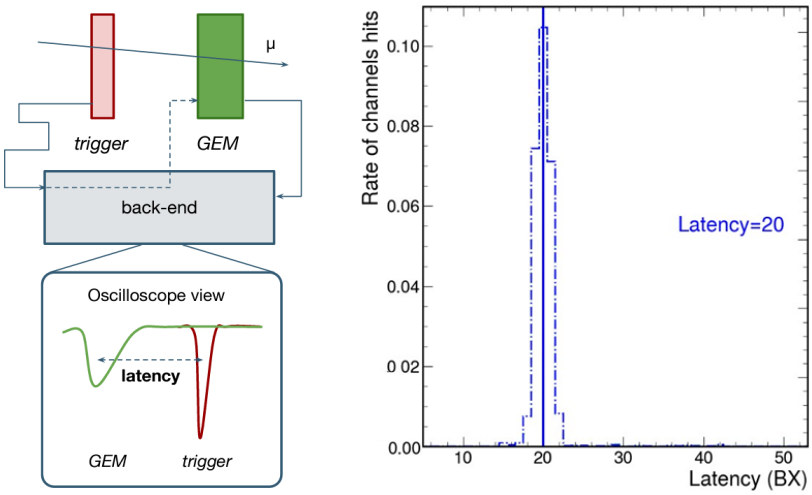

(A) (B)

FIGURE 3.15: (A) Schematic of a general setup (GEM detector+trigger+back-end electronics) outlining the different paths the trigger signal and the GEM signal follow, causing the latency to arise. (B) Example of latency scan performed with a GEM detector, the peak represents the "optimal" latency.

Chapter 4

CMS ME0 performance in high background rate environment

The present chapter summarizes the analysis of the performance of a 4-layer prototype of ME0 stack in a high-rate background environment, emulating the expected background of HL-LHC. The chosen place to perform such measurements is the Gamma Irradiation Facility (GIF++) located at CERN in the North Area, on the H4 beam line. The GIF++ provides a 14 TBq[1] ^{137}Cs radioactive source, allowing the measurement of MIP detection efficiency under uniform irradiation. A two-week test beam campaign in the GIF++ was carried out in July 2023 with a stack of 4 layers of ME0 triple GEM prototypes. I have carried out the tests for the calibration and configuration of the stack (discussed in Section 3.7) in the laboratory, participated in the installation, commissioning, and calibration of the test beam setup in the experimental area. Finally, I have taken the data during the test beam and analyzed them to obtain all the performance results shown in this chapter. The goal of the GIF++ test beam has been measuring the efficiency of each ME0 detector in the four-layer stack as a function of the background particle rate to determine the rate capability of the system.

4.1 GIF++ at CERN

4.1.1 General features

Located at the H4 beam line in the EHN1 building, the GIF++ [7] combines a ^{137}Cs source, with two sets of adjustable filters to vary its intensity, and a high-energy muon beam (around 100 GeV/c) from the secondary SPS beam. The ^{137}Cs isotope was chosen instead of ^{60}Co due to its long half-life of 30.17 years, leading to a smaller decrease of the photon rate over the expected lifetime of this facility. The high photon background rate generated by the ^{137}Cs is used to emulate the background radiation at LHC experiments, and consequently to study the behavior of detectors in tracking muons in such environmental conditions. The layout of the GIF++, together with the typical frame of reference adopted, is shown in Figure 4.1A.
The muon beam is generated as a secondary beam from the primary SPS proton beam on a production target. The spectrometer of the H4 beam line allows the beamline user to choose the nominal momentum of the secondary beam with a maximum momentum of 400 GeV/c. The muon beam, in the energy range of 57-100% of the nominal beam energy, is mainly generated by the decay of pions and kaons produced in the primary target.

[1] in March 2015 [7]

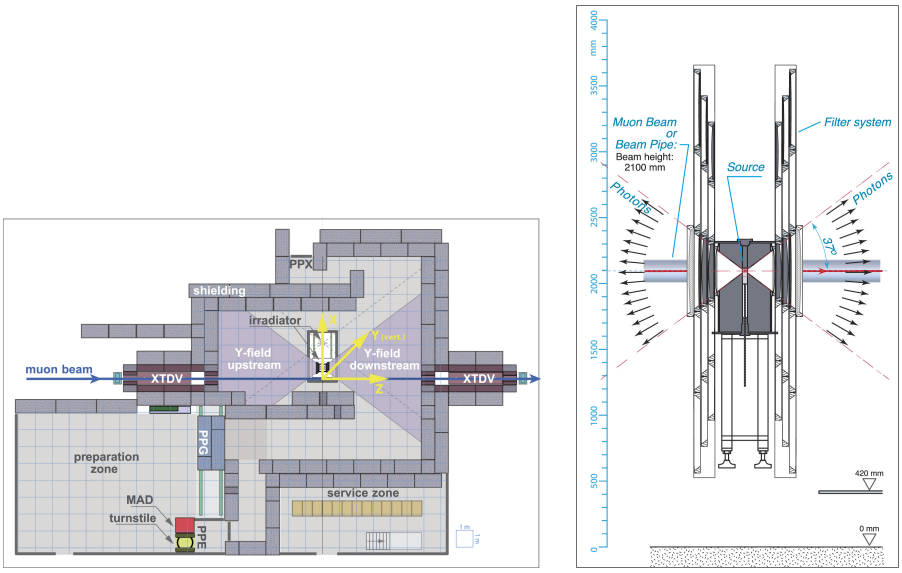

(A) (B)

FIGURE 4.1: (A) Floor plan of the GIF++. In yellow the GIF++ typically adopted frame of reference. (from [7]) (B) Irradiator with filter system at GIF++. (from [7])

4.1.2 Characteristics of the photon flux

The GIF++ source is a point source, with $1/r^2$ of the flux; however, two $\pm 37°$ panoramic collimators are installed so that the wavefront is approximately planar (xy plane). The GIF++ irradiator and its filter system are depicted in Figure 4.1B.
Embedded inside a common enclosure, two complete and independent attenuation systems are available, each consisting of an array of 3×3 convex lead attenuation filters, to fine-tune the photon flux for each irradiation field individually. The total attenuation factor, obtained by combining the three filter layers, can be set via a dedicated control panel. In total, 24 different nominal attenuation factors between 1 and 46 415 can be selected, as shown in Figure 4.2A. In the subsequent analysis, the attenuation factor will be also denoted as *ABS factor*.

According to the Lambert law [8], the intensity of a photon beam traversing a thin absorber material of thickness z is described by the formula: $I(z) = I_0 e^{-z/\mu}$, where μ is the absorption length of the material. In the GIF++ framework, the attenuation factor is $ABS = e^{z/\mu}$, where the material thickness, z/μ, depends on the absorbers' thickness and material composition. Then, the Lambert law can be rewritten, in terms of ABS factor, as:

$$I(ABS) = I_0 \frac{1}{ABS} \,. \tag{4.1}$$

The ABS factor provides information about the intensity of the photon flux, while its energy spectrum depends on the characteristics of the radioactive source and on the elements of the facility the photons interact with.
Figure 4.2B shows the typical processes of radioactive decay of a ^{137}Cs atom. ^{137}Cs decays with a half-life of 30.17 years by emitting a β-particle, i.e. a high energy electron. In 94.6% of the cases the electron carries away an energy of 512 keV and the ^{137}Cs transmutes into a meta-stable state of the ^{137m}Ba. The excited state ^{137m}Ba is characterized by an excitation energy of 661.7 keV, and it decays with the half-life of 2.55 minutes into the ground state of ^{137}Ba, which is stable. This decay occurs

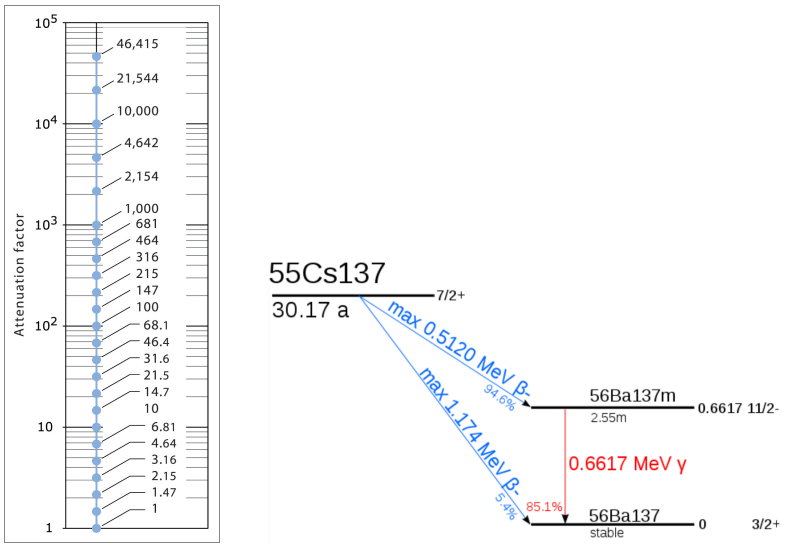

(A) (B)

FIGURE 4.2: (A) Nominal attenuation factors at GIF++. (from [7]) (B) ^{137}Cs beta decay modes. (from [76])

in the 85.1% of cases via the emission of a 661.7 keV photon, otherwise alternative, non-radiative, processes take place.
Nevertheless, the actual spectrum of the photon background in the facility is affected by the interaction of photons with the materials present in GIF++: lead (irradiator, filters), steel (filters, floor), aluminum (filters), and concrete (surrounding bunker enclosure). For the available photon energies ($\sim$662 keV), the main processes involved are Compton scattering and photoelectric effect, which cause an overall degradation of the emitted photon energy. Figure 4.3A shows the simulated spectral shape of the degraded photons for photons emerging from the capsule, from the angular correction filter, and from an exemplary attenuation filter of nominal factor 100.
Referring to the range of energies of the GIF++ photon flux ($\lesssim$662 keV) and considering the Ar:CO_2 (70:30) cross-section for photon interaction (see Figure 1.3), the main interaction mechanism of the GIF++ photon flux with CMS ME0 triple-GEM detector is the photoelectric effect of low energy photons ($\lesssim$100 keV). The photoelectric effect is characterized by the emission of an atomic electron (with either a fluorescence photon or an Auger electron), with an energy similar to the energy of the impinging photon. In this range, the electron energy loss is between 1-2 times the typical MIP energy deposit ($\sim$3-6 keV cm^{-1}, according to the computation in Section 1.2.1).

4.1.3 Dose rate at GIF++ vs ME0

Figure 4.3B shows the simulated absorbed dose rate in the air in the xz plane of the GIF++ bunker, when the irradiator is fully opened downstream (ABS=1) and fully closed upstream, that is the configuration used in the current test beam, as downstream and upstream zones are basically independent. The region occupied by the detector under analysis in the current test beam is denoted with "D1" in the aforementioned picture. Consequently, the simulated absorbed dose rate is of the order of 10^5 µGy h^{-1}=28 µGy s^{-1}. On the other hand, considering the nominal HL-LHC integrated luminosity ($\sim$3000 fb^{-1}), the total simulated absorbed dose in ME0 ranges from 30 to 1000 Gy [77]. Since the LHC year corresponds to 10^7 s, in the 10 years

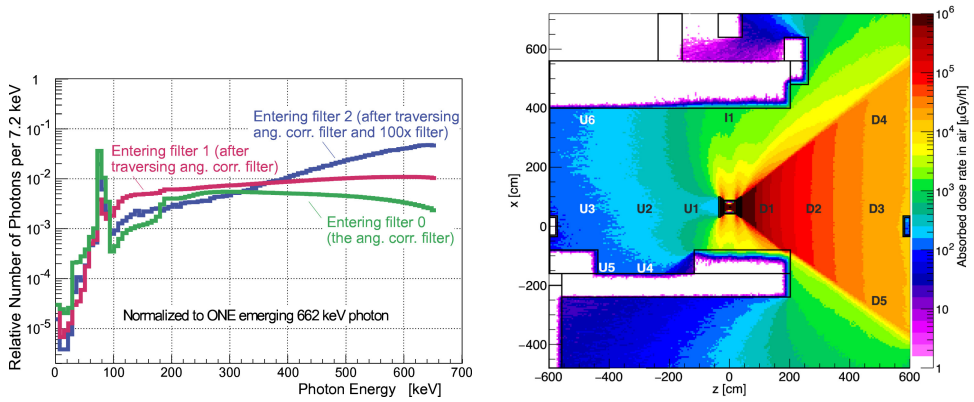

(A) (B)

FIGURE 4.3: (A) Simulated spectral shape of degraded photons for photons emerging from the capsule (in green), from the angular correction filter (in red), and from an exemplary attenuation filter of nominal factor 100 (in blue). The peak around 80 keV corresponds to the fluorescence line expected for lead. The vertical line is normalized to one emerging 662 keV photon flux. (from [7]) (B) The absorbed dose rate in air in the vertical plane through the source (xz plane) at $y = 0.65\,m$. Only downstream side opened with attenuation filters at factor 1. The horizontal axis (z coordinates) corresponds to the direction of the beam axis. (from [7])

of HL-LHC operation the maximum absorbed dose rate will be 10 µGy s^{-1}. The absorbed dose rate in GIF++ is threefold the ME0 absorbed dose rate. Nevertheless, the performance of the detector is determined by the amount of ionizing interactions the traversing particles produce. This depends on the nature of the particles composing the background and on their cross-section of interaction with the active material of the detector. The background in GIF++ is made of photons only, while in ME0 also leptons and hadrons will traverse the detector, determining a higher interaction rate.
Even when the source is "off", which means that the ABS factor is set at its maximum, the background photon rate is not zero, but, in terms of absorbed dose rate in air is 200 µGy h^{-1}= 55 nGy s^{-1} (as reference value it has been considered the one in the upstream region U1 of Figure 4.3B). Since the photon radiation weighting factor is $W_R = 1$, the effective absorbed dose rate is 55 nSv s^{-1}. To have an idea of the magnitude of such a dose, one can consider the effective absorbed rate due to the background radiation in Geneva (CH), which is around 30 pSv s^{-1} [2]. Consequently, the effective dose rate in GIF++ when the source is covered at its maximum ABS factor, is 2000 times the effective dose rate due to the background environment radiation. Analogously, the effective dose rate in GIF++ when ABS = 1 (maximum background rate) is 1 million times the background radiation effective dose rate.

4.2 Test beam setup

The detector under test is a stack of four ME0 triple-GEM detector prototypes. The four chambers are equally spaced at a distance of 3.6 cm (GEB to GEB) and held together by the mechanical structure shown in Figure 4.4A. As depicted in the aforementioned figure, only the wide GEB is instrumented. The overall schematic test-beam setup is shown in Figure 4.4.

[2]Data taken from the EU Radioactivity Environmental Monitoring webpage [78], relative to the week 23-30/06/2024.

The stack is located downstream of the ^{137}Cs source, at a distance of 90 cm from it.

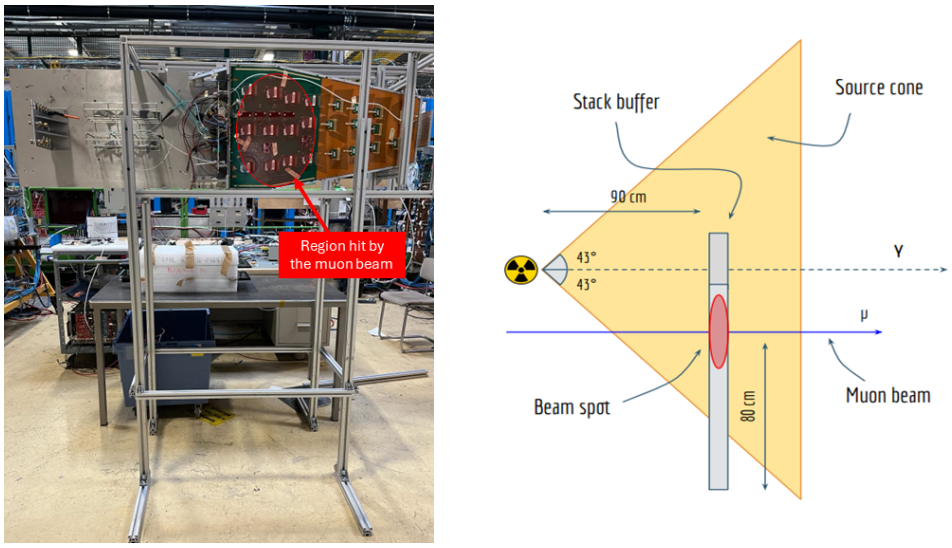

(A) (B)

FIGURE 4.4: (A) Four-layer stack with the mechanical support at laboratory 904, CERN. Only the wide GEB is instrumented. (B) Two-dimensional scheme of the test beam setup. The yellow area represents the irradiation field coverage.

This distance allows for the largest background rate ever measured in ME0 prototype test beams. The mechanical structure is attached to the facility wall by its side, in such a way that the muon beam, whose axis is at 80 cm from the wall, hits the chambers only in the instrumented region. The position of the stack in the bunker is schematized in Figure 4.4B; the yellow area in the aforementioned figure represents the radioactive source irradiation cone. It is noteworthy to observe that, due to the very short distance of the source from the stack, the irradiation field is not homogeneous throughout it.

The trigger system is made of two 30×30 cm^2 scintillators provided by the GIF++ and located outside of the irradiation cone of the source in such a way to trigger only on the muon beam. The two scintillators are read out by PMTs and the trigger signal is their coincidence. The overall block scheme of the test beam setup is depicted in Figure 4.5.

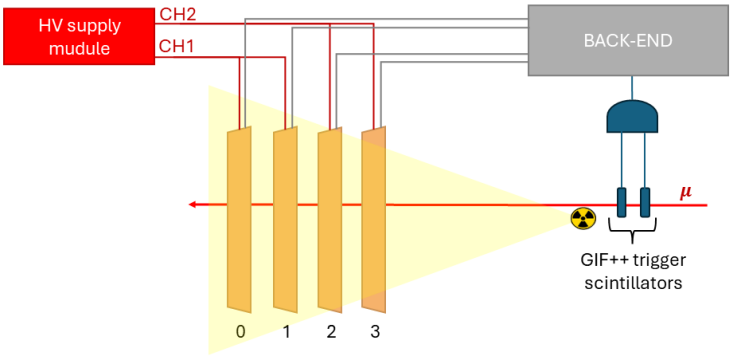

FIGURE 4.5: Overall block scheme of the test beam setup. The scintillators are out of the radiation cone, both downstream and upstream.

The readout system employed for the current test beam is shown schematically in Figure 4.6. The front-end electronics coincide with the ME0 foreseen electronics:

the VFAT3 is the front-end chip and the concentrator OptoHybrid (OH) handles the communication with the backend (as explained in Section 3.3). Regarding the back-end electronics, a commercial CVP-13 board is used. CVP-13 is a PCIe board and it is able to read 4 half-GEBs, in this case, the wide GEBs.
In the VFAT3 chip, the duration of the synchronized digital signal can be extended in time to last from 1 to 8 clock cycles (25 ns). The duration of the signal can be set by varying the pulse stretch (PS) from 0 to 7: $t_{signal} = (PS + 1) \times 25\,\text{ns}$. During the current test beam, two types of acquisition have been performed:

- the source scans: when the beam is turned off and only photons from the source traverse the detector. For these runs, the PS has been set to 0;
- the physics runs: when both the beam and the source are turned on. Since the aim of these runs is to measure the muon efficiency, the PS has been set to 7 ($t_{signal} = 200\,\text{ns}$). Indeed, the larger the PS the longer is the time window of acquisition, resulting in a higher probability of detecting the traversing muons.

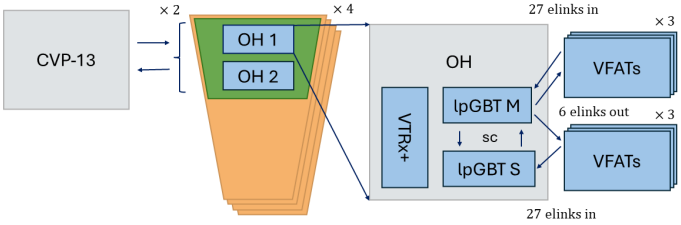

FIGURE 4.6: Scheme of the readout system used at the GIF++ test beam in 2023.

4.3 Test Beam operations

The test beam consisted of 14 days of data taking. After a first calibration step, in which s-curve scans and s-bit scans were performed, in order to check the noise level and determine a reasonable VFAT threshold, a HV scan was performed. The HV scan consists of measuring the efficiency of the detector at different HV points, in order to determine when the plateau of the efficiency is reached, and, consequently, fix a reasonable value of the high voltage point for each detector. Then, a background rate measurement has been performed, in order to determine the exact rate of interacting γ photons at different values of the attenuation factor of the source, i.e. at different ABS. Finally, a rate capability measurement was made: the detector efficiency was measured for different values of the attenuation factor, in order to establish how the efficiency varies at increasing background rates, and use its trend to infer the dead time of the detector. Additionally, when operating triple-GEM detectors in the GIF++ high rate of background, the HV drops due to the high current that flows through the protection resistors.
An HV compensation procedure is performed to apply the correct voltage to the chambers' electrodes. An outline of the compensation procedure and how it is applied in the GIF++ test beam is provided in Appendix C.

4.4 Reconstruction

Reconstruction consists of converting the binary data obtained from the detector electronics to physical objects. The track-based reconstruction chain adopted consists of three steps:

- the **unpacking**, that consists of decoding binary electronics data to information on readout channels hit event by event;
- the **hit reconstruction**, through which hits made of consecutive strips are clustered; strip clusters are mapped to a position in the detector plane to obtain reconstructed hits, also termed "rechits". The clusters are fully described by: a center, a cluster size, and an arrival time with respect to the trigger (the choice of the arrival time will be discussed in Chapter 5);
- the **track reconstruction**, consisting of fitting particle tracks from reconstructed hits to obtain a segment.

As of particular interest for the efficiency measurement, an in-depth description of the track reconstruction procedure is given. As described above, the test beam setup does not comprise external trackers, so the 4-layer stack is used standalone for the reconstruction. In particular, for each event, the "propagated hit" on the i-th chamber (i=0,1,2,3) is computed as follows:

- all the *rechits* from all the chambers except the i-th (labeled "detector under test") are fitted with a linear function, that is a "partial track". In case there is more than one rechit per chamber (i.e. multiple possible partial tracks), the one with the least χ^2 is saved and the other ones are discarded;
- the intersection of the partial track previously obtained with the plane corresponding to the detector under test returns the "propagated hit", alternatively labeled "prophit".

A scheme of such a procedure is depicted in Figure 4.7.

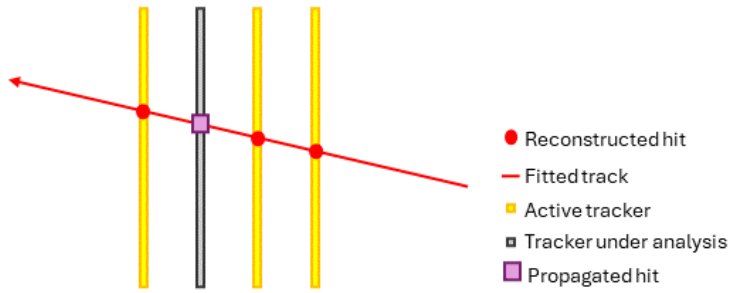

FIGURE 4.7: Schematic of the procedure used to determine propagated hits.

4.5 Analysis workflow

4.5.1 Beam profile

The detectors in GIF++ are irradiated by both the ^{137}Cs radioactive source and the H4 muon beam. "Switching off" the radioactive source (namely setting maximum

ABS = 46000), a measurement of the beam profile has been performed, in order to determine its characteristics, in terms of direction and intensity, depending on the position along the chambers. For the sake of clarity, in Figure 4.8A the frame of reference of the ME0 stack and that of the GIF++ source are shown together.
Figure 4.8B shows the shape of the beam in the x direction in the detector frame of reference, which is the vertical direction in the frame of reference of the GIF++ bunker, and over the four eta partitions.

It is apparent that the beam hits predominantly the partitions etas 1 and 2, while

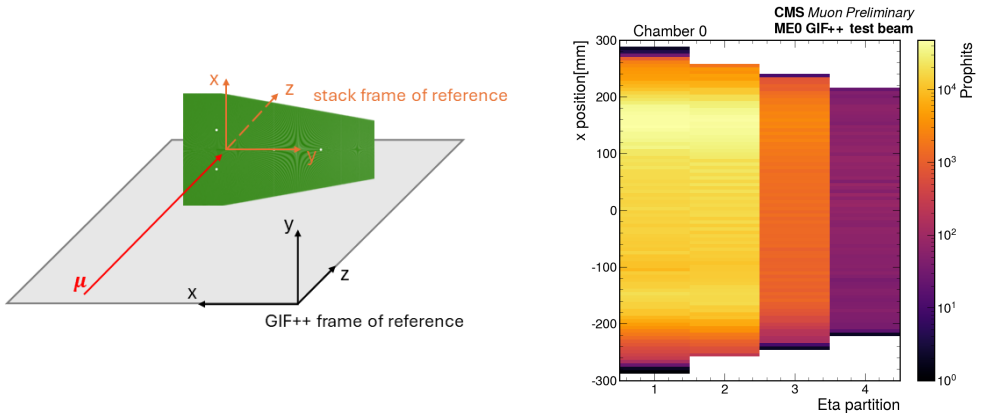

(A) (B)

FIGURE 4.8: (A) Scheme of the two different reference frames: the stack frame of reference and the GIF++ frame of reference. The red arrow represents the muon beam direction. (B) 2-dimensional prophit maps, showing the distributions of the x positions and eta partitions of the muon beam along one of the 4 stacked layers without background hits from the radioactive source. The count per bin is expressed in a logarithmic scale. These hits have been accumulated during one run lasting around 2:30 hours

its intensity sharply decreases along etas 3 and 4. Accordingly, the analysis of the efficiency has been performed only over eta 1 and 2, due to the strongly different statistics over the different eta partitions. The distribution of the size of the clusters[3] are depicted in Figure 4.9A, showing that most of the reconstructed hits are associated with clusters of size 3.

Furthermore, the track reconstruction algorithm returns the slope and the intercept of the lines obtained fitting the reconstructed hits on 3 over 4 chambers, as described in section 4.4. Figure 4.9B shows the distributions of the slopes and intercepts of the reconstructed tracks. Most of the tracks appear to be very straight, as evident from the aforementioned plot, and there is a halo of higher slope tracks, which are mainly generated by track reconstruction affected by the noise hits, or, much less frequently, by muon multiple Coulomb scattering. The shape of the halo is due to the geometric acceptance of the stack, e.g. tracks with a large positive (negative) intercept must have a large negative (positive) slope to be fully contained in the detector volume.

4.5.2 Background rate measurement at the GIF++

The intensity of the impinging photon flux on the detector is related to the ABS factor through the relation in Equation 4.1. A direct high-granularity measurement of the background rate at the GIF++ is needed to know the background rate throughout

[3] i.e. the number of strips in a cluster

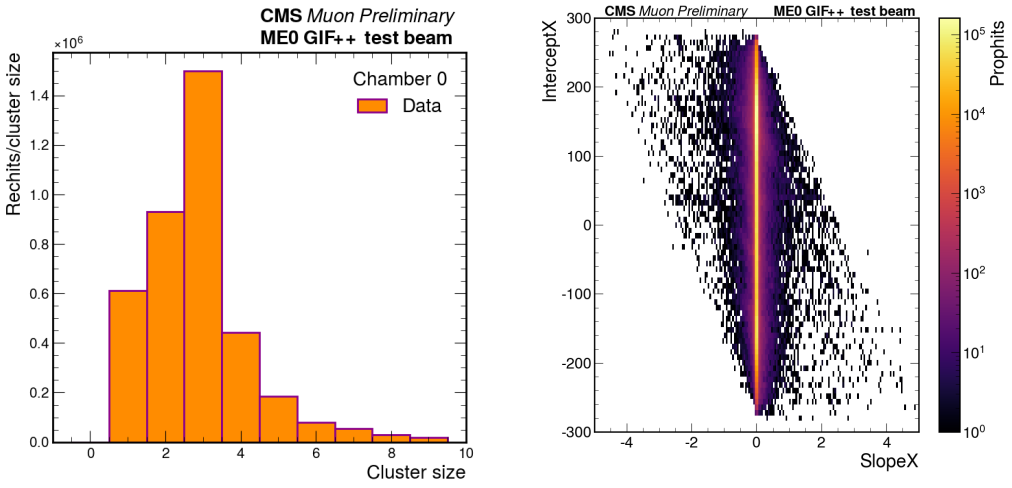

(A) (B)

FIGURE 4.9: (A) Cluster size distributions for muon hits in chamber 0. (B) 2D distribution of reconstructed tracks' slopes and intercepts.

the detector corresponding to the different values of the attenuation factor. The DAQ path was used to estimate the background rate with single strip precision on all four GEM chambers. The rate is measured with a 50 kHz cyclic trigger, configuring the VFAT3s for pulse stretch zero. Consequently, the rate on the i-th readout channel is calculated from the number of events v_i in which the i-th channel recorded hit with the equation:

$$f_i = \frac{v_i}{n \cdot 25\ ns} \tag{4.2}$$

where n represents the total number of events in the run and 25 ns is the duration of the time window opened at each trigger. Figure 4.10 shows the distribution of the measured rates. Fitting the distribution with a Gaussian, the μ parameter represents the average rate per strip on the selected eta partition of the selected chamber and the σ is the inhomogeneity of the photon flux along the partition. For the sake of clarity, the results of the background rate measurements are considered separately for low ABS values (ABS$\leq$10 or ABS^{-1} $\geq$0.1) and for high ABS values (ABS$\geq$10 or ABS^{-1} $\leq$0.1).

Concerning the measured rate at low ABS values, Figure 4.11 shows the resulting rate scan as a function of the reciprocal of the GIF++ source attenuation factor. Some preliminary observations about the measured rate can be made according to the GIF++ irradiation field, previously shown in Figure 4.3B:

- the rate is not homogeneous throughout each chamber, because of the proximity of the stack to the radioactive source. In particular, the chamber is in correspondence of the border between the core of the irradiation field (red region) and its halo (yellow region);
- due to the presence of collimators around the source, the rate per strip in the halo deviates from the Lambert law trend, and it saturates already at values of the ABS factor larger than 1.5.

The rate increases increasing ABS^{-1}, but the linearity, described by the Lambert law (here the hypothesis of a thin medium is verified), is substituted by a saturating

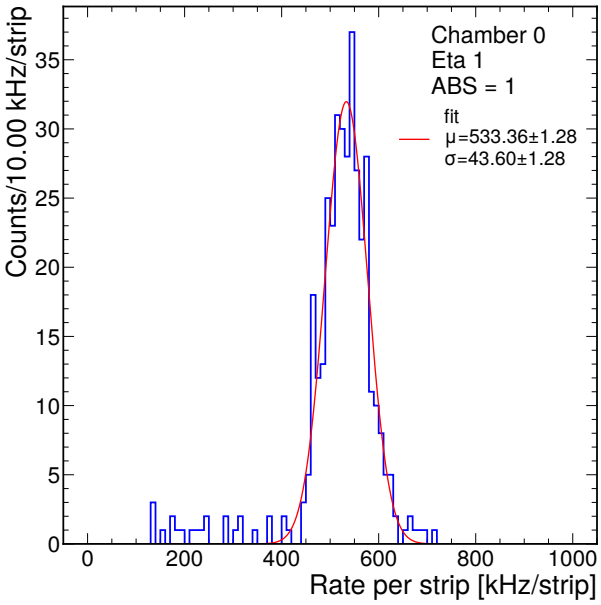

FIGURE 4.10: Rate per strip distribution. The red line is the result of the Gaussian fit.

trend. Indeed, as discussed in Appendix A, due to the detector dead time the measured rate depends on the "true" rate via the following function:

$$f(x) = \frac{mx + q}{1 + \tau(mx + q)}\,, \tag{4.3}$$

where the "true" rate is a linear function of the ABS^{-1} factor. The parameters m and q are, respectively, the slope and intercept of the line, and τ is the reciprocal of the saturation value, namely the dead time of the detector. The results of the fit are shown in Figure 4.11

The maximum rate that can be measured by each single strip is limited by the dead time of the detection system (detector+readout). Then, it must be at least larger than the dead time of the front-end VFAT3 chip, which ranges from 400 to 1000 ns; The parameter τ of the fit can be, then, interpreted as a first estimation of the dead time of the chamber. As evident from the plots in Figure 4.11, the error in the estimation of the dead time is significant due to the fact that the plateau is not reached and the uncertainty introduced by the extrapolation is considerable. As a consequence, the measurement of the dead time is less precise in the low-rate regions.

Figure 4.12 shows the average rate per strip for ABS^{-1} $\leq$0.1. While the ABS^{-1} decreases (moving towards the left-hand side of the plot) the rate first decreases linearly (as expected according to the Lambert law) but then it starts saturating. The saturation is related to the fact that lower ABS^{-1} means larger absorbers' thickness, so the hypothesis of a thin medium of the Lambert law is not valid anymore. In particular, the nominal attenuation factor is defined as attenuation of 662 keV photon flux, and for ABS factors greater than 10, the effective attenuation is considerably lower than the nominal one, since scattered photons with energy smaller than 662 keV (generated by the photon energy degradation through GIF++ instrumentation) contribute substantially [7].

Furthermore the rate per unit surface has been computed. considering the area of the strips in each partition (listed in Table 4.1). In Figure 4.13A, it is depicted the

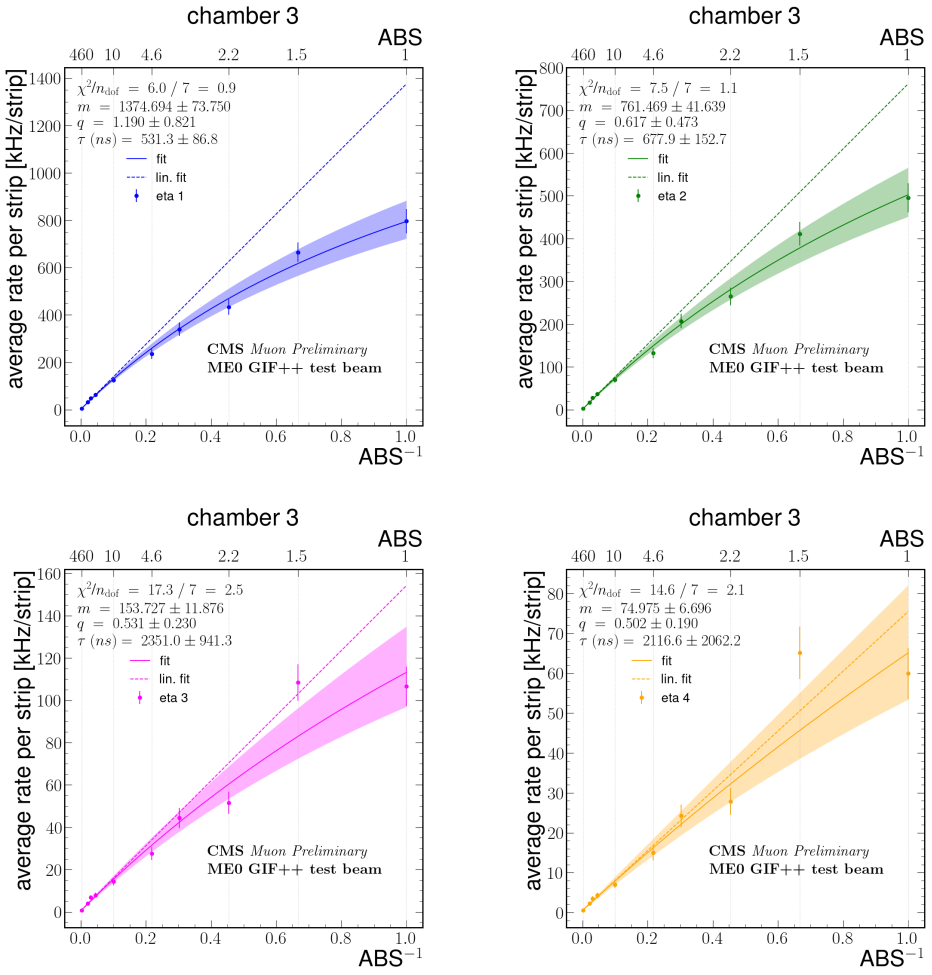

FIGURE 4.11: Average rate per strip as a function of the reciprocal of the attenuation factor for chamber 3 (the closest to the source). Fitting with the function in Equation 4.3 is performed and the shadow represents 1σ error over the fitting parameters, while the dashed line is the linearized function obtained taking only the numerator of the fitting function. In the upper x-axis, the corresponding values in terms of ABS are shown.

trend of the normalized rate per cm^2 as a function of the eta partition is approximately the same at different values of the attenuation factor. Here, the rate per cm^2 has been taken into account because of the different configurations of the strips in the 4 eta partitions considered.

Finally, in Figure 4.13B the cluster size distribution for the background hits produced by the photon flux when ABS = 4.6 is shown. It can be noted that background photons produce mostly clusters of size 1.

4.5.3 Efficiency computation

In order to evaluate the performance of the ME0 prototype to track muons under a high background rate, a measurement of the efficiency is performed.
In case of no background hits, the efficiency can be computed as follows. For each event and for each detector, the overall reconstruction process returns the reconstructed hits and the propagated hit position, obtained with the procedure described

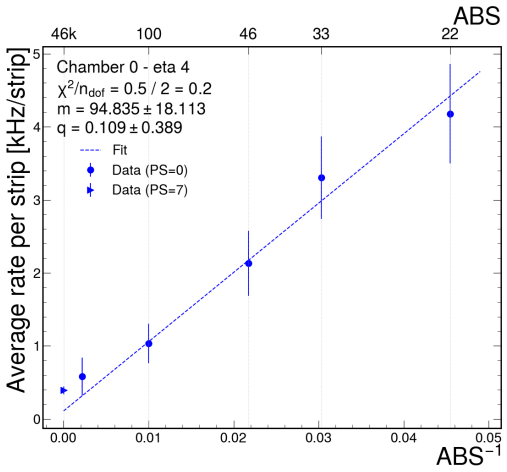

FIGURE 4.12: Measured average rate per strip for chamber 0 eta 4 for high values of the attenuation factor. The experimental points represented by dots are taken from runs with PS = 0, while that represented by the triangle (ABS=46000) from a run with PS = 7. The dashed line is the linear fit.

Eta partition	1	2	3	4	5	6	7	8
Area (cm^2)	627	549	448	336	302	246	210	158
Number of strips	360[4]	384	384	384	384	384	384	384
Area per strip (cm^2)	1.74	1.42	1.17	0.88	0.79	0.64	0.54	0.41

TABLE 4.1: Summary of the areas of the eta partitions, the number of strip and the area per strip per eta partition in a CMS ME0 triple-GEM chamber.

in Section 4.4. Then, it is considered the distribution of the track residuals, that is the distance along the x direction (in the local detector coordinates) between reconstructed hits and a propagated hit in the same detector and eta partition.
In Figure 4.14, the distributions of the residuals for each event and each chamber, are depicted[5]. Fitting the residual distributions with a Gaussian function, μ and σ can be inferred. In particular, the σ is linked to the spatial resolution of the detector, but it is influenced by the track reconstruction procedure. For the two outermost layers (0 and 3), the propagated hit position is obtained via an extrapolation, so its uncertainty will be larger and will make the σ larger than the expected spatial resolution of the chamber ($\sim p/\sqrt{12}$). As the interpolation is less affected by the uncertainty, for the two innermost layers (1 and 2) the σ is closer to the spatial resolution. Before computing efficiency, the "good" events must be selected, considering only those presenting one propagated hit in the selected detector and eta partition. In the subsequent computation, the aforementioned events will be named "filtered events". Without this selection, the events in which no muon track is reconstructed would be considered. The aim, instead, is to compute the efficiency to track muons, once that a muon track is reconstructed.
Finally, the efficiency of the i-th detector and j-th eta partition can be defined as the ratio between the number of filtered events that have at least one residual lower than

[5]When there is more than one rechit per event in the eta partition hit by the muon track, the minimum residual is considered.

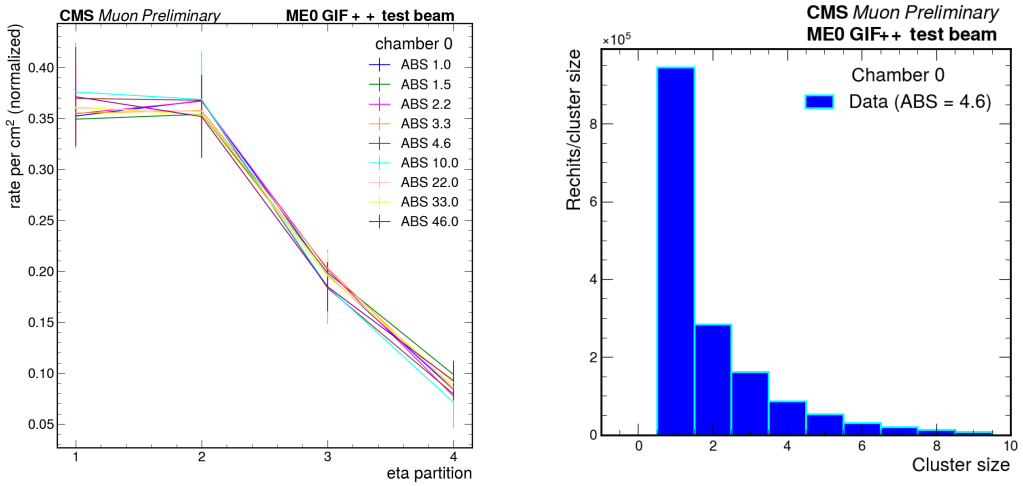

(A) (B)

FIGURE 4.13: (A) Normalized rate per cm^2 as a function of the eta partition, for different values of the ABS factor. The plot refers only to chamber 0, because the results for the other chambers have approximately the same trend. (B) Distribution of the cluster sizes of the background hits in chamber 0.

a certain multiple M of σ ("residual cut") and the total number of filtered events:

$$\epsilon_m = \frac{N(\text{filtered events} \mid \min_{x_{rec}} |x_{prop} - x_{rec}| < M \cdot \sigma)}{N(\text{filtered events})} \,. \tag{4.4}$$

However, the computation of the efficiency in the presence of background slightly differs from the procedure described above. When the background rate increases, it also increases the probability that a photon causes a strip to fire within the matching window previously defined. This can increase the number of events at the numerator of Formula 4.4, causing a measured efficiency artificially higher than the effective efficiency. Therefore, the effective efficiency is computed statistically to reject the muon contamination by background in the tracks [63]. Figure 4.15 shows the residual distribution on the ME0 detector in two runs at high and low background, respectively 4.6 and 69 in terms of attenuation factor.

As evident from the aforementioned figure, at a high background rate, there is an approximately uniform distribution of residuals out of the Gaussian core, centered in the mean of the Gaussian and $M\sigma$ large (M$\sim$3-5 is a reasonable choice, depending on the efficiency plateau). This constant background is generated by the spurious hits of the γ photons randomly distributed throughout the chambers, according to a uniform probability distribution. Due to the high contamination of background events, the efficiency cannot be measured event by event simply applying a cut on the residuals. Therefore, the number of background hits within the residual cut, i.e. fake muon hits, is estimated from the sidebands and subtracted from the count of the matching hits. To compute the efficiency statistically, we first define two classes of events:

- event A = a muon hit is found compatible with an extrapolated track position within a residual cut x_c;
- event B = a background hit is found compatible with an extrapolated track position within a residual cut x_c.

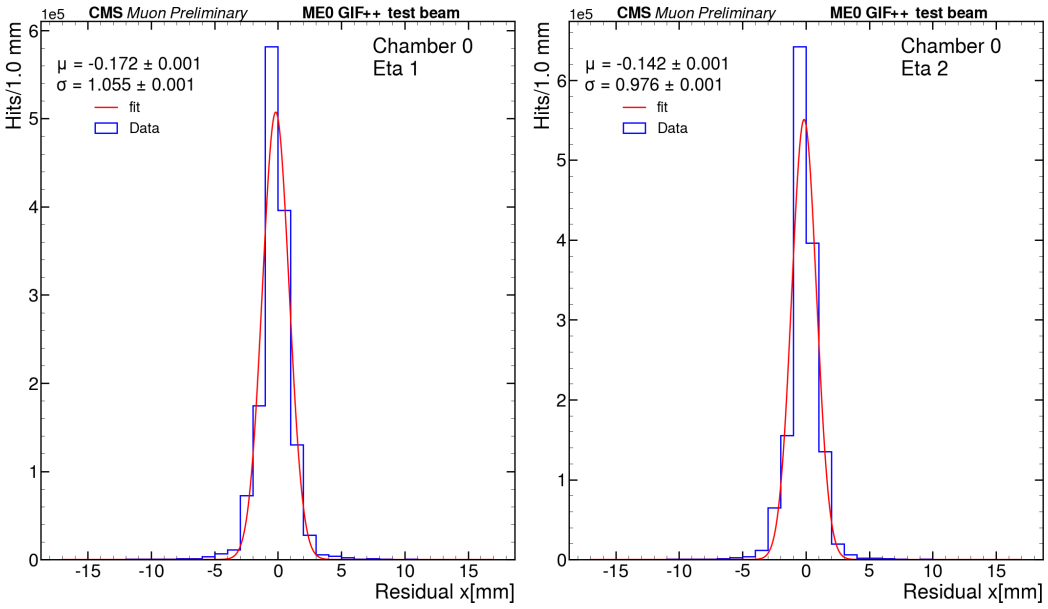

FIGURE 4.14: Distributions of the minima of the residuals per event, for one of the four layers, layer 0, and for eta 1 and 2. The Gaussian fit is performed and the values of A, μ and σ are displayed.

Next, the *measured efficiency*, as defined in Equation 4.4, can be rewritten in terms of frequentist probability:

$$\epsilon_m = P(A \cup B) = P(A) + P(B) - P(A)P(B) \,. \tag{4.5}$$

The two terms $P(A)$ and $P(B)$ are, respectively, the "true efficiency" ϵ of the detector and the "background contamination", b. The latter can be calculated as the number of events with at least one hit in the sidebands between two cuts x_c and x_s, appropriately rescaled to the area of the acceptance region:

$$b = \frac{x_c - x_0}{x_s - x_c} \frac{N\{hits \mid x_c < |x_{prop} - x_{rec}| < x_s\}}{N\{hits\}} \,. \tag{4.6}$$

where x_s is an arbitrary cut on the residuals used in the evaluation of the sidebands. By inverting the formula,

$$\epsilon = \frac{\epsilon_m - b}{1 - b} \,. \tag{4.7}$$

4.6 Results and discussion

4.6.1 HV scan

The detector efficiency has been measured in a run with source off at increasing values of the detector equivalent divider current, from 640 µA to 700 µA, in order to determine the detector's best working point. The procedure performed to compute the efficiency is the same as described in Section 4.5.3. Figure 4.16 shows the efficiency as a function of the HV. The efficiency reaches its plateau of 98% at an HV point corresponding to 680 µA of equivalent divider current.

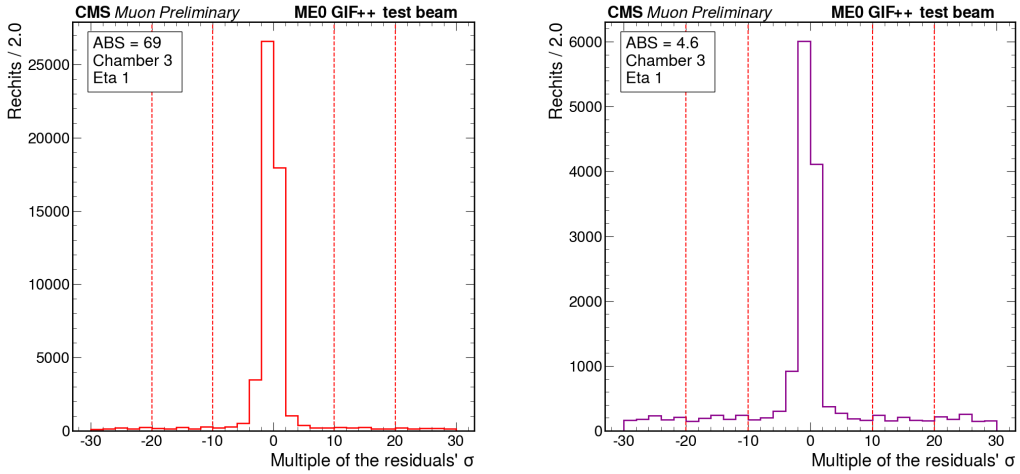

(A) (B)

FIGURE 4.15: (A) Distributions of the residuals for an attenuation factor of 69, (B) Distributions of the residuals for an attenuation factor of 4.6. In both plots, the dashed line represents the borders of the sidebands used to determine the fraction of background hits.

4.6.2 Efficiency measurement

Figure 4.17 shows the efficiency as a function of the cut over the residuals for one of the four chambers of the stack. As apparent, the efficiency plateaus when the multiple that defines the cut gets larger than 4, approximately. Hence, M=5 seems a reasonable choice to evaluate the associated efficiency. Due to radiative losses (e.g. delta-electrons) the tails of the residuals are not Gaussian but can be rather described by a crystal ball function. Therefore, a usual 3σ cut does not cover the typical 99.7% of events expected for a normal distribution. In Table 4.2 the values of the efficiency at 5σ for all the chambers are listed.

ϵ_m **at** 5σ	chamber 0	chamber 1	chamber 2	chamber 3
eta partition 1	0.981	0.973	0.979	0.965
eta partition 2	0.982	0.971	0.979	0.963

TABLE 4.2: List of the muon reconstruction efficiency at 5 residuals' sigma cut for all the four chambers.

Comparing these results with the ones from previous tests [63], some differences show up. The former shows that the efficiency starts saturating approximately at 98%, while the latter yields as upper limit 95-96%, as a consequence of the chamber HV segmentation. This increase in efficiency can be explained considering that the setup of the aforementioned test beam was provided with an external tracker, thus taking into account also muons passing through the inactive zones of the chamber under test generating the plateau. In contrast, in the test beam under analysis the lack of the external tracker and the precise alignment achieved by the mechanical support make the stack insensitive to most of the muons that pass through the dead zones of the chambers, resulting in a higher, but biased, relative efficiency.
When the GIF++ Cs source attenuation factor is reduced (i.e. the source is "ON"), the background particle rate must be taken into account. According to the procedure described in Section 4.5.3, Figure 4.18 depicts the efficiency as a function of the residual

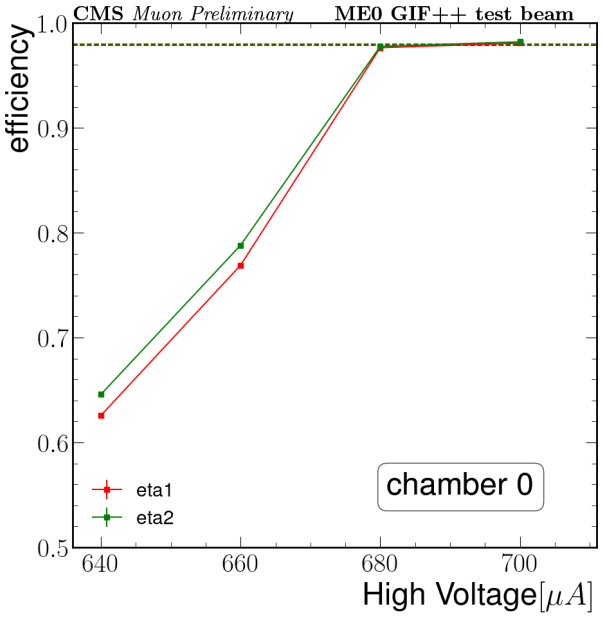

FIGURE 4.16: HV scan for chamber 0, eta 1 and eta 2

cut before (in red) and after (in blue) the background subtraction, showing how the former increases gradually at increasing cut while the latter reaches a plateau as in the no-background case. The background subtraction is larger the higher is the rate of background photons, and, indeed, it is more effective in eta 1, than in eta 2, according to the aforementioned plots. Additionally, the efficiency decreases substantially with increasing rate. The efficiency measured is 78% in eta 1 and 87% in eta 2, that, compared with the 98% of efficiency measured when almost no background hits the same chamber, shows a decrease of respectively 20% and 10%. This drop of the efficiency when the background rate increases should be related to the rate capability of the detector, resulting in a rate capability lower than the one measured in previous tests [63]. Nevertheless, it is noteworthy that in the current test beam the stack is used standalone in the reconstruction, and this feature can strongly affect the efficiency measurements because the stack itself cannot distinguish in any way muon hits from photon hits. In the next section, a deep insight of the limits of the reconstruction procedure will be provided.

4.6.3 Rate capability measurement

Measuring the efficiency at increasing background rate, a drop in efficiency is expected as a consequence of the limits in rate capability imposed by the dead time of the detectors' electronics. The aforementioned trend of efficiency can be exploited to infer the dead time of the detector, according to the model described in Appendix A. The rate capability of all the four ME0 prototype chambers of the stack has been measured evaluating the efficiency for muons of each chamber with the radioactive source activated. The measurement has been repeated for different values of the attenuation factor, i.e. different values of the background rate as measured in Section 4.5.2. The measured efficiency to muons of the ME0 detector as a function of the background rate is shown in Figure 4.19. A significant efficiency drop (∼15%) is observable within the range of background flux.

In the framework of detection techniques, a model has been developed to describe

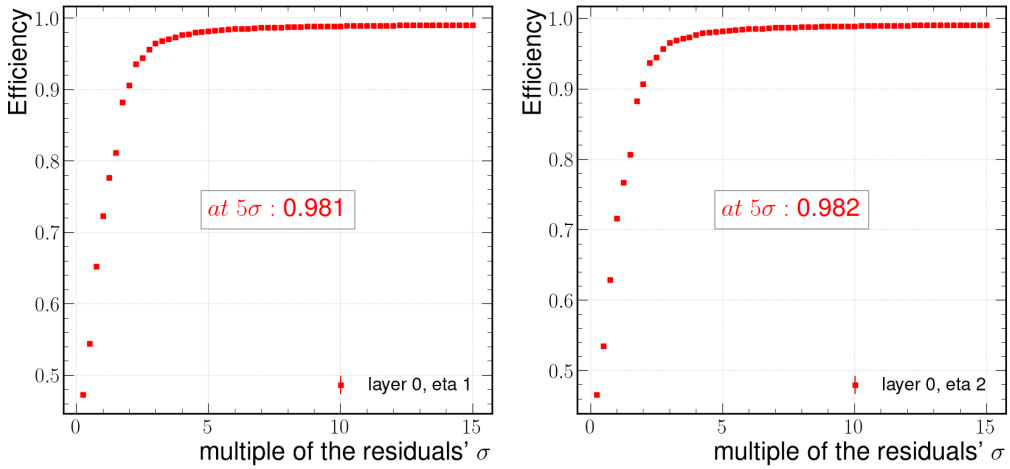

FIGURE 4.17: Muon reconstruction efficiency as a function of the cut on the σ of the residuals' distribution for chamber 0 and eta 1 and 2 for a run without background (source off).

the efficiency of a detector as a function of the rate of impinging background particles in a nonparalyzable[6] response detector [79]. It is described in Appendix A. To quantify the loss of efficiency, a fit is applied to the rate capability curve with the function in Equation A.4, where n is the background rate measured in the rate scans, and the fit parameters ϵ_0 and τ are respectively the efficiency without background and the dead time of the system. The aforementioned plot shows a significant efficiency drop, which corresponds to approximately 1 µs, in terms of dead time. This result differs from the expected one determined from previous tests on ME0 prototypes, according to which a dead time of the order of 100 ns is expected. Once again, this discrepancy is allegedly caused by the lack of an external tracker, which makes the reconstruction procedure less reliable. In fact, the determination of propagated hits over one chamber is determined from the reconstructed hits over the other chambers. Therefore, the segment quality is impacted by the presence of background and may lead to artificially underestimate the efficiency. Then, to improve the measurement of the rate capability of the stack in the GIF++ environment, one needs to employ external trackers[7], that can reconstruct the muon track. Consequently, with the external tracker, muon hits can be distinguished from the photon hits, and the efficiency can be computed more accurately.
However, knowing the profile of the muon beam measured with very low rate of background, some selections can be performed to avoid taking into account faulty tracks. The following reasonable selections can be performed:

- $\chi^2 < 10$, in order to select only tracks successfully reconstructed. Figure 4.20A shows the χ^2 distribution for one chamber, highlighting that badly reconstructed tracks represent a negligible fraction of the total amount of tracks;
- $|slope_{xz}| < 0.1$, that characterizes muon tracks in the muon beam, as observed in its profile measurements (see Section 4.5.1) and emphasized by the plot in

[6] True events that occur during the dead period are lost and assumed to have no effect whatsoever on the behavior of the detector.
[7] A group of chambers with a finer pitch (with respect to the detectors under analysis) and/or far enough from the source (to be irradiated with a lower background rate).

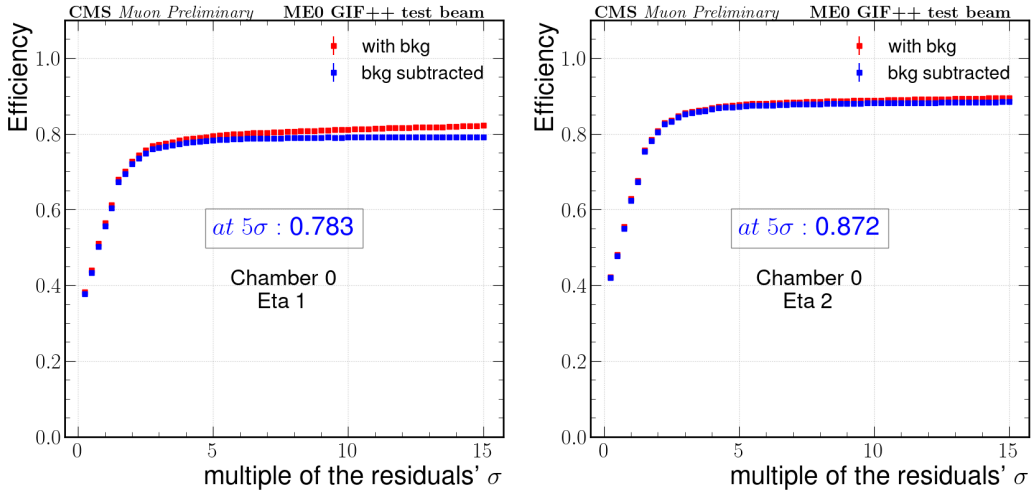

FIGURE 4.18: Muon reconstruction efficiency as a function of the cut on the σ of the residuals' distribution for chamber 0 and eta 1 and 2, in the presence of background (ABS = 4.6). In red, the measurements with background, while in blue the results of the procedure of background rejection. These plots show non-optimal plateau values, but they are obtained without any quality selection on the tracks reconstructed, which are necessary when the stack is used standalone in reconstruction under high rate of background.

Figure 4.20B that shows the comparison of $slope_{xz}$ distributions for a run without background and a run with high background.

- $|slope_{yz}| < 0.01$, which selects only tracks that traversed the same eta partition for all four chambers. The comparison of the distributions without and with background is provided in Figure 4.21;

The number of events with at least one partial track surviving each of these cuts is represented in Figure 4.22 for a high background rate run, showing that, overall, only the 10% of the events is excluded.
Then, the results of such selections are shown in the plot in Figure 4.23. The efficiency drop results to be significantly reduced and in agreement with the expected one.
In Table 4.3 the values of the dead time inferred from the above-mentioned fitting procedure are listed per chamber and per eta partition.

τ(ns)	chamber 0	chamber 1	chamber 2	chamber 3
eta 1	98 ± 10	182 ± 11	126 ± 8	98 ± 8
eta 2	67 ± 11	160 ± 12	97 ± 10	131 ± 12

TABLE 4.3: Dead time inferred from the fit of the detector efficiency as a function of the rate per strip.

Among the possible sources of the efficiency drop observed, one can count:

- the intrinsic detector rate capability;
- the offline reconstruction in high background;
- the read-out electronics.

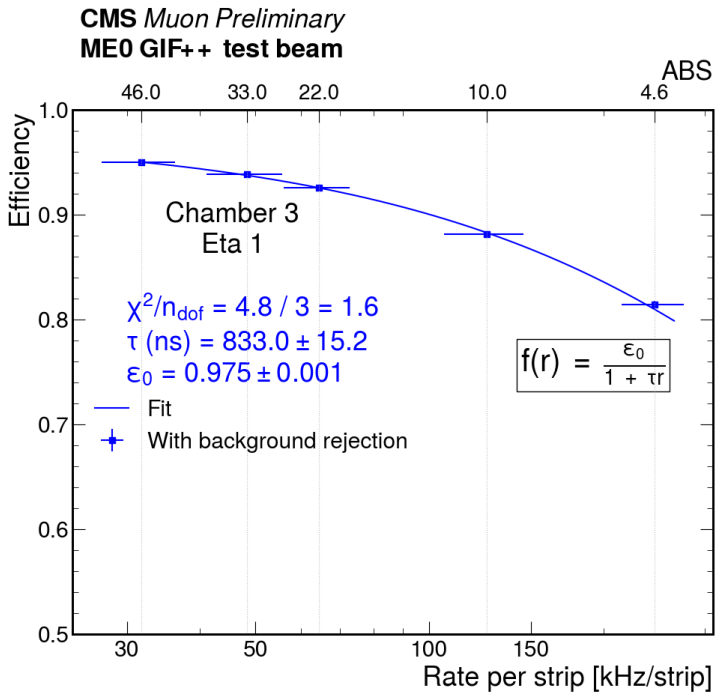

FIGURE 4.19: Preliminary plot (no quality selection applied to the tracks) of the efficiency as a function of the rate per strip, obtained with the background rejection; the line represents the result of the fit with the function in Eq. A.4.

The contribution of the intrinsic rate capability at these rates ($\lesssim$250 kHz/strip) is negligible because the HV drop is lower than $\sim$5 V (see Appendix C). As apparent from the HV scan in Section 4.6.1, the detectors' gain is not affected by the HV drop caused by the background irradiation.
The offline reconstruction using the stack standalone introduces, instead, a decrease in the efficiency caused by the increase of background hits. Although, this effect has been mitigated by introducing quality criteria for selecting only the "good" tracks.
Once selected the "good" tracks, the read-out electronics represent the most significant source for the observed dead time. In particular, among the front-end components, the VFAT3 ASIC is quoted for a rate capability around 2 MHz/strip [68], at least one order of magnitude higher than the rates reached at the GIF++. Nonetheless, previous test beams at GIF++ and tests with x-ray irradiation have already proved that the ME0 detector is not only limited by the gain loss due to the resistive effect but also by the dead time of its front-end electronics. This is confirmed by the results of this test beam.

A Monte Carlo toy has been developed (see Appendix B) to simulate the effect of the VFAT3 dead time, and estimate how the dead time of the single strip and of the whole detector are influenced by the cluster size of muon hits and background hits, confirming that the results obtained in the current test beam align with the rationale that attributes the limited rate capability primarily to the VFAT3 dead time.

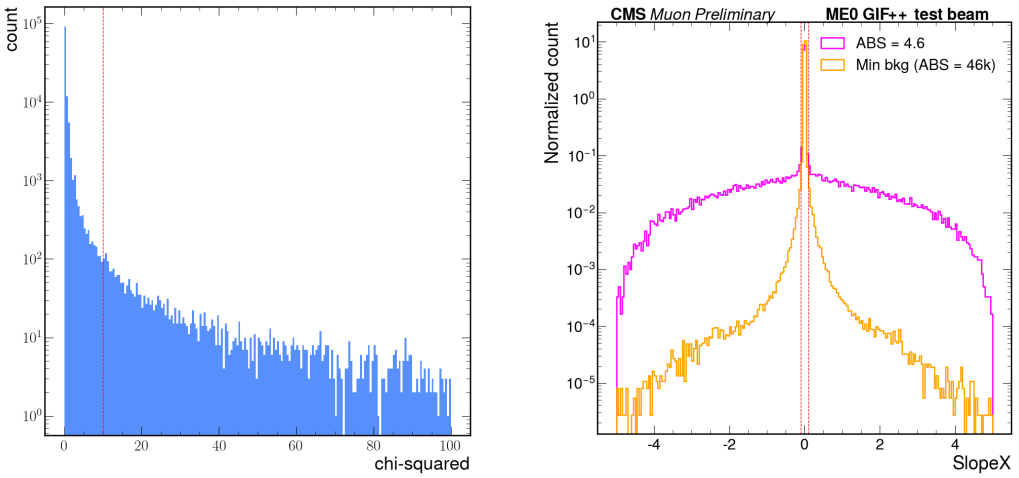

(A) (B)

FIGURE 4.20: (A) Overall χ^2 distribution for a run with ABS = 4.6, the dashed red line corresponds to the value of the cut ($\chi^2 < 10$). (B) Overall distributions of the $slope_{xz}$ for two runs, one with no background and one with ABS = 4.6. The two dashed red lines correspond to the two cuts.

4.7 Offline detector monitoring

Together with the tracking measurement performed to compute the 4-layer stack reconstruction efficiency, the current flowing through each electrode of the four triple-GEM detectors employed has been measured and analyzed. In particular, in the following sections, a measurement of the integrated charge and the discharge rate is presented, aimed at investigating the solidity of previous results. Data from GIF++ monitoring [80] and the HV monitoring board (with a sampling rate of 1 Hz) have been used, in order to know second by second:

- the current flowing through each of the seven electrodes;
- the value of the source status (ON/OFF) and its attenuation factor;

The current flowing through each foil is determined by the number of electron/ion pairs generated by ionizing interactions and moving in the gas. Since the muon rate (5-100 kHz) is far lower than the rate of the source (1-10 MHz), the current generated by muons is negligible, with respect to the current generated by the background photons passing through the whole chambers. This means that the current is linearly proportional to the interacting rate of the background, with a factor that depends on the gain of each gap.
The dependence of the current over the rate is obtained and shown in Figure 4.24. As expected, a linear trend is observed in the central region, while at the extremes of the rate range, the experimental points deviate from the straight line:

- At the lowest values of the rate, the current increases more quickly. This is probably due to the fact that at larger thickness of the absorbers (ABS>10) the probability of Compton scattering increases and the fraction of low energy photons in the flux increases. Since lower energy photons have a higher cross-section of interaction with the detectors' medium, the average number of primary electron/ion pairs increases accordingly.

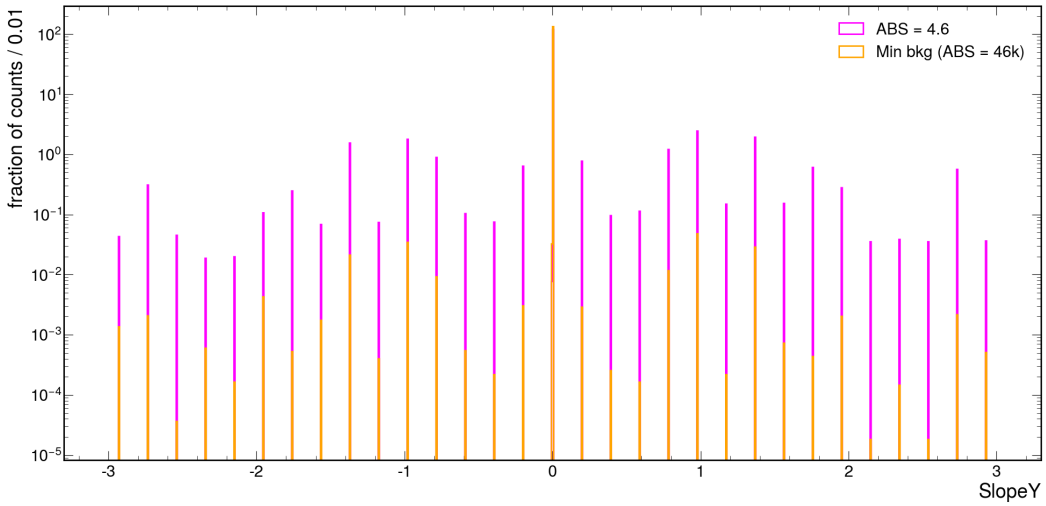

FIGURE 4.21: Overall distributions of the $slope_{yz}$ for two runs, one with no background and one with ABS = 4.6.

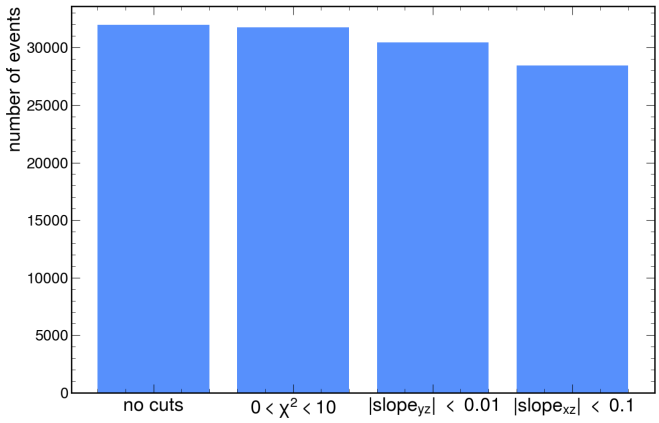

FIGURE 4.22: Number of events surviving each selection.

- At the highest values of the rate, the current starts saturating because of the HV drops through the protection resistors (the detector is under-compensated).

4.7.1 Integrated charge

As the GIF++ is mostly used as an irradiation facility, it is interesting to know the collected charge during the rate tests performed.
Integrating the current over the time of the test beam, the integrated charge for each electrode can be obtained. Particular interest lies in the charge integrated over the bottom electrode of the third GEM foil, which measures a current equal to the one induced on the anode. The overall charge integrated on the whole chamber 3 is shown in Figure 4.25A reaching 4 C. The latter result can be used to compute the average integrated charge per unit of surface per eta partition, since each partition is hit with different rates, as shown in Figure 4.13A. The integrated charge, though, includes also the eta partitions that are not instrumented with the GEBs, whose rate cannot be measured directly but only extrapolated. The rate as a function of eta seems to be well approximated by an error function. Once fitted with the latter, the rates for the

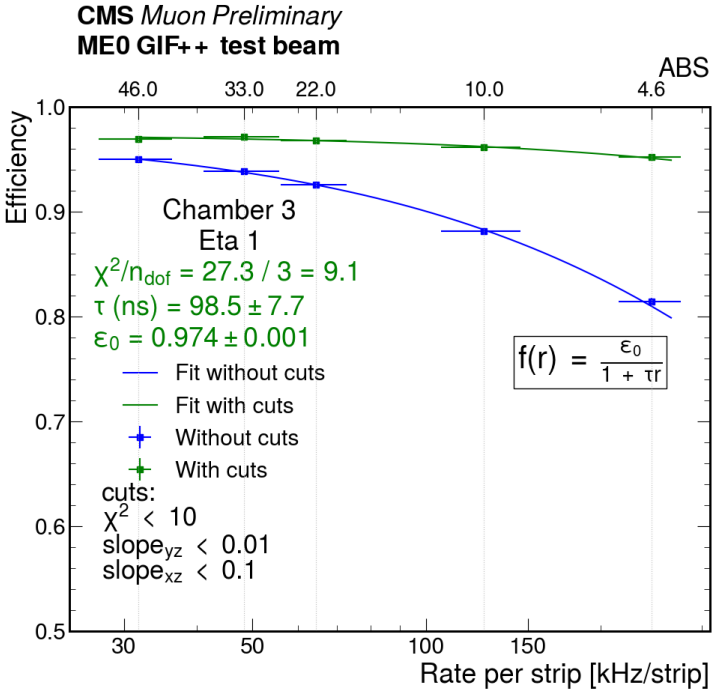

FIGURE 4.23: Efficiency, after the background rejection, as a function of the rate per strip applying the quality cuts (in green) and without applying them (in blue). The lines represent the result of the fit with the function in Eq. A.4. The fitting parameters shown refer to the fit of the efficiency measured after applying the quality cuts on the tracks.

eta partitions from 5 to 8 can be extrapolated. In Figure 4.25B, the aforementioned fit result is shown. Then, the weighted average rate $\bar{r}$ on each chamber, using as weight the irradiated surface, namely the surface of the eta partition (listed in Table 4.1). At this point, for each instrumented eta partition a coefficient can be computed:

$$k_i = \frac{r_i}{\bar{r}}, \; i = 1,2,3,4 \tag{4.8}$$

where r_i is the measured rate on the i^{th} eta partition. Multiplying these coefficients by the average integrated charge per unit surface, an estimate of the average integrated charge per unit surface per eta partition is obtained and shown in Figure 4.26.

As expected, the observed integrated charge ($\sim$2.5 mC cm^{-2}) is much lower than the one expected in CMS for the HL-LHC scenario, which has been estimated to be approximately equal to 8 C cm^{-2}. In fact, usually, aging tests are performed with highly ionizing particles, like α particles, or with x-ray sources with far larger rates. For the purposes of this test beam, it is sufficient to observe that no deviations from the expected behavior are observed at the level of integrated charge reached, as no gain drop has been observed throughout the data taking.

4.7.2 Discharges

The current monitoring allows to count the number of discharges occurring throughout the test beam. In particular, the computation of the average current for the different values of the attenuation factor provides a baseline for the current flowing through each electrode. Thus, a discharge can be defined as a spike that exceeds

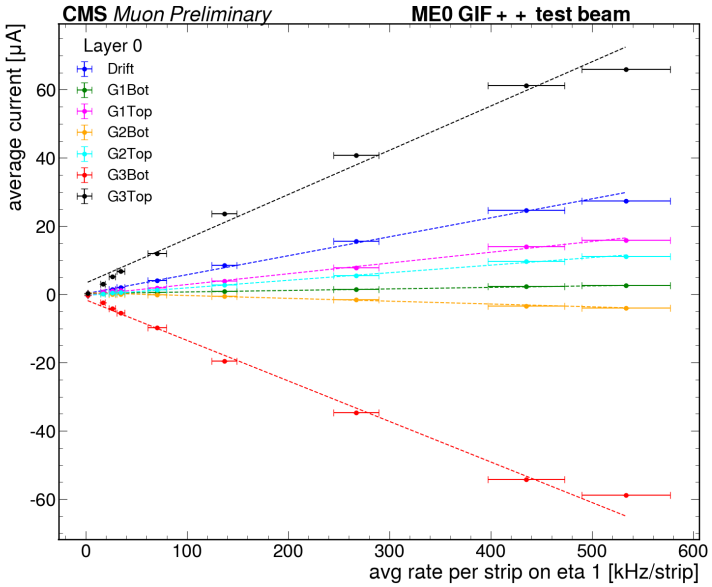

FIGURE 4.24: Average current monitored over each electrode of layer 0 as a function of the average rate per strip on eta partition 1. The dashed line is a linear fit.

the baseline of a certain threshold. Figure 4.27A shows the discharge rate as a function of the attenuation factor when the HV compensation is active. As apparent, no particular trend emerges from these plots, thus, implying that the discharge rate is independent from the attenuation factor, and, then, from the background rate. This result is a consequence of the type of particles constituting the background in the test beam under analysis. The energy spectrum of the γ photons produced by ^{137}Cs source at the GIF++ ranges from 100 to 660 keV, hence their ionizing power is lower than that of the particles that constitute the background in events of pp collisions at CMS, as pointed out in Figure 2.8. As worth comparing, Figure 4.27B shows the trend of discharge rate as a function of the ABS factor when the HV compensation is not applied. No significant differences with respect to the previous case are found, confirming that the HV compensation procedure does not enhance the discharge rate under a high background irradiation.

4.8 Conclusions

The dead time for the chambers is approximately 100-120 ns, in agreement with the previous measurements [63]. At the highest background rate considered (∼200 kHz-/strip), the efficiency drop is 1-2% on each detector. Consequently, the efficiency of the stack is $(95\%)^4 = 81\%$, while the efficiency for a six-layer stack (since at least 5 hits are required to build a segment) is 97%. The measured rate is comparable to the expected one in CMS Phase-2 upgrade in the highest η region of ME0 station (eta partition 8), and the measured efficiency drop is negligible for the physics goals of ME0. Concerning the offline detector monitoring, the results are in agreement with the expectations: the efficiency does not drop after integrating a charge of ∼4 C per chamber, and the discharge rate is constant both without and with HV compensation being applied.

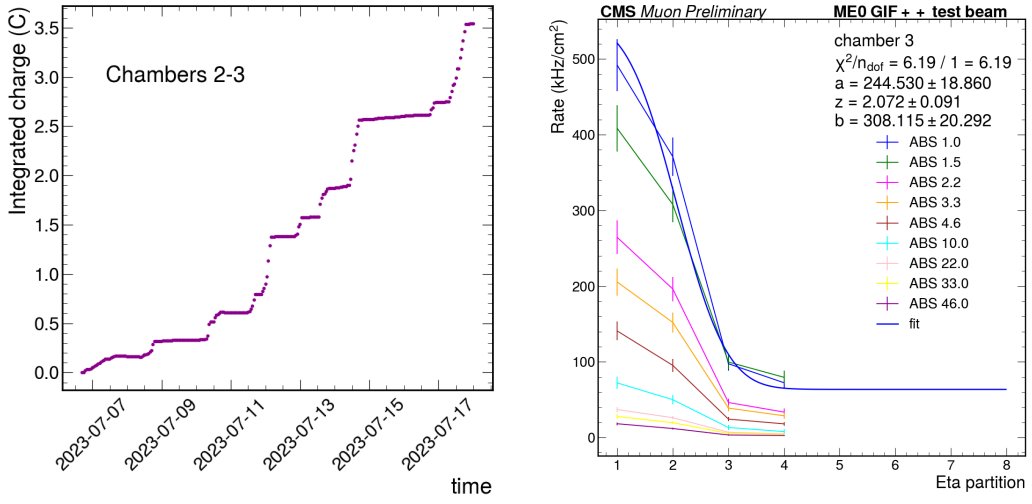

(A) (B)

FIGURE 4.25: (A) Integrated charge over chamber 2 and chamber 3, supplied through the same HV channel. (B) Average rate per unit surface per eta partition for chamber 3. The blue line indicates the result of the fit of experimental data for ABS = 1 with an error function.

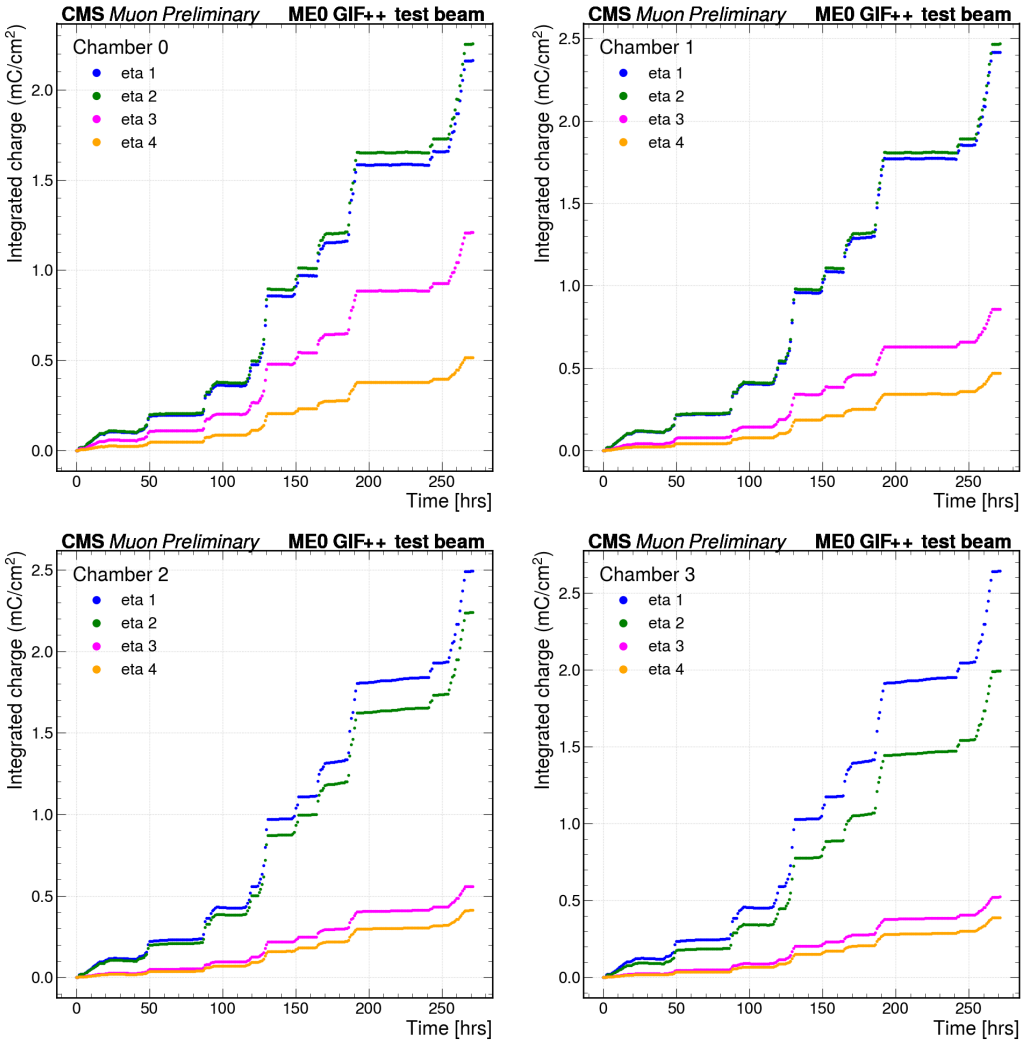

FIGURE 4.26: Average integrated charge per eta for all the four chambers of the stack.

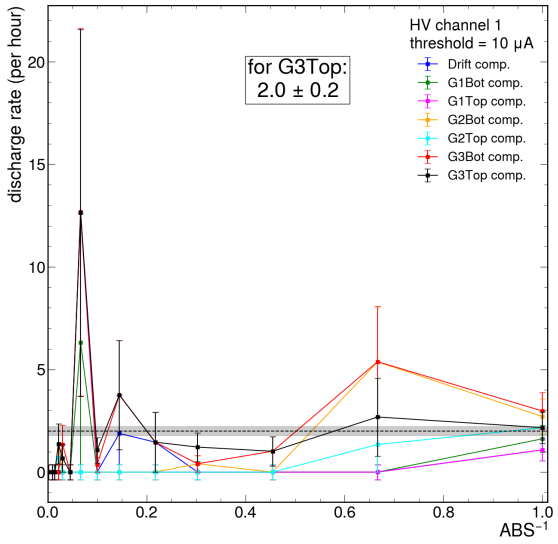

(A)

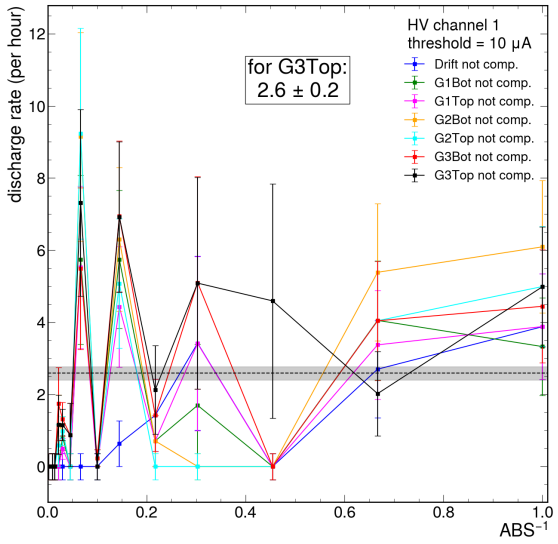

(B)

FIGURE 4.27: Discharge rate as a function of the reciprocal of the attenuation factor respectively with HV compensation (A) and without (B). The black dashed line represents the average of the discharge rate for G3Top electrode (whose values is indicated in the box) and the halo is its standard deviation.

Chapter 5

CMS ME0 performance with MIPs

This chapter describes the spatial and timing performance of a full stack of six ME0 detectors with high energy muons. In particular, in the first part of the chapter the offline alignment procedure developed for the stack will be outlined, while, in the second part, a measurement of the time resolution of the chambers will be described together with the most relevant results obtained. In particular in addition to the time resolution of the single chambers, also a measurement of the ME0 stub timing is performed since the L1 trigger requires segments in the ME0 detector.
The results of the current chapter are based on data taken from a two-week test beam campaign conducted at the SPS H4 beam line in the North Area in April 2024, and from measurements with cosmic rays in laboratory.

5.1 Setup and electronics

The six-layer stack of the ME0 prototype is an extension to six layers of the four-layer stack extensively described in Chapter 4. Hence, it is composed of six ME0 second-generation prototypes held together at a distance of 3.6 cm from each other. Unlike the setup previously mentioned, for the measurements presented in the current chapter, both the narrow and the wide GEBs are instrumented, allowing to readout all the eta partitions of the chambers. The setups employed during the testbeam and for the cosmic stand are identical, with the only difference being the orientation, as displayed in Figure 5.1. Both in the testbeam and in the cosmic stand, the trigger system is made of two $30\times30\,\mathrm{cm}^2$ scintillators, whose coincidence is required.

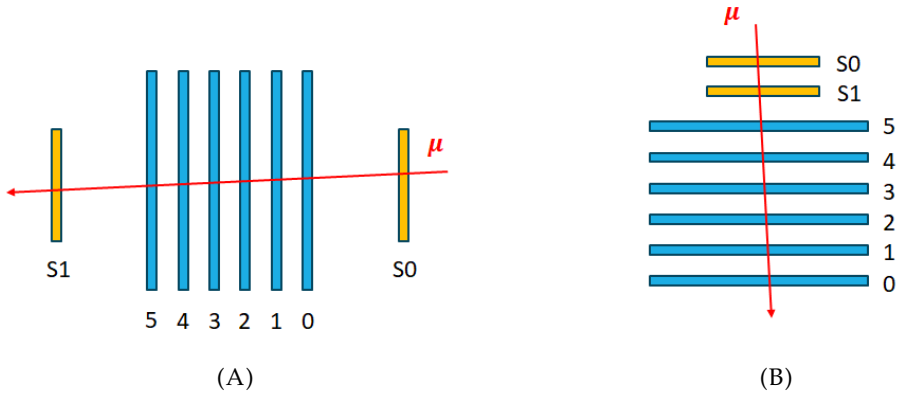

(A) (B)

FIGURE 5.1: Schematics of the setups of, respectively, the H4 test beam (A) and the cosmic stand (B).

5.1.1 Trigger system

The VFAT3 is designed to synchronize output digital signals with the LHC 40 MHz clock. For this reason, to measure the ME0 timing one needs to apply a "trigger conditioning" to select only the events containing muons with arrival time in phase with the electronics clock. In the laboratory setup, the clock is generated by the AMC13 clock, and the conditioning is performed requiring the coincidence of three signals:

- AMC13 clock out (negative front);
- 2 PMT signals, discriminated and set to a narrow time width (∼5 ns).

To reduce the trigger jitter, AMC13 clock is coupled with a dual timer NIM module to last only 5 ns and the time width of the discriminated PMT signals is set to 5 ns, too. The full trigger scheme is shown in Figure 5.2.

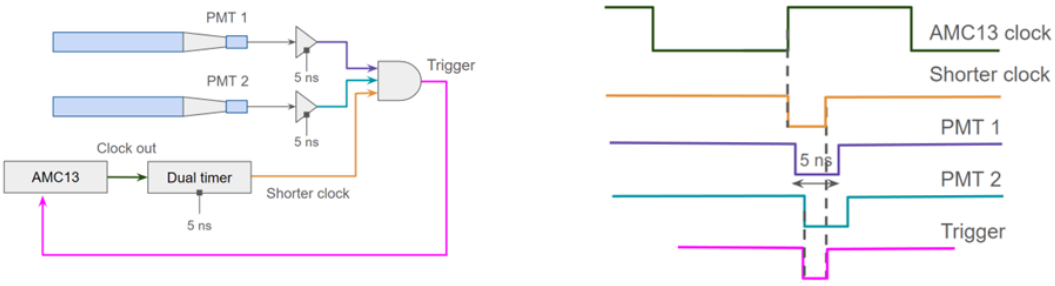

FIGURE 5.2: Full schematic of the trigger conditioning system

This setting ensures a trigger jitter of about 2 ns. Reducing the trigger jitter is important because it influences the time resolution measurement. Indeed the arrival time of a certain hit is evaluated with respect to the trigger reference time. Consequently, the fluctuation in the arrival time takes into account also the fluctuations of the trigger reference, i.e. the trigger jitter:

$$\sigma(t - t_{trigger}) = \sqrt{\sigma(t)^2 + \sigma(t_{trigger})^2}$$

5.2 Offline alignment

The mechanical alignment of the six chambers of the stack is not enough to ensure a precise strip-by-strip alignment among consecutive chambers, with the result of a worse spatial resolution. Therefore, an offline procedure needs to be undertaken in order to improve it. Figure 5.3 shows an example of a misaligned chamber within a stack, and, as evident, the misalignment causes an offset between the reconstructed hits on one chamber and the corresponding propagated hit. The residual distribution can, thus, provide a quantitive evaluation of the stack misalignment. Figure 5.4 shows the residual distribution before applying any alignment. Considering that the strip pitch ranges from 0.8 to 1.2 mm, the misalignment corresponds to less than a strip, but still more than the typical spatial resolution of the detector, i.e. ∼ 230-350 µm. The following iterative procedure to align a set of chambers in a stack can be defined:

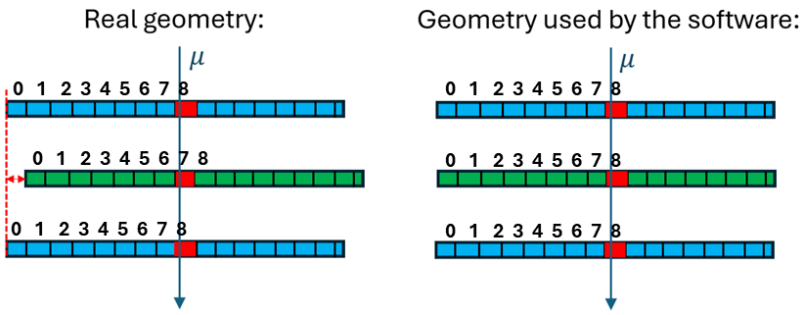

FIGURE 5.3: Partial schematic of the setup, comparing the real stack with one misaligned chamber (in green) and the stack according to the geometry used by the software (in absence of alignment corrections) for the track reconstruction. The numbers refer to the indices of the strip, highlighting that the misalignment generate a displacement between the rechit (in position 7) and the corresponding prophit (in position 8).

0) For the initial geometry, the average offset between reconstructed and propagated hits is given by the mean of the fitting Gaussian:

$$\langle x^0_{rec} - x^0_{prop} \rangle = \mu_0 \, .$$

1) The geometry is updated, redefining $x^0_{rec} \rightarrow x^1_{rec} = x^0_{rec} - \mu_0$.

2) The steps **1)-2)** are repeated for all the chambers in the stack. Chamber by chamber, the iteration updates the geometry. As the propagated hit position depends on the reconstructed hits position, the new propagated hit position is $x^1_{prop} = x^0_{prop} + \delta_1$. Subsequently, a new residuals' distribution is obtained:

$$\langle x^1_{rec} - x^1_{prop} \rangle = -\delta_1 = \mu^1$$

where the new offset, μ_1, is due to the change in the propagated hits positions. Thus, more than one iteration can be needed to minimize it.

i) At the i-th step, repeating the calculations made before:

$$x^i_{rec} = x^0_{rec} - \sum_{j=0}^{i-1} \mu^j \text{ with } \mu^j = \langle x^j_{rec} - x^j_{prop} \rangle .$$

The procedure is iterated until the correction term, μ_i, converges.
Figure 5.5 shows the trend of the correction term during the alignment procedure, as a function of the iteration step. Convergence is reached after only two iterations, confirming that the mechanical support already provides a good initial alignment.

5.3 Time resolution measurements

The role of ME0 in the CMS L1 trigger imposes time resolution requirements to ME0 chambers. In particular, as discussed in Chapter 2, ME0 will be used in CMS to trigger on forward muons at the level-1 in coincidence with other objects. To obtain a BX identification with 99% efficiency, a time resolution better than 4 ns is required. Accordingly, the TDR [6] requires a time resolution of 8-10 ns for a single chamber. The reason for this requirement is the following. When dealing with a telescope of

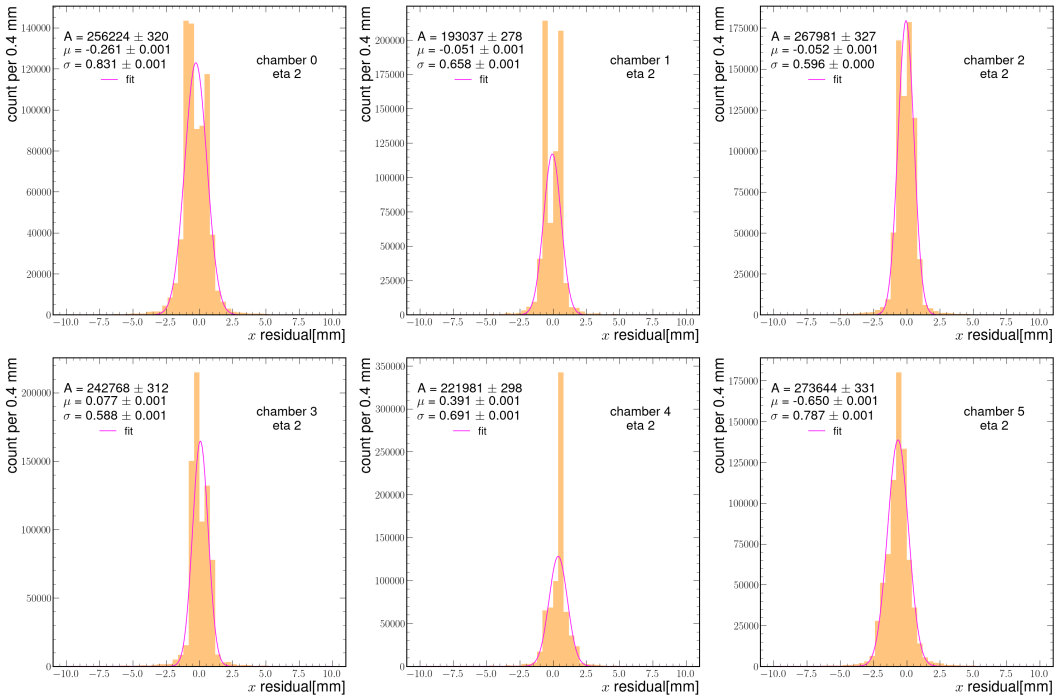

FIGURE 5.4: Residuals distribution before applying alignment procedure for all the chambers taking only the eta partition with the highest number of hits, i.e. eta partition 2.

N detectors, its time resolution goes like $1/\sqrt{N}$ times the time resolution of the single chamber[1], if each chamber has the same time resolution. In order to have a time resolution of 4 ns in the ME0 six-layer stack, a time resolution of ∼9.8 ns is required for each chamber.
To demonstrate this in practice, in the cosmic stand a measurement of the time resolution for the single layers together with the time resolution of the segment has been performed. The time resolution of a detector depends both on the type of detector employed and on the front-end electronics used. The measured time resolution, though, is also affected by the trigger system.
In particular, the GEM analog front-end is represented by the VFAT3, which has two comparators: the Arming (ARM), which is a fixed threshold comparator, and the Zero Crossing (ZCC), which employs CFD logic to improve timing with respect to the ARM. ZCC timing performance are degraded by the noise overlaid with the physics signal. In order to reduce such an effect, the ZCC threshold can be set. The ZCC gets activated only when the signal exceeds the threshold, and when the ARM fires the threshold is removed (set back to 0) and the zero-crossing point is evaluated. The procedure is depicted in Figure 5.6.
The VFAT3 itself does not provide timing information directly, but the firmware can be set to read together consecutive BXs. This firmware function is called multi-BX readout. In the analysis that follows, data taken in the multi-BX readout mode are considered.
In the following sections, the measurements of the time resolution of the digital hits (labeled "digi"), of the reconstructed hits (labeled "rechit") and, finally, of the segments are discussed.

[1] if the time resolution is defined taking as arrival time of the muon the average of the arrival times of the hits in the N chambers.

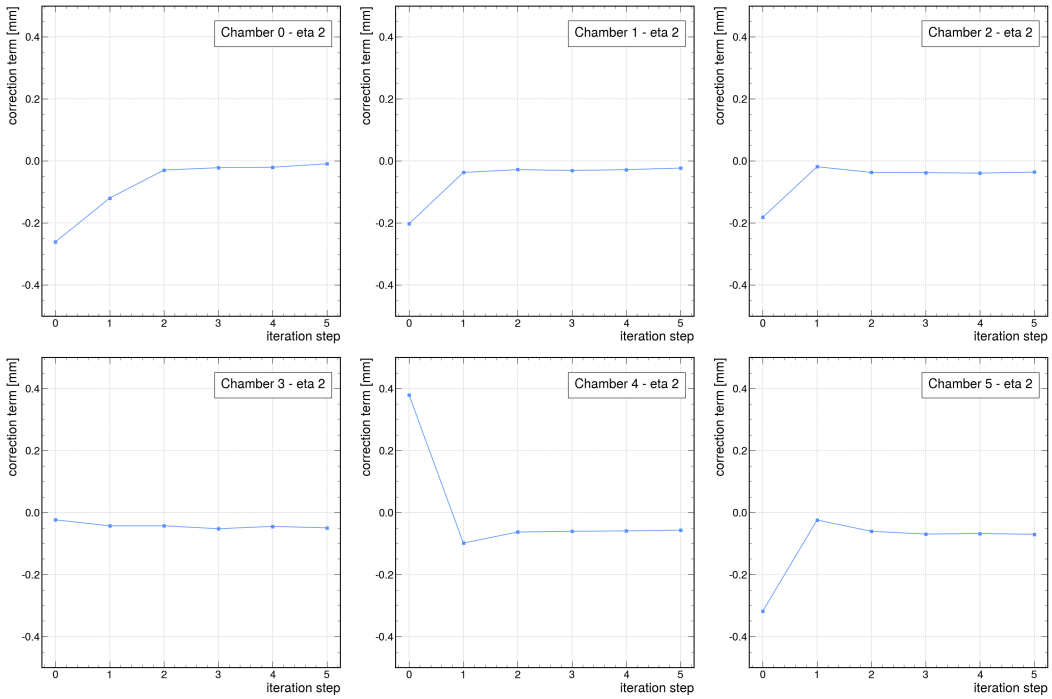

FIGURE 5.5: Trend of the correction term as a function of the iteration step of the alignment procedure for all the chambers of the stack, eta partition 2.

5.3.1 Digi timing

Figure 5.7 shows the distribution of the arrival times of the digital hits. The time resolution determines the spread of the hits among adjacent BXs, and it can be evaluated as the standard deviation of the distribution[2] (The Gaussian fitting, instead, gets less reliable decreasing the time resolution, so it is not applied). The time resolution is between 0.60 BX and 0.80 BX (15 −20 ns), larger than the requirements.
Recent studies have shed light on the major cause affecting GEM chambers' time resolution: the different natures of the signals. Indeed, when a particle traverses the detector, its strips not only see the well-shaped signals induced by the avalanche but also cross-talk signals on the neighboring strips. The latter are typically bipolar signals with null net charge and a negative part peaking earlier than the avalanche signal, generating an earlier VFAT3 response. A comparison of the regular signal with the bipolar signal is shown in Figure 5.8A. Therefore, the digi timing is affected by the presence of bipolar signals generated by crosstalk hits, that generally fire before the regular signal. The plot in Figure 5.8B shows that the central hits (position 0 for odd cluster size, positions -0.5 and 0.5 for even cluster size) within a cluster arrive, on average, before the border hits.
As depicted in the plots in Figure 5.9, when the cluster size is odd (on the right) the central strip (i.e. strip 0) arrives, on average, later with respect to the adjacent strips (for example, +1 and -1); instead, when the cluster size is even (on the left) the two central strips show a similar arrival time distribution.

[2]The uncertainty on the standard deviation is computed with the formula of the variance of sample variance [82].

$$\text{Given } \hat{\mu} = \frac{\sum_{i=1}^{N} X_i}{N} \ , \ \hat{\mu_k} = \frac{\sum_{i=1}^{N} (X_i - \hat{\mu})^k}{N} \ \rightarrow Var(S^2) = \frac{1}{N}(\hat{\mu_4} - \hat{\mu_2}^2) + \mathcal{O}(N^{-2}) \ .$$

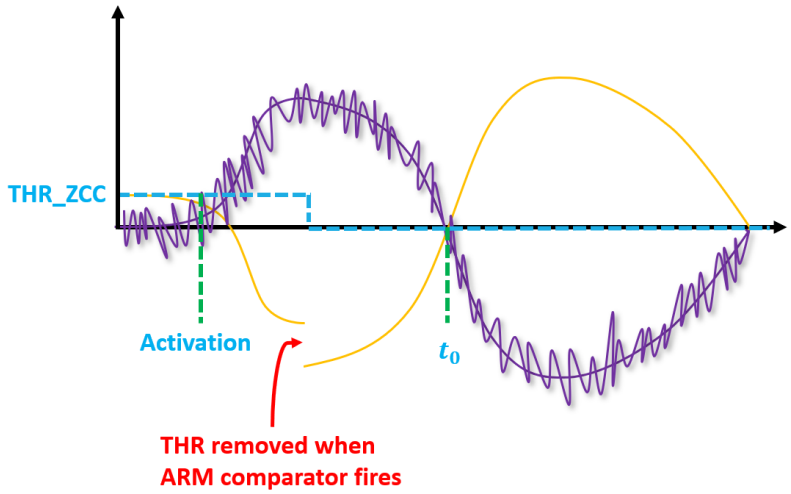

FIGURE 5.6: Schematic showing how the ZCC threshold is applied to the signal. (taken from [81], modified in form)

5.3.2 Rechit timing

In order to reduce the effect of crosstalk signals, clustering must be performed according to the procedure described in Section 4.4; additionally, the arrival time associated with each cluster is the maximum among the arrival times of the strips that compose it. Once reconstructed hits and their timing are computed, the new time distribution is obtained and shown in Figure 5.11A. The influence of crosstalk hits is clear, indeed removing their contribution the time resolution goes down to 11.25 ns, not yet in the required range, but closer to it.
One of the effect degradating the observed time resolution is that the average value of the rechit time may be very different from an integer value, populating two time bins equally (see Figure 5.10A). This effect can be corrected by adjusting the GBT-TX phase, i.e. delaying the clock sent by the GBT to the VFAT3 by a fraction of BX (with a granularity of 1/64 BX[83]); Figure 5.10B shows that the time distribution after this correction is centered on the closest BX.
Finally, it is considered the contribution to the timing due to noise and cross-talk hits separate from the muon cluster. To exclude their contribution, only hits matching with the muon segment reconstructed by the other layers in the stack are taken into account. Matching reconstructed hits are defined according to the definition given in Section 4.5.3. As shown in Figure 5.11B, this further selection significantly improves the time resolution to 10.00±0.25 ns, in agreement with the TDR requirements.

5.3.3 Segment timing

ME0 trigger primitives are multi-layer segments, so another important feature to measure is the time resolution of the segment. Time resolution of the segment is improved with respect to the single chamber by statistics. In fact, given a stub made from the hits on N_{layers} layers, the average arrival time will be distributed with a standard deviation:

$$\sigma_{stub} = \frac{\sigma_{layer}}{\sqrt{N_{layers}}} .$$

Taking into account all the possible combinations of the six chambers, the time resolution of the stub has been computed and it is shown in Figure 5.12, showing a trend

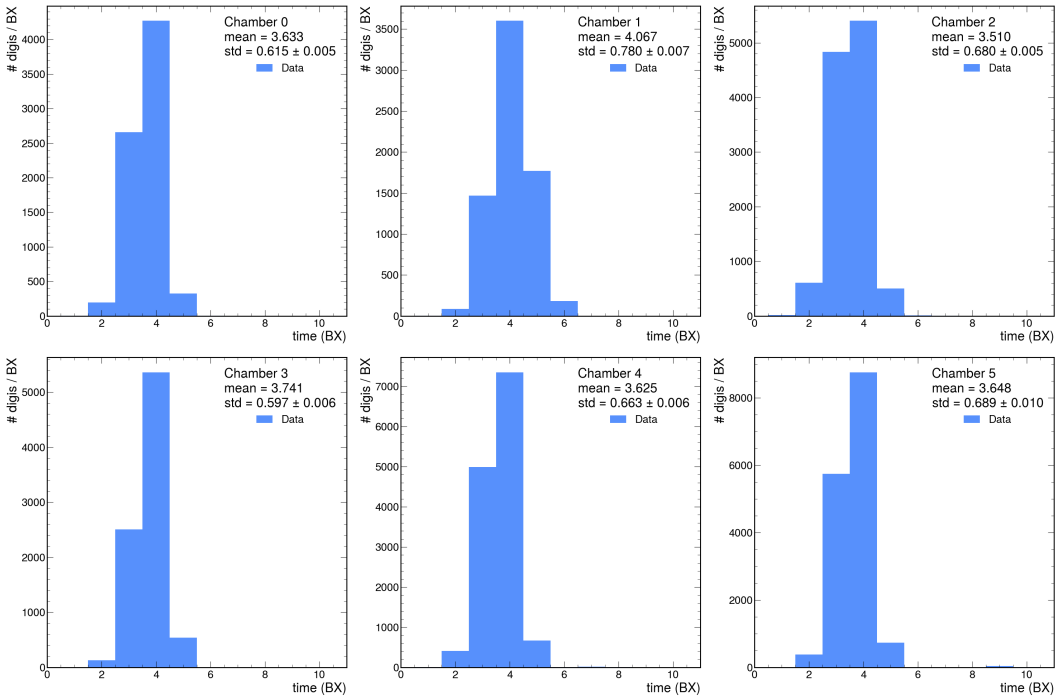

FIGURE 5.7: Distribution of the arrival time of the digital hits in units of bunch-crossings. The fitting with a Gaussian function has been performed.

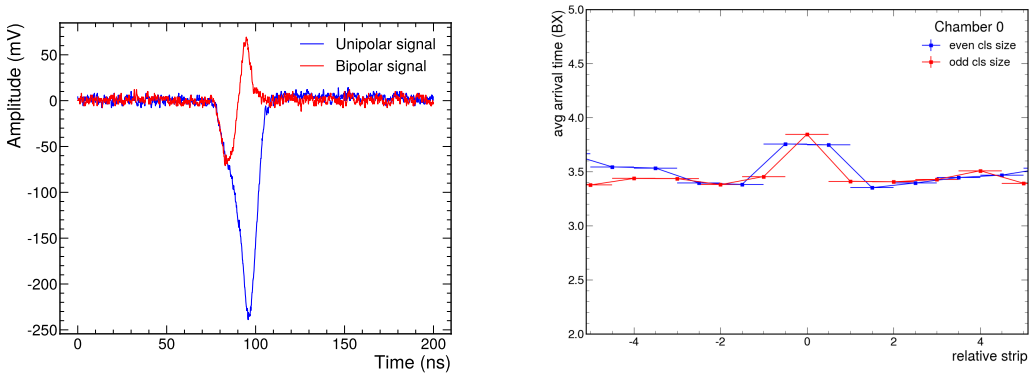

(A) (B)

FIGURE 5.8: (A) Example of a regular signal compared to a bipolar signal obtained with cosmic rays read from one strip of a ME0 detector using a linear amplifier. (from [81]) (B) Arrival time as a function of the relative position of the digi inside the cluster, distinguishing odd cluster size (in red) from even cluster size (in blue).

that falls off like $1/\sqrt{N_{layers}}$. As evident from the width of the error bars, there is one chamber (chamber 1 in Figure 5.7) with a worse timing resolution that affects the timing resolution of the stub.
Nevertheless, the average of the arrival times of the hits is not the only way to determine the arrival time of the track. A possible alternative consists of taking the median of the arrival times. In Figure 5.13, the distributions of the arrival times for the six-layer segment (obtained respectively with the average, Figure 5.13A, and with the median, Figure 5.13B) are shown. Accordingly, the time resolution of the segment goes down to:

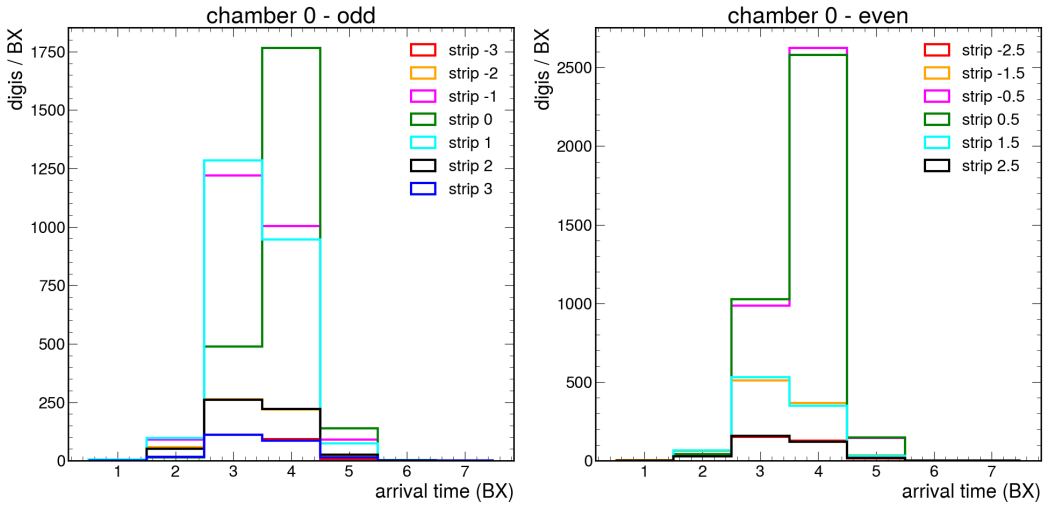

FIGURE 5.9: Distribution of the arrival time of the digital hits for the different strips (expressed in relative positions) within a cluster.

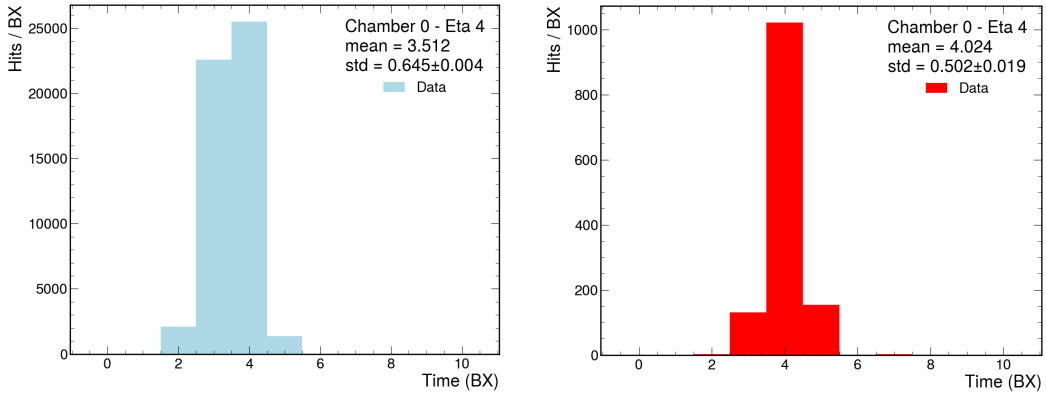

(A) (B)

FIGURE 5.10: Time distribution for the reconstructed hits in chamber 0 eta 4 for two different runs: (A) before the GBT-TX phase adjustment (B) after the GBT-TX phase adjustment.

- using the average: 0.21 ± 0.007 BX $= 5.25 \pm 0.18$ ns, with a probability of the 0.3% of pre-fire, 2.4% of post-fire and ∼97% of BX identification;
- using the median: 0.15 ± 0.02 BX $= 3.75 \pm 0.5$ ns, with a negligible probability of pre-fire (<0.001%), 2.9% of post-fire and ∼97% of BX identification.

5.4 Conclusions

In conclusion, in the first part of the current chapter a procedure for the alignment of the stack has been described. Only the transversal alignment has been performed. The procedure for the angular alignment still needs to be developed, because it needs both an extended beam (e.g. cosmic rays) and an extended trigger able to cover the whole stack.
Concerning the measurement of the time resolution, the results achieved for the single layers (σ_t = 10.00 ±0.25 ns) are in agreement with the TDR. Considering six-layer

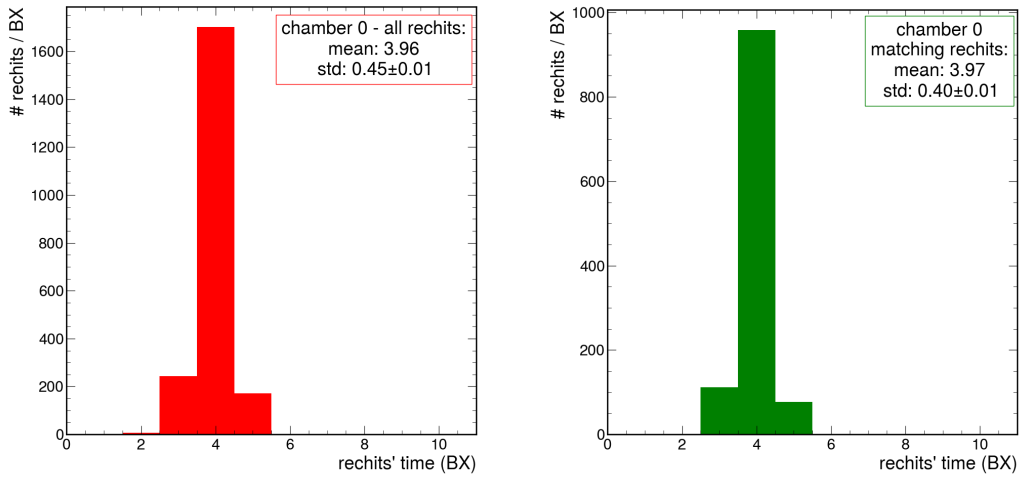

(A) (B)

FIGURE 5.11: (A) Time distribution for all the reconstructed hits. (B) Time distribution for the muon matching reconstructed hits.

segments, the time resolution goes down to either 5.25±0.18 ns (using the average) or 3.75±0.5 ns (using the median). In both cases, the BX identification corresponds to the ∼97%.

However, the next step to validate the stack performance consists of measuring the time resolution of the stack in presence of background. Background hits contaminate the clusters, affecting the time resolution of the chambers.

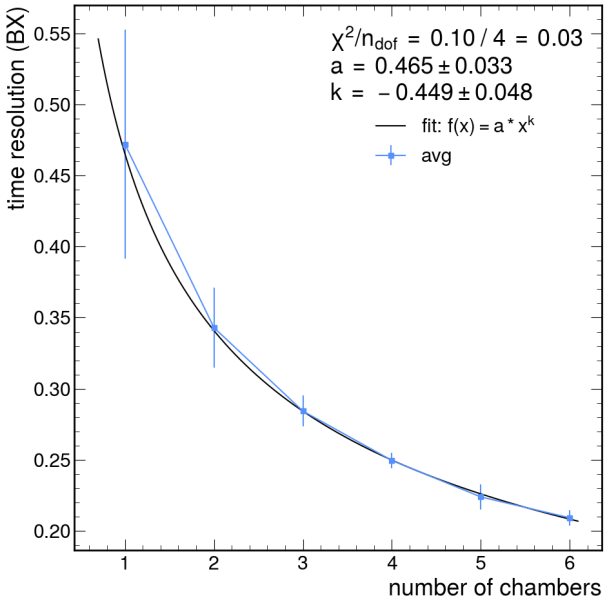

FIGURE 5.12: Average time resolution of the track as a function of the number of chambers used to reconstruct it.

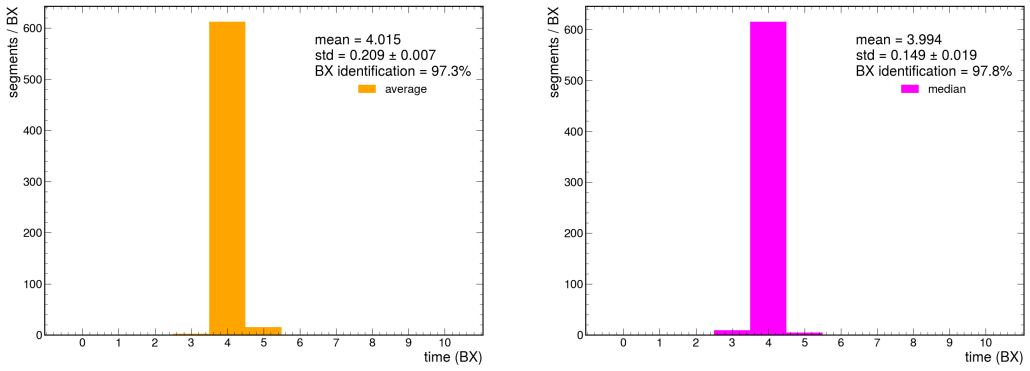

(A) (B)

FIGURE 5.13: (A) Distribution of the arrival times of the six-layer segments computed with the average of the matching rechit arrival times. (B) Distribution of the arrival times of the six-layer segments computed with the median of the matching rechit arrival times.

Conclusion

The work presented in this thesis is aimed at validating the performance of the prototype of the CMS ME0 detector. In particular, the first prototype consisted of four (out of the six foreseen in the final design) stacked triple-GEM chambers, instrumented only with the wide GEB. Data have been collected with the prototype standalone during a test beam campaign at the CERN GIF++ (in July 2023) and have been subsequently analyzed, in order to validate the performance of the prototype in the facility high-rate environment. With a background particle rate up to about 200 kHz/strip, the efficiency of the four chambers in detecting muons has been measured. The results showed an efficiency drop of ∼1-2%, confirming the results obtained in the previous tests performed on the single ME0 triple-GEM chamber [63]. The dead time measured is compatible with the dead time of the VFAT3 chips, used for the frontend electronics, if one takes into account the different cluster sizes of muon (∼3) and background hits (∼1). The average dead time measured is approximately 120 ns, ranging from 67 to 182 ns for the single chambers and partitions.
The analysis could be improved if an external tracker was employed. In fact, the lack of external trackers caused:

- a bias in the efficiency measurement with low background due to the overlapping of the chambers' dead areas.
- an enhancement of the efficiency drop, caused by the fact that the track reconstruction algorithm could not distinguish muon hits from background hits. This limit has been overcome by applying quality cuts on the tracks, after an analysis of the slope of the muon tracks in absence of background.

In April 2024, the final prototype of the six-layered ME0 stack fully GEB-instrumented has been completed. Accordingly, the first validation tests have been carried out both with cosmic rates and in a test beam at the H4 beamline. In this thesis, a procedure for the offline alignment of the chambers within the stack has been successfully developed, using data from the test beam campaign abovementioned. Additionally, using cosmic rays, a measurement of the time resolution of the single chambers and of the entire stack has been carried out. To measure the detector time resolution, the reconstruction of readout clusters was modified to take into account the presence of bipolar signals due to induction between adjacent strips. The results obtained have shown a time resolution of the single chambers down to 10 ns, and a time resolution for a six-hit track of approximately 5.25 ns. In CMS ME0 segments will be mostly (∼97%) made by 5 or 6 hits. These results are in agreement with the requirement of the CMS Phase-2 upgrade TDR, and are compatible with an excellent BX identification of 97%. However, the measurement still needs to be performed in a high-rate background environment to correctly validate the performance of the ME0 stack.

Appendix A

Model for dead time behavior

In nearly all detector systems, there will be a minimum amount of time that must separate two events so that they are both recorded. The limiting time may be set by processes in the detector itself, and in other cases the limit may arise in the associated electronics. In the GEM detector, the dead time is related to the dead time of the comparator. The the detector under analysis works in non-paralyzable mode, the corresponding model of dead time behavior is taken into account [79]. The response of a detector system can be described in terms of the following variables:

- n = true interaction rate;
- m = recorded count rate;
- τ = system dead time.

Assuming that the counting time is long, both n and m can be regarded as average rates. The goal is to obtain an expression for the true interaction rate n as a function of the measured rate m and the system dead time τ. In the non-paralyzable case, the fraction of all time that the detector is dead is given simply by the product $m\tau$. Therefore, the rate at which true events are lost is simply $nm\tau$. But, since $n - m$ is another expression for the rate of losses,

$$n - m = nm\tau \tag{A.1}$$

solving for m, the following formula is obtained:

$$m = \frac{n}{1 + n\tau} \, . \tag{A.2}$$

Figure A.1 shows the function describing the measured rate, m, as a function of the true rate, n, for different values of the dead time, τ. Defining the efficiency $\epsilon = m/n$ as the ratio between the average observed rate of events and the average input rate, an expression of the efficiency as a function of the observed rate and the detector's dead time can be written as follows:

$$\epsilon = \frac{1}{1 + n\tau} \, . \tag{A.3}$$

Given that the detector has an intrinsic efficiency ϵ_0<1, the absolute efficiency becomes:

$$\epsilon = \frac{\epsilon_0}{1 + n\tau} \, . \tag{A.4}$$

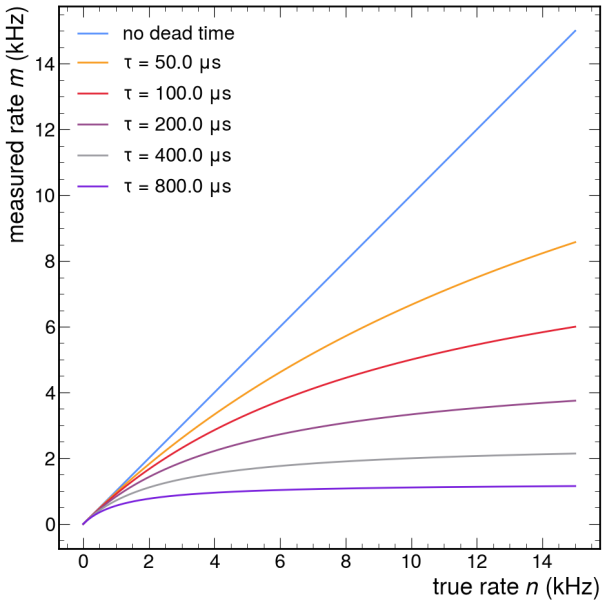

FIGURE A.1: Variation of the observed rate, m, as a function of the true rate, n, for the model of dead time losses in a nonparalyzable-response detector.

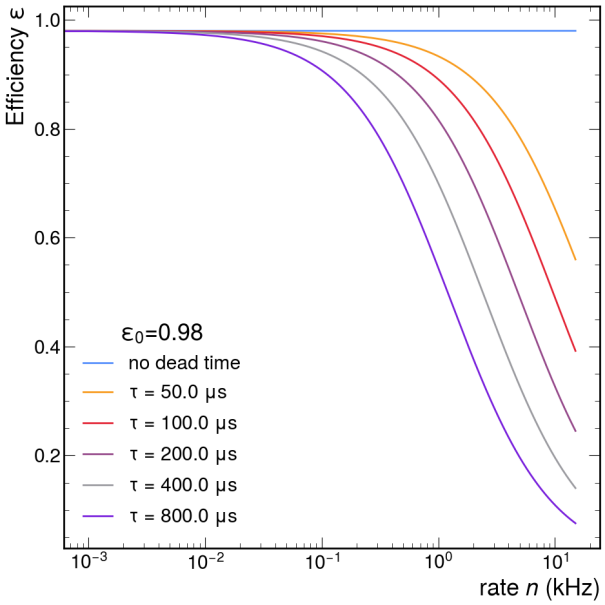

FIGURE A.2: Measured efficiency as a function of the true rate for different values of the dead time and a nominal efficiency ϵ_0 of 0.98.

Appendix B

Monte Carlo toy for dead time

The GIF++ test beam results showed that the ME0 detector operated in an intense background environment has an efficiency for muons compatible with a dead time in a range from 60 ns to 170 ns depending on the chamber and eta partition, as shown in Table 4.3; simulations and measurements with x-rays have shown that the VFAT3 dead time, depending on the input charge, is comprised between 400 and 1000 ns. A numerical simulation has been developed to understand how the detector dead time can be related to the dead time of a single readout electronics channel by keeping into account the effect of the cluster size both of the muon hits and of the background hits. The toy monte carlo works by generating events hitting a detector surface made of 384 rectangular parallel strips (equal to the number of strips per η partition in an ME0 detector) uniformly in space. This is not exactly the shape of the ME0 GEM chamber partitions, that are trapezoidal, but it is reasonable to make such an approximation. In addition, the events generated are distinguished in two classes:

- "muon" events, which occur with a cluster rate of $r_\mu = 3$ kHz per strip and are the one we are interested in detecting;
- "background" events, which occur with a much larger cluster rate of $r_{bkg} = 250$ kHz per strip.

The area of the detector does not matter in the simulation. Each event contains one hit; the hits are generated by sampling a random time from a Poisson distribution with mean $\tau_{\mu/bkg} = (r_{\mu/bkg} \times 384)^{-1}$, depending on whether it is a "muon" event or a "background" one, and the central strip hit is sampled from a uniform distribution. In order to take into account the different cluster sizes measured for "background" events and "muon" events (shown, respectively, in Figures 4.13B and 4.9A), for each event, the corresponding hit is digitized by assuming a cluster size that is sampled from two different Poissonian distributions of average respectively 3 for muons and 1 for background. Since the null values sampled are discarded, the actual average of the cluster size distribution is larger than the one used for generation, and the cluster size distributions obtained are shown in Figure B.1.
Then, a dead time $t_0 = 400$ ns is applied through the following procedure:

- for each strip, a "muon" event is marked as "not detected by the strip" if its distance in time from the previous hit, either "muon" or "background", occurring on the same strip is lower than t_0;
- an event is marked as "not detected by the detector" if it is not detected by any of the strips it hits.

After applying the selection, the following two variables are calculated:

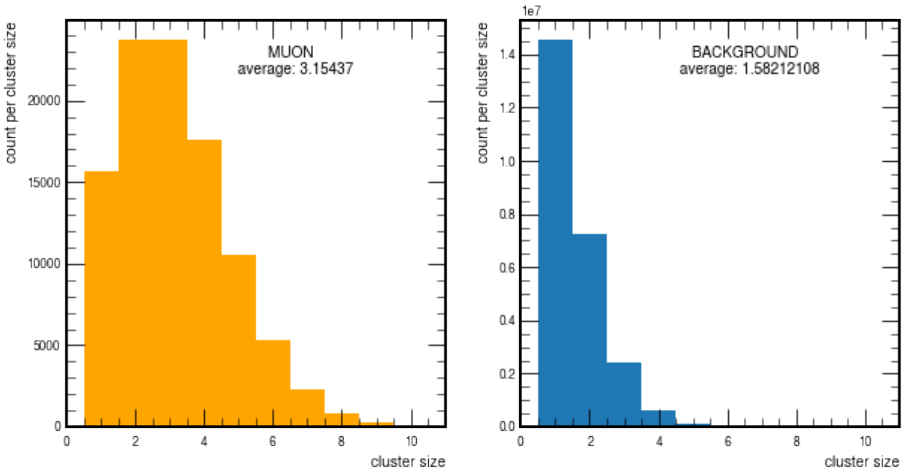

FIGURE B.1: Cluster size distribution of muon hits and background hits generated from poissonian distributions.

- the efficiency of the strip is defined as the ratio between the number of "muon" events detected by the strip and the number of "muon" events containing a hit on the strip;
- the efficiency of the detector is defined as the ratio between the number of "muon" events detected by the detector and the total number of "muon" events.

The procedure above defined is repeated for different input rates per strip. Figure B.2 shows the trend of the strip efficiency (averaged among all the strips) and the detector efficiency as a function of the effective strip rate. The trends are fitted by the function

$$\frac{1}{1+f\tau}$$

to determine the measured "strip" and "detector" dead times. The calculated strip dead time of 431.9 ns is close to the input dead time of 400 ns, while the detector dead time is much lower, equal to 125.7 ns. This explains how the dead time of the ME0 detectors measured in GIF++ test beams, is compatible with a dead time of 400 ns per strip of the VFAT3 chip.

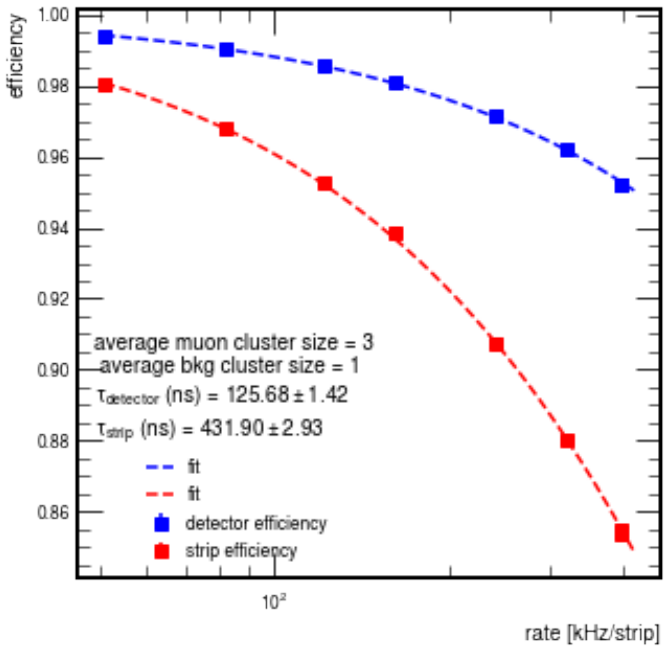

FIGURE B.2: Detector efficiency and strip efficiency as a function of the effective strip rate.

Appendix C

High Voltage compensation at GIF++ test beam

When GEM detectors are working in a high background rate environment, like at the GIF++, the multitude of electrons moving through the electrodes can generate a non-negligible amount of current flowing through the protection resistors. Consequently, it causes a drop of the voltage applied to the foils, and, finally, a decrease of the gain, as shown in Figure C.1.

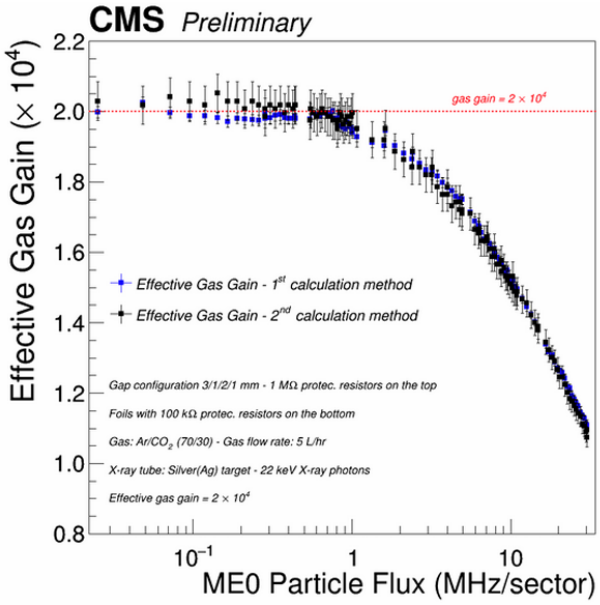

FIGURE C.1: Gain drop of the irradiated prototype comparing the "direct" gain measurement (in black) and the "ohmic" gain measurement (in blue). (from [63])

Therefore, among the operations needed to utilize triple-GEM detectors in GIF++ test beam, the compensation of the HV drop has a primary role, and the procedure performed will be discussed here. The flowchart in Figure C.2 displays the procedure used for the HV compensation[63] of one of the 7 electrodes of a triple-GEM detector and it is applied identically to each of them. The gain recovery is performed iteratively, and the steps are the following:

- at step 0, the voltage applied to each electrode is $V^0_{SET} = V_{NOM}$, where V_{NOM} is the nominal value set via the Multi-Channel HV supply (MC). The current monitored through the foil, I^0_{MON}, and the corresponding voltage drop is computed as $\Delta V = I^0_{MON} \times R_{PROT}$. The effective voltage applied is: $V^0_{EFF} = V^0_{SET} - I^0_{MON} \times R_{PROT}$;

- at each subsequent i-th step, the voltage applied to the electrode is set to $V^i_{SET} = V^{i-1}_{SET} + I^{i-1}_{MON} \times R_{PROT}$;
- the compensation is completed when $|V^i_{EFF} - V_{NOM}| < V_{th}$, namely the effective voltage ($V^i_{EFF} = V^i_{SET} - I^i_{MON} \times R_{PROT}$) on each electrode is compatible with the nominal one within a small tolerance, for example 1 V.

Figure C.3A shows the iterative trend of the voltage corrections on each electrode; the compensation converges almost immediately for all electrodes except for the bottom of the third foil, the one sustaining the largest amount of current, which takes 5 to 6 iterations to converge at the largest fluxes tested. Figure C.3B shows the rate capability curve overlapping with the recovered gain curve after voltage compensation, together with the nominal gain at which the detector has to be powered to operate it at an effective gain of 2×10^4 for each value of the background rate.
Due to a mistake, during the current test beam, the compensation algorithm has been developed considering HV filters of 50 kΩ, while, from measurements after the test beam, it has been found that their resistance was equal to 320 kΩ. This implies that, even when the compensation is active, the detector is under-compensated; indeed, referring to Figure 3.2, the voltage drop is computed as:

$$\Delta V = I_{MONDET} \times (\frac{R_{seg}}{N_{seg}} + R_{filter}) \tag{C.1}$$

where R_{seg} is the protection resistance of one GEM foil sector (there are N_{seg}=40 HV segments in a ME0 GEM foil) and R_{filter} is the resistance of the corresponding HV filter.
For the purpose of evaluating the effects, one should compute the expected voltage drop ΔV without compensation and evaluate the efficiency measured at the voltage $V_{NOM} - \Delta V$ (from the HV scan in Figure 4.16). The reconstruction algorithm described in Section 4.4 works successfully for attenuation factors above 4.6, hence the voltage drop should be evaluated for $ABS = 4.6$, where it reaches its highest value. As the value of the monitored current measured (as shown later in Figure 4.24) for the third GEM foil bottom electrode (R_{seg} = 100 kΩ) is around 10-20 µA (depending on the single chamber irradiation), the voltage drop ΔV, after compensation, is approximately:

$$I_{MONDET} \times (R^{true}_{filter} - R^{algorithm}_{filter}) = 2 - 6 \ V \ .$$

For these values of the voltage drop the effective HV point $V_{NOM} - \Delta V$ is still larger than 680 µA. Consequently, since the efficiency of the detector, as evident from the HV scan, is at the plateau from 680 µA (see Section 4.6.1), the partial "under-compensation" of the high voltage does not affect significantly the results of the rate capability analysis.

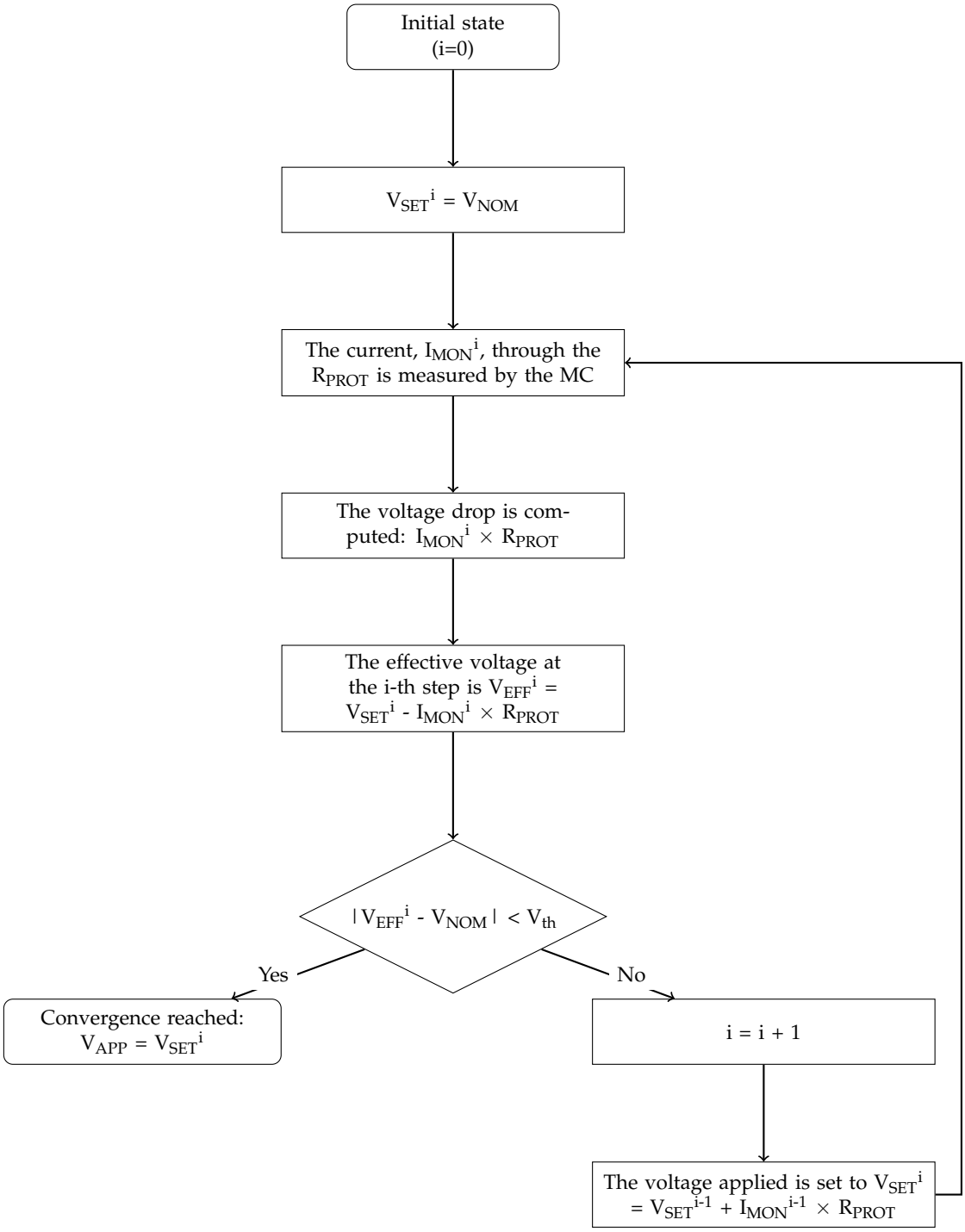

FIGURE C.2: Flowchart of the HV compensation algorithm.

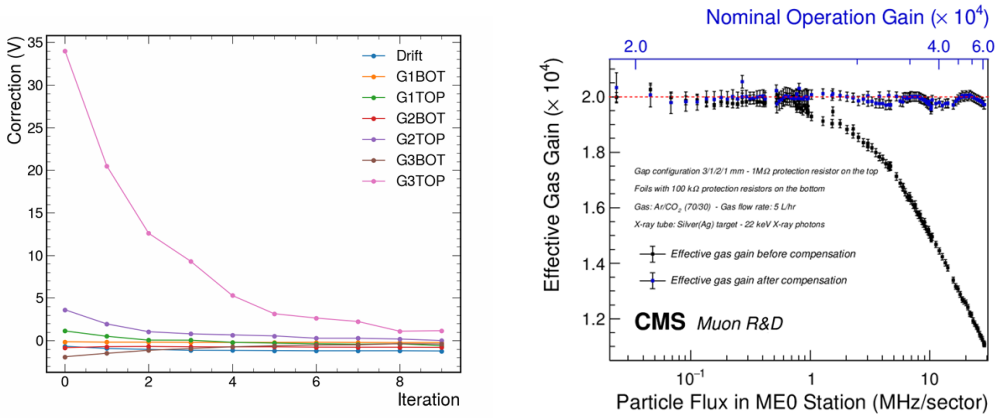

(A) (B)

FIGURE C.3: (A) Iterative corrections applied in each electrode during the voltage compensation procedure. (from [63]) (B) Recovered gain of the GEM detector over the tested rate region. The top axis shows the nominal gain (as per gain calibration curve) at which the detector has to be powered to operate it at an effective gain of 2×10^4 under irradiation. (from [63])

Bibliography

[1] A. Oed. "Position-sensitive detector with microstrip anode for electron multiplication with gases". In: *Nuclear Instruments and Methods in Physics Research Section A: Accelerators, Spectrometers, Detectors and Associated Equipment* 263.2 (1988), pp. 351–359. ISSN: 0168-9002. DOI: https://doi.org/10.1016/0168-9002(88)90970-9. URL: https://www.sciencedirect.com/science/article/pii/0168900288909709.

[2] Georges Charpak, R. Bouclier, T. Bressani, J. Favier, and C. Zupancic. "The Use of Multiwire Proportional Counters to Select and Localize Charged Particles". In: *Nucl. Instrum. Meth.* 62 (1968), pp. 262–268. DOI: 10.1016/0029-554X(68)90371-6.

[3] F. Sauli. "GEM: A new concept for electron amplification in gas detectors". In: *Nuclear Instruments and Methods in Physics Research Section A: Accelerators, Spectrometers, Detectors and Associated Equipment* 386.2 (1997), pp. 531–534. ISSN: 0168-9002. DOI: https://doi.org/10.1016/S0168-9002(96)01172-2. URL: https://www.sciencedirect.com/science/article/pii/S0168900296011722.

[4] "LHC Machine". In: *JINST* 3 (2008). Ed. by Lyndon Evans and Philip Bryant, S08001. DOI: 10.1088/1748-0221/3/08/S08001.

[5] Burkhard Schmidt. "The High-Luminosity upgrade of the LHC: Physics and Technology Challenges for the Accelerator and the Experiments". In: *Journal of Physics: Conference Series* 706.2 (2016), p. 022002. DOI: 10.1088/1742-6596/706/2/022002. URL: https://dx.doi.org/10.1088/1742-6596/706/2/022002.

[6] *The Phase-2 Upgrade of the CMS Muon Detectors*. Tech. rep. This is the final version, approved by the LHCC. Geneva: CERN, 2017. URL: https://cds.cern.ch/record/2283189.

[7] Dorothea Pfeiffer, Georgi Gorine, Hans Reithler, Bartolomej Biskup, Alasdair Day, Adrian Fabich, Joffrey Germa, Roberto Guida, Martin Jaekel, and Federico Ravotti. "The radiation field in the Gamma Irradiation Facility GIF++ at CERN". In: *Nuclear Instruments and Methods in Physics Research Section A: Accelerators, Spectrometers, Detectors and Associated Equipment* 866 (2017), pp. 91–103. ISSN: 0168-9002. DOI: https://doi.org/10.1016/j.nima.2017.05.045. URL: https://www.sciencedirect.com/science/article/pii/S0168900217306113.

[8] H. Kolanoski and N. Wermes. *Particle Detectors: Fundamentals and Applications*. Oxford University Press, 2020. ISBN: 9780198858362. URL: https://books.google.it/books?id=2TjpDwAAQBAJ.

[9] Fabio Sauli. *Gaseous Radiation Detectors: Fundamentals and Applications*. Cambridge Monographs on Particle Physics, Nuclear Physics and Cosmology. Cambridge University Press, 2014.

[10] Fabio Sauli. *Principles of operation of multiwire proportional and drift chambers*. Tech. rep. CERN, Geneva, 1975 - 1976. Geneva, 1977. DOI: 10.5170/CERN-1977-009. URL: https://cds.cern.ch/record/117989.

[11] Fabio Sauli. *Micro-pattern gaseous detectors: principles of operation and applications*. Singapore: World Scientific, 2021. URL: https://cds.cern.ch/record/2730577.

[12] John Douglas Cockcroft. "Experimental Nuclear Physics". In: *Nature* 175 (1955). URL: https://api.semanticscholar.org/CorpusID:4249052.

[13] N. Bohr. "II. On the theory of the decrease of velocity of moving electrified particles on passing through matter". In: *The London, Edinburgh, and Dublin Philosophical Magazine and Journal of Science* 25.145 (1913), pp. 10–31. DOI: 10.1080/14786440108634305. eprint: https://doi.org/10.1080/14786440108634305. URL: https://doi.org/10.1080/14786440108634305.

[14] R. L. Workman and Others. "Review of Particle Physics". In: *PTEP* 2022 (2022), p. 083C01. DOI: 10.1093/ptep/ptac097.

[15] J. Beringer et al. "Review of Particle Physics". In: *Phys. Rev. D* 86 (1 2012), p. 010001. DOI: 10.1103/PhysRevD.86.010001. URL: https://link.aps.org/doi/10.1103/PhysRevD.86.010001.

[16] L.B. Loeb. *Basic Processes of Gaseous Electronics*. University of California Press, 2022. ISBN: 9780520348929. URL: https://books.google.it/books?id=1SOFEAAAQBAJ.

[17] J.S.E. Townsend and J. Townsend. *Electrons in Gases*. Hutchinson's Scientific and Technical Publications, 1948. URL: https://books.google.it/books?id=NOafAAAAMAAJ.

[18] A. Chirokov, Alexander Gutsol, and A. Fridman. "Atmospheric pressure plasma of dielectric barrier discharges". In: *Pure and Applied Chemistry - PURE APPL CHEM* 77 (Jan. 2005), pp. 487–495. DOI: 10.1351/pac200577020487.

[19] W. Shockley. "Currents to Conductors Induced by a Moving Point Charge". In: *Journal of Applied Physics* 9.10 (Oct. 1938), pp. 635–636. ISSN: 0021-8979. DOI: 10.1063/1.1710367. eprint: https://pubs.aip.org/aip/jap/article-pdf/9/10/635/18304047/635_1_online.pdf. URL: https://doi.org/10.1063/1.1710367.

[20] S. Ramo. "Currents Induced by Electron Motion". In: *Proceedings of the IRE* 27.9 (1939), pp. 584–585. DOI: 10.1109/JRPROC.1939.228757.

[21] Rajendra Nath Patra, R. N. Singaraju, S. Biswas, T. K. Nayak, and Y. P. Viyogi. "Time Resolution and Characteristic Studies of MWPC Detectors with Argon Based Gas Mixtures". In: *Springer Proceedings in Physics*. Springer International Publishing, 2018, 509–512. ISBN: 9783319731711. DOI: 10.1007/978-3-319-73171-1_119. URL: http://dx.doi.org/10.1007/978-3-319-73171-1_119.

[22] *Garfield*. https://garfield.web.cern.ch/garfield/. 1984.

[23] D Acosta, G Apollinari, J Blomquist, R Breedon, N Bondar, Yu Bonushkin, E Borissov, A Bujak, B Bylsma, N Chester, D Chrisman, D Cline, S Dolinsky, S Durkin, D Eartly, T Ferguson, F Feyzi, J Gilmore, L Gorn, W Gorn, J Gu, L Gutay, J Hauser, S Hershman II, J Hoftiezer, O Kisselev, W Ko, J Korienek, A Korytov, J Kubic, J Layter, T.Y Ling, R Loveless, S Lusin, C Matthey, M Matveev, S Medved, G Mitselmakher, S Otwinowski, P Padley, F Petriello, Yu Pischalnikov, O Prokofiev, V Razmyslovich, D Reeder, J Roberts, P Robl, C

Rush, J.-C Santiard, S Sedov, B Smith, S Sobolev, V Soulimov, B Tannenbaum, N Terentyev, A Vorobyov, and V Yarba. "Large CMS cathode strip chambers: design and performance". In: *Nuclear Instruments and Methods in Physics Research Section A: Accelerators, Spectrometers, Detectors and Associated Equipment* 453.1 (2000). Proc. 7th Int. Conf on Instrumentation for colliding Beam Physics, pp. 182–187. ISSN: 0168-9002. DOI: https://doi.org/10.1016/S0168-9002(00)00627-6. URL: https://www.sciencedirect.com/science/article/pii/S0168900200006276.

[24] Daniel Francois Teyssier. *CMS Drift Tubes performance*. Tech. rep. Geneva: CERN, 2016. URL: https://cds.cern.ch/record/2118383.

[25] R. Santonico and R. Cardarelli. "Development of resistive plate counters". In: *Nuclear Instruments and Methods in Physics Research* 187.2 (1981), pp. 377–380. ISSN: 0167-5087. DOI: https://doi.org/10.1016/0029-554X(81)90363-3. URL: https://www.sciencedirect.com/science/article/pii/0029554X81903633.

[26] R. Cardarelli, R. Santonico, A. Di Biagio, and A. Lucci. "Progress in resistive plate counters". In: *Nuclear Instruments and Methods in Physics Research Section A: Accelerators, Spectrometers, Detectors and Associated Equipment* 263.1 (1988), pp. 20–25. ISSN: 0168-9002. DOI: https://doi.org/10.1016/0168-9002(88)91011-X. URL: https://www.sciencedirect.com/science/article/pii/016890028891011X.

[27] R. Cardarelli, A. Di Ciaccio, and R. Santonico. "Performance of a resistive plate chamber operating with pure CF-3 - Br". In: *Nucl. Instrum. Meth. A* 333 (1993), pp. 399–403. DOI: 10.1016/0168-9002(93)91182-M.

[28] I. Crotty, J. Lamas Valverde, G. Laurenti, M.C.S. Williams, and A. Zichichi. "Further studies of avalanche mode operation of resistive parallel plate chambers". In: *Nuclear Instruments and Methods in Physics Research Section A: Accelerators, Spectrometers, Detectors and Associated Equipment* 346.1 (1994), pp. 107–113. ISSN: 0168-9002. DOI: https://doi.org/10.1016/0168-9002(94)90693-9. URL: https://www.sciencedirect.com/science/article/pii/0168900294906939.

[29] M. Abbrescia, A. Colaleo, G. Iaselli, F. Loddo, M. Maggi, B. Marangelli, S. Natali, S. Nuzzo, G. Pugliese, A. Ranieri, F. Romano, G. Gianini, S.P. Ratti, and P. Vitulo. "Resistive Plate Chambers in avalanche mode: a comparison between model predictions and experimental results11Talk presented by M. Abbrescia at the 7th Meeting on advanced detectors, La Biodola, Isola d'Elba, Italy, 25–31 May 1997." In: *Nuclear Instruments and Methods in Physics Research Section A: Accelerators, Spectrometers, Detectors and Associated Equipment* 409.1 (1998), pp. 1–5. ISSN: 0168-9002. DOI: https://doi.org/10.1016/S0168-9002(97)01225-4. URL: https://www.sciencedirect.com/science/article/pii/S0168900297012254.

[30] A. Breskin, G. Charpak, F. Sauli, M. Atkinson, and G. Schultz. "Recent observations and measurements with high-accuracy drift chambers". In: *Nuclear Instruments and Methods* 124.1 (1975), pp. 189–214. ISSN: 0029-554X. DOI: https://doi.org/10.1016/0029-554X(75)90403-6. URL: https://www.sciencedirect.com/science/article/pii/0029554X75904036.

[31] A Oed. "Properties of micro-strip gas chambers (MSGC) and recent developments". In: *Nuclear Instruments and Methods in Physics Research Section A: Accelerators, Spectrometers, Detectors and Associated Equipment* 367.1 (1995). Proceedings of the 7th International Wire Chamber Conference, pp. 34–40. ISSN: 0168-9002. DOI: https://doi.org/10.1016/0168-9002(95)00657-5. URL: https://www.sciencedirect.com/science/article/pii/0168900295006575.

[32] Fabio Sauli and A. Sharma. "Micro-pattern gaseous detectors". In: *Annual Review of Nuclear and Particle Science* 49 (Dec. 1999). DOI: 10.1146/annurev.nucl.49.1.341.

[33] Suzan Bachmann, A. Bressan, Alfredo Placci, Leszek Ropelewski, and Fabio Sauli. "Optimization of operation and test of large size GEM detectors". In: (Jan. 1999).

[34] Alexey Buzulutskov. "Radiation detectors based on gas electron multipliers (Review)". In: *Instruments and Experimental Techniques* 50 (May 2007), pp. 287–310. DOI: 10.1134/S0020441207030013.

[35] A Bondar, A Buzulutskov, L Shekhtman, and A Vasiljev. "Study of ion feedback in multi-GEM structures". In: *Nuclear Instruments and Methods in Physics Research Section A: Accelerators, Spectrometers, Detectors and Associated Equipment* 496.2-3 (2003), pp. 325–332.

[36] Marie Blatnik, Klaus Dehmelt, Abhay Deshpande, Dhruv Dixit, Nils Feege, Thomas K. Hemmick, Benji Lewis, Martin L. Purschke, William Roh, Fernando Torales-Acosta, Thomas Videbaek, and Stephanie Zajac. "Performance of a Quintuple-GEM Based RICH Detector Prototype". In: *IEEE Transactions on Nuclear Science* 62.6 (Dec. 2015), 3256–3264. ISSN: 1558-1578. DOI: 10.1109/tns.2015.2487999. URL: http://dx.doi.org/10.1109/TNS.2015.2487999.

[37] F. Ivone. "Discharge mitigation strategies for the CMS GE1/1 Triple-GEM detectors". In: *Journal of Instrumentation* 15.05 (2020), p. C05009. DOI: 10.1088/1748-0221/15/05/C05009. URL: https://dx.doi.org/10.1088/1748-0221/15/05/C05009.

[38] S. Bachmann, A. Bressan, M. Capeáns, M. Deutel, S. Kappler, B. Ketzer, A. Polouektov, L. Ropelewski, F. Sauli, E. Schulte, L. Shekhtman, and A. Sokolov. "Discharge studies and prevention in the gas electron multiplier (GEM)". In: *Nuclear Instruments and Methods in Physics Research Section A: Accelerators, Spectrometers, Detectors and Associated Equipment* 479.2 (2002), pp. 294–308. ISSN: 0168-9002. DOI: https://doi.org/10.1016/S0168-9002(01)00931-7. URL: https://www.sciencedirect.com/science/article/pii/S0168900201009317.

[39] Patrik Thuiner. "Ion space-charge effects in multi-GEM detectors: challenges and possible solutions for future applications". Presented 07 Dec 2016. TU Vienna, 2016. URL: https://cds.cern.ch/record/2238855.

[40] M. Alfonsi, G. Croci, S. Duarte Pinto, E. Rocco, L. Ropelewski, F. Sauli, R. Veenhof, and M. Villa. "Simulation of the dielectric charging-up effect in a GEM detector". In: *Nucl. Instrum. Meth. A* 671 (2012), pp. 6–9. DOI: 10.1016/j.nima.2011.12.059.

[41] M Alfonsi, G Bencivenni, P de Simone, F Murtas, M Poli Lener, W Bonivento, A Cardini, C Deplano, D Pinci, D Raspino, and B Saitta. "A triple-GEM detector for high-rate particle triggering". In: *Nuclear Instruments and Methods in Physics Research Section A: Accelerators, Spectrometers, Detectors and Associated*

Equipment 525.1 (2004). Proceedings of the International Conference on Imaging Techniques in Subatomic Physics, Astrophysics, Medicine, Biology and Industry, pp. 17–19. ISSN: 0168-9002. DOI: https://doi.org/10.1016/j.nima.2004.03.026. URL: https://www.sciencedirect.com/science/article/pii/S0168900204003407.

[42] M. Alfonsi, S. Baccaro, G. Bencivenni, W. Bonivento, A. Cardini, P. de Simone, F. Murtas, D. Pinci, M.P. Lener, D. Raspino, and B. Saitta. "Studies of etching effects on triple-GEM detectors operated with CF/sub 4/-based gas mixtures". In: *IEEE Transactions on Nuclear Science* 52.6 (2005), pp. 2872–2878. DOI: 10.1109/TNS.2005.855640.

[43] F Fallavollita. "Aging phenomena and discharge probability studies of the triple-GEM detectors for future upgrades of the CMS muon high rate region at the HL-LHC". In: *Nucl. Instrum. Methods Phys. Res., A* 936 (2019), pp. 427–429. DOI: 10.1016/j.nima.2018.10.180. URL: https://cds.cern.ch/record/2692480.

[44] Tomonori Ikeda, Kentaro Miuch, Atsuhiko Ochi, Ryota Yakabe, Takashi Hashimoto, Ryosuke Taishaku, Daniel P. Snowden-Ifft, Jean-Luc Gauvreau, Toru Tanimori, Atsushi Takada, and Kiseki Nakamura. "Study of Negative-Ion TPC Using -PIC for Directional Dark Matter Search". In: *EPJ Web of Conferences* 174 (2018). Ed. by S. Dalla Torre, B. Gobbo, S. Levorato, L. Ropelewski, and F. Tessarotto, p. 02006. ISSN: 2100-014X. DOI: 10.1051/epjconf/201817402006. URL: http://dx.doi.org/10.1051/epjconf/201817402006.

[45] Francesca Carnesecchi. "Experimental study of the time resolution for particle detectors based on MRPC, SiPM and UFSD technologies". PhD thesis. alma, 2018. URL: http://amsdottorato.unibo.it/8538/.

[46] Z. Liu, F. Carnesecchi, M.C.S. Williams, A. Zichichi, and R. Zuyeuski. "Timing performance study of Multigap Resistive Plate Chamber with different gap size". In: *Nuclear Instruments and Methods in Physics Research Section A: Accelerators, Spectrometers, Detectors and Associated Equipment* 927 (2019), pp. 396–400. ISSN: 0168-9002. DOI: https://doi.org/10.1016/j.nima.2019.02.068. URL: https://www.sciencedirect.com/science/article/pii/S0168900219302566.

[47] M Poli-Lener. "Triple-GEM detectors for the innermost region of the muon apparatus at the LHCb experiment". Presented on 01 Dec 2005. Roma U., 2005. URL: https://cds.cern.ch/record/940631.

[48] M Alfonsi. "The GEM detectors for the innermost region of the forward muon station of the LHCb experiment". U. Rome 2, Tor Vergata (main), 2008. DOI: 2108/496. URL: https://cds.cern.ch/record/2093526.

[49] G L Bayatian et al. *CMS Physics: Technical Design Report Volume 1: Detector Performance and Software*. Technical design report. CMS. There is an error on cover due to a technical problem for some items. Geneva: CERN, 2006. URL: https://cds.cern.ch/record/922757.

[50] Tai Sakuma. "3D SketchUp images of the CMS detector (120918)". In: (2016).

[51] Waqar Ahmed. "The Compact Muon Solenoid Experiment Status of the electronics and DAQ for the Triple-GEM project for the upgrade of the CMS forward muon spectrometer". In: Dec. 2015.

[52] Sergio Cittolin, Attila Rácz, and Paris Sphicas. *CMS The TriDAS Project: Technical Design Report, Volume 2: Data Acquisition and High-Level Trigger. CMS trigger and data-acquisition project*. Technical design report. CMS. Geneva: CERN, 2002. URL: https://cds.cern.ch/record/578006.

[53] Gabriella Pásztor. "The Phase-2 Upgrade of the CMS Detector". In: *PoS* LHCP2022 (2023), p. 045. DOI: 10.22323/1.422.0045. URL: https://cds.cern.ch/record/2880161.

[54] Benjamin Charles Radburn-smith. *Overview of the HL-LHC Upgrade for the CMS Level-1 Trigger*. Tech. rep. Geneva: CERN, 2023. DOI: 10.22323/1.414.0639. URL: https://cds.cern.ch/record/2841568.

[55] *The Phase-2 Upgrade of the CMS Tracker*. Tech. rep. Geneva: CERN, 2017. DOI: 10.17181/CERN.QZ28.FLHW. URL: https://cds.cern.ch/record/2272264.

[56] *The Phase-2 Upgrade of the CMS Endcap Calorimeter*. Tech. rep. Geneva: CERN, 2017. DOI: 10.17181/CERN.IV8M.1JY2. URL: https://cds.cern.ch/record/2293646.

[57] Grégory Soyez. "Pileup mitigation at the LHC: A theorist's view". In: *Physics Reports* 803 (2019). Pileup mitigation at the LHC: A theorist's view, pp. 1–158. ISSN: 0370-1573. DOI: https://doi.org/10.1016/j.physrep.2019.01.007. URL: https://www.sciencedirect.com/science/article/pii/S0370157319300456.

[58] D. Abbaneo, Masooma Abbas, Marcello Abbrescia, Ahmed Abdelalim, Maya Abi Akl, Waqar Ahmed, Palma Altieri, Reham Aly, A Ashfaq, P. Aspell, Yasser Assran, I. Awan, S. Bally, Yunqi Ban, Sampriti Banerjee, Patrizia Barria, Luigi Benussi, Vallary Bhopatkar, and Siah Bianco. "Upgrade of the CMS muon system with triple-GEM detectors". In: *Journal of Instrumentation* 9 (Oct. 2014). DOI: 10.1088/1748-0221/9/10/C10036.

[59] *The Phase-2 Upgrade of the CMS L1 Trigger Interim Technical Design Report*. Tech. rep. This is the CMS Interim TDR devoted to the upgrade of the CMS L1 trigger in view of the HL-LHC running, as approved by the LHCC. Geneva: CERN, 2017. DOI: 10.17181/CERN.UUWZ.FMIS. URL: https://cds.cern.ch/record/2283192.

[60] D. Abbaneo et al. "Performance of a Large-Area GEM Detector Prototype for the Upgrade of the CMS Muon Endcap System. Performance of a Large-Area GEM Detector Prototype for the Upgrade of the CMS Muon Endcap System". In: (2016). 8 pages, 32 figures, submitted to Proc. 2014 IEEE Nucl. Sci. Symposium, Seattle, WA, reference added, p. 7431249. DOI: 10.1109/NSSMIC.2014.7431249. arXiv: 1412.0228. URL: https://cds.cern.ch/record/1973272.

[61] M. Bianco, F. Fallavollita, D. Fiorina, A. Pellecchia, L. F. Ramirez Garcia, N. Rosi, and P. Verwilligen. "Rate Capability of Large-Area Triple-GEM Detectors and New Foil Design for the Innermost Station, ME0, of the CMS Endcap Muon System". In: *2021 IEEE Nuclear Science Symposium and Medical Imaging Conference (NSS/MIC)*. 2021, pp. 1–5. DOI: 10.1109/NSS/MIC44867.2021.9875626.

[62] F. Fallavollita. "Novel triple-GEM mechanical design for the CMS-ME0 detector and its preliminary performance". In: *Journal of Instrumentation* 15.08 (2020), p. C08002. DOI: 10.1088/1748-0221/15/08/C08002. URL: https://dx.doi.org/10.1088/1748-0221/15/08/C08002.

[63] Antonello Pellecchia. "Performance of micro-pattern gaseous detectors at the LHC and future collider experiments". Presented 2023. Bari U., 2023. URL: https://cds.cern.ch/record/2860786.

[64] M. Bianco, F. Fallavollita, D. Fiorina, A. Pellecchia, L. F. Ramirez Garcia, N. Rosi, and P. Verwilligen. "Rate Capability of Large-Area Triple-GEM Detectors and New Foil Design for the Innermost Station, ME0, of the CMS Endcap Muon System". In: *2021 IEEE Nuclear Science Symposium and Medical Imaging Conference (NSS/MIC)*. 2021, pp. 1–5. DOI: 10.1109/NSS/MIC44867.2021.9875626.

[65] Piet Verwilligen and on behalf of the CMS Muon group. "GEM detectors for the CMS endcap muon system: status of three new detector stations". In: *Journal of Instrumentation* 18.07 (2023), p. C07006. DOI: 10.1088/1748-0221/18/07/C07006. URL: https://dx.doi.org/10.1088/1748-0221/18/07/C07006.

[66] M. Abbas et al. "Quality control of mass-produced GEM detectors for the CMS GE1/1 muon upgrade". In: *Nuclear Instruments and Methods in Physics Research Section A: Accelerators, Spectrometers, Detectors and Associated Equipment* 1034 (2022), p. 166716. ISSN: 0168-9002. DOI: https://doi.org/10.1016/j.nima.2022.166716. URL: https://www.sciencedirect.com/science/article/pii/S0168900222002480.

[67] D. Fiorina. "ME0 project for the Triple-GEM upgrade of the CMS muon spectrometer: Design, preliminary performance and R&D perspective". In: *Nuovo Cim. C* 44.2-3 (2021), p. 45. DOI: 10.1393/ncc/i2021-21045-2.

[68] P. Aspell, C. Bravo, M. Dabrowski, G. De Lentdecker, G. De Robertis, M. Firlej, T. Fiutowski, T. Hakkarainen, M. Idzik, A. Irshad, P. Leroux, F. Licciulli, F. Loddo, A. Muhammad, J. Moron, H. Petrow, K. Swientek, F. Tavernier, and T. Tuuva. "VFAT3: A Trigger and Tracking Front-end ASIC for the Binary Readout of Gaseous and Silicon Sensors". In: *2018 IEEE Nuclear Science Symposium and Medical Imaging Conference Proceedings (NSS/MIC)*. 2018, pp. 1–8. DOI: 10.1109/NSSMIC.2018.8824655.

[69] Thierry Maerschalk. "Study of Triple-GEM detector for the upgrade of the CMS muon spectrometer at LHC". Brussels U., 2016. URL: https://cds.cern.ch/record/2291028.

[70] *Edimburgh Instruments*. Accessed on 06 27, 2024. URL: https://www.edinst.com/blog/constant-fraction-discrimination/.

[71] Julian Maxime Mendez, Sophie Baron, Szymon Kulis, and Jose Fonseca. "New LpGBT-FPGA IP: Simulation model and first implementation". In: *PoS* TWEPP2018 (2019), p. 059. DOI: 10.22323/1.343.0059.

[72] *PICMG*. Accessed on 06 27, 2024. URL: https://www.picmg.org/openstandards/advancedtca/.

[73] *CAEN*. Accessed on 06 27, 2024. URL: https://www.caen.it/products/a1515b/.

[74] *CAEN*. Accessed on 06 27, 2024. URL: https://www.caen.it/products/easy3000/.

[75] Giovanni Mocellin. "Performance of the GE1/1 detectors for the upgrade of the CMS muon forward system". Presented 19 Jul 2021. RWTH Aachen University, 2021. URL: https://cds.cern.ch/record/2809098.

[76] *MAXIMUS.ENERGY*. Accessed on 06 29, 2024. URL: https://maximus.energy/index.php/2020/10/24/the-rich-physics-of-cs-137-gamma-spectrum/.

[77] Alexis Fagot, Anna Cimmino, Shannon Crucy, Mazlum Gul, Alberto Rios, Michael Tytgat, Nikolaos Zaganidis, Soher Aly, Yasser Assran, Amr Radi, A. Sayed, Gurdishpal Singh, Marcello Abbrescia, G. Iaselli, M. Maggi, Gabriella Pugliese, Piet Verwilligen, W. Doninck, and Juozas Vaitkus. "RD towards the CMS RPC Phase-2 upgrade". In: *Journal of Instrumentation* 11 (June 2016). DOI: 10.1088/1748-0221/11/09/C09017.

[78] *Radioactivity Environmental Monitoring*. Accessed on 06 30, 2024. URL: https://remap.jrc.ec.europa.eu/Advanced.aspx.

[79] Glenn F Knoll. *Radiation detection and measurement; 4th ed.* New York, NY: Wiley, 2010. URL: https://cds.cern.ch/record/1300754.

[80] *Timber CERN webpage*. URL: https://timber.cern.ch/.

[81] G. Mocellin. *CERN Indico page GEM sessions*. URL: https://indico.cern.ch/event/1372009/#59-vfat-timing-update.

[82] Eungchun Cho and Moon J. Cho. *Variance of the With-Replacement Sample Variance*. URL: http://www.asasrms.org/Proceedings/y2008/Files/300992.pdf.

[83] *EMU 0xBEFE Project*. Accessed: 2024-07-10. 2024. URL: https://gitlab.cern.ch/emu/0xbefe/-/blob/devel/common/hdl/lpgbt/lpgbt.vhd#L197.